The Pennsylvania State University
The Graduate School
College of Engineering

SIMULATIONS OF THE FLOW GENERATED BY FLUIDIC INSERTS IN A CONVERGING DIVERGING NOZZLE

A Thesis in
Aerospace Engineering
by
Jacob Lampenfield

Submitted in Partial Fulfillment
of the Requirements
for the Degree of

Master of Science

May 2016

The thesis of Jacob Lampenfield was reviewed and approved* by the following:

Philip J. Morris
Boeing/A.D. Welliver Professor of Aerospace Engineering
Thesis Advisor

Dennis K. McLaughlin
Professor of Aerospace Engineering

George A. Lesieutre
Professor of Aerospace Engineering
Head of The Department of Aerospace Engineering

*Signatures are on file in the Graduate School.

Abstract

This investigation of military jet noise prediction and reduction is a continuation from previous projects and is still ongoing. Numerical simulations have been performed on baseline nozzles and nozzles with the addition of fluidic inserts. The design Mach number of the nozzle is 1.65, but only the over-expanded Mach number of 1.36 has been analyzed. The fluidic inserts have been generated using different numbers of injectors and injector hole sizes.

The supersonic military style jet simulation makes use of advanced meshes combined with CFD technology. Steady Reynolds-averaged Navier-Stokes (RANS) simulations are produced by the CFD technology and used to predict and understand the flow field. Through collaboration with experimental noise measurements, a correlation between flow field properties and noise reduction is examined. The ANSYS suite is used to create grids and run simulations by using ANSYS-ICEM and ANSYS-CFX respectively. The geometry of the nozzle is modeled using an unstructured hexahedral mesh. The Menter SST turbulence model with a wall function is used inside of the CFX-Solver.

The objective is to further simulate a military-style nozzle, similar to the GE F404 family, with added fluidic inserts. Previous simulations have been conducted and new simulations were planned and performed based on information gathered from the previous simulations and experiments. The fluidic inserts are used to alter the flow field to achieve the same effect of hard wall corrugations, which have been shown to reduce noise levels. The numerical simulations are used to help understand the effects on the flow field created by the fluidic inserts and to attempt to find flow parameters that can be correlated to noise reduction.

Simulations were first run on a simpler geometry to give an understanding of the fluidic inserts. They were conducted by having three injectors exhausting into a supersonic boundary layer. The freestream Mach number was 1.5 to simulate the inside of the nozzle. A study was then conducted to see the effect of a change in downstream injector angle on the fluidic insert.

There was also a study of an increase Reynolds number as three different sized

nozzles were modeled. The first size is a small nozzle with an exit diameter of 0.885 inches. The nozzle size was then increased by a factor of 1.2 to an exit diameter of 1.06 inches. A third nozzle was then modeled to recreate the nozzle used in the GE experiments. This nozzle had a diameter of 5.07 inches.

The results from all the simulations were then compared to experimental acoustic data. Flow parameters were then integrated from each simulation to attempt to find a correlation to noise reduction. Parameters such as streamwise vorticity, turbulent kinetic energy, and Q criterion were all analyzed.

Table of Contents

List of Figures

List of Tables

List of Symbols

Abbrevations

BBSAN	Broadband shock associated noise
CDN	Convergent-divergent nozzle
CFD	Computational fluid dynamics
DES	Detached eddy simulation
DNS	Direct numerical simulation
FAA	Federal Aviation Administration
Inj	Injector
IPR	Injector pressure Ratio
LES	Large eddy simulation
NPR	Nozzle pressure ratio
RANS	Steady Reynolds-average Navier-Stokes
SPL	Sound pressure level
TKE	Turbulent kinetic energy
TTR	Total temperature ratio

Symbols

a	Local speed of sound

c_p	specific heat at constant pressure
D	Diameter of nozzle Exit
D^*	Diameter of nozzle throat
e	Total energy per unit mass
f	Frequency
L	Length
M_d	Design Mach number
M_j	Fully expanded jet Mach number
p	Pressure
Re	Reynolds number
T	Temperature
u, v, w	Cartesian velocity components
U_j	Fully expanded jet velocity
x, y, z	Cartesian coordinates
Greek Letters	
δ	Kronecker Delta
γ	Heat capacity ratio
μ	Dynamic viscosity
ν	Kinetic viscosity
ρ	Density
τ	Viscous stress
Superscripts	
*	Dimensionless value
'	Flucuating component around a time averaged value

Subscripts

0	Total condition
j	Fully expanded jet
∞	Reference values
i, j, k	Tensor notation indicies

Acknowledgments

I would first like to express my gratitude toward Dr. Phillip Morris for his help and insight into the numerical simulations and my thesis as a whole. He has been a constant help throughout my graduate school experience and has been a terrific mentor. I would also like to thank Dr. Dennis McLaughlin for introducing me to Dr. Morris and for his continued guidance and words of encouragement.

I would also like to thank my family and friends. First, my longtime girlfriend for constantly supporting me in every way possible while asking for nothing in return. I would also not have made it this far in my academic career without the encouragement from my parents. They have given me constant support and reassurance that I have to ability and means to do whatever I can think of.

Lastly, I would like to thank all my student colleagues who have helped me along the way. Matt Kapusta has given me all the knowledge and tools I needed and his insights into CFD have been invaluable. I would also like to thank Russell Powers and Scott Hromisin for taking the time to answer any questions I had and their insights into aeroacoustics. To anyone who was not listed here, I thank you for your support throughout my time here at Penn State. I would not have been able to do it without you.

Chapter 1 Introduction

1.1 Background

High noise levels have been a consequence of the invention of the jet engine. The noise that is generated from aircraft with these engines can disrupt the lives of people who live near areas of high air traffic. Loss of sleep, annoyance, and even effects on cardiovascular health are a few of the consequences of aircraft noise.

The Federal Aviation Administration (FAA) has made efforts to limit noise created by commercial aircraft in an attempt to reduce the health and environmental risks associated with exposure. According to the FAA, during the years 1975 to 2000 there has been a 90 percent reduction in the number of people exposed to significant noise levels. Most of the gains from quieter aircraft were achieved by 2000. The remaining problem can only be solved by changing operational procedures unless further noise reduction technologies are discovered. These reductions can be attributed to the strict regulations for noise levels made by the administration. [4]

Jet noise is not a problem that only pertains to civilian life. Military personnel face the same risks as civilians and also have added risks. Current tactical aircraft produce greater noise levels than commercial aircraft because they are not under the same strict regulations. The personnel working near the aircraft are exposed to these higher noise levels and are at high risk for health problems, even with the use of protective gear. Military personnel are working much closer to aircrafts than civilians and often times can not distance themselves from the aircrafts, like on an aircraft carrier.

However, many noise reduction techniques are being researched and applied to address the health and environmental concerns. One technique is the use of hard-wall corrugations in the divergent section of a GE military-style convergent-divergent nozzle. The idea was developed by Seiner and his colleagues at NASA Langley Research Center and the University of Mississippi. [5] The use of fluidic inserts is based on the original work by Seiner. However, the hard walled corrugations are replaced by strategic blowing in the diverging setion of the converging diverging nozzle. The original baseline nozzle is designed to operate at a Mach number of $M_d = 1.65$ and is based on of the GE F404 nozzle family. The divergent section of the nozzle is made up of flaps and seals that are represented by twelve facets.

Fludic inserts have been shown to be an effective technique for reducing generated noise. However, experiments are not able to see every detail due to limitations in the measurement equipment. Computational Fluid Dynamics (CFD) is a powerful tool that can be used to fill the gaps of experimental data. CFD can be used to guide and assist experimental noise research. Through the collaboration of both CFD and experimental research, a higher understanding of complex flow fields is possible.

1.2 Supersonic Jet Noise

This section encompasses the characteristics of supersonic jets and the associated generated noise. The concept of a convergent-divergent nozzle is presented along with the flowfield of a supersonic nozzle with and without fluidic insert, and the three components of noise generation.

1.2.1 Convergent-divergent Nozzle of Supersonic Jets

A turbofan jet engine is comprised of a fan, compressors, combustion chamber, and nozzle. The nozzle expels hot gases created in the combustion chamber into the atmosphere, which creates thrust. A high exit jet velocity is needed to maximize the amount of thrust. A convergent-divergent nozzle (CDN) has to be used to achieve high, supersonic speeds needed to generate large amounts of thrust. Noise is created by the CDN and the generated flow-field, but the parameters and conditions of the nozzle need to be understood to understand the different noise components.

The nozzle pressure ratio (NPR) is defined as the ratio of the jet plenum to the ambient pressure.

$$NPR = p_0/p_\infty \tag{1.1}$$

The minimum cross sectional area in the CDN is called the throat with a diameter denoted by D^*. The flow in the nozzle is related to the NPR and D^*.

The total temperature ratio (TTR) is similar to the NPR in that it is the ratio of the total temperature in the plenum to the ambient temperature.

$$TTR = p_0/p_\infty \tag{1.2}$$

Isentropic flow relations can be used to determine these conditions and the operation conditions of the nozzle. The Reynolds number (Re) is also an important parameter. Re is defined as the ratio of dynamic forces to viscous forces.

$$Re = \frac{U_j D}{\nu_j} \tag{1.3}$$

Where U_j is the fully expanded jet velocity, D is the jet exit diameter, and ν_j is the fully expanded jet flow kinematic viscosity. The design Mach number, M_d, is the fully expanded jet Mach number. This occurs when the nozzle exit static pressure is equal to the ambient pressure. When the nozzle is operating at the design Mach number, there are a minimum number of expansions and shock waves in the jet plume.

The geometry of the nozzle is linked to the design Mach number, specifically the areas in the nozzle. The ratio of the nozzle exit area to the area at the throat is given by (1.4).

$$\frac{A}{A^*} = \frac{(1 + \frac{\gamma - 1}{2})^{\frac{\gamma+1}{2(1-\gamma)}}}{M_d(1 + \frac{\gamma-1}{2} M_d^2)^{\frac{\gamma+1}{2(1-\gamma)}})} \tag{1.4}$$

γ is the specific heat ratio for an ideal gas, which is 1.4 for air. It is not possible for the design Mach number to be obtained explicitly in terms of the area ratio. In order to solve for M_d an iterative method has to be used, such as the Newton-Rasphon method. The flow is considered choked when the Mach number at the throat is equal to one.

If the design Mach number does not equal the fully expanded jet Mach number, the jet is said to be operating at off-design conditions. The fully expanded jet Mach number is directly related to the NPR . The NPR is the parameter that has the most effect on the flow outside of the nozzle. The jet can be operating subsonically or supersonically depending on the given NPR. The different operating conditions can be seen in Figure 1.1.

$$M_j = \left[\frac{2}{\gamma - 1}(NPR^{\frac{\gamma-1}{\gamma}} - 1)\right]^{1/2} \tag{1.5}$$

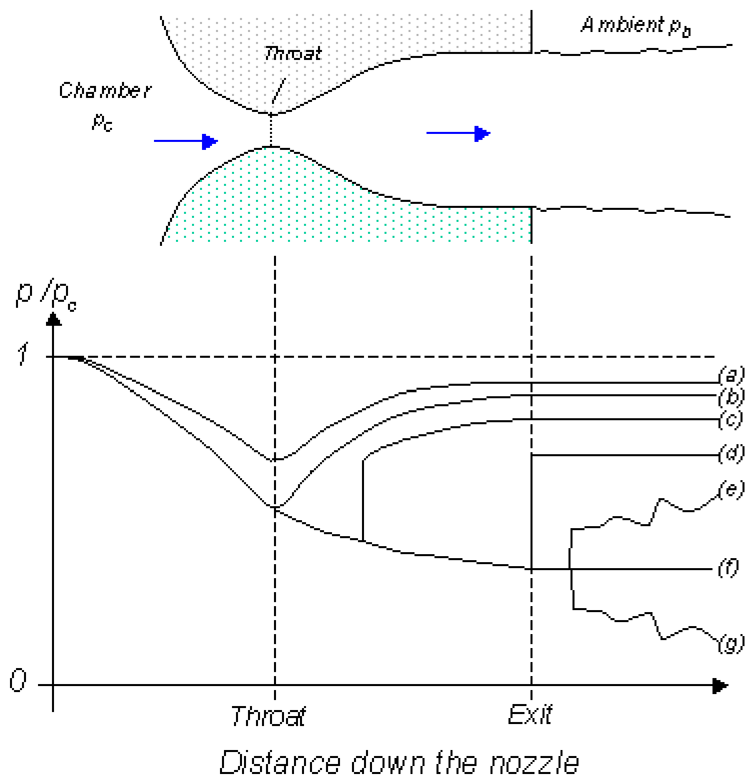

Figure 1.1. Schematic and relative operating conditions of a convergent-divergent nozzle based on NPR [1]

If the NPR is greater than NPR_b, the flow in the divergent section of the nozzle will be supersonic. However, if the NPR is less than NPR_d, the flow will be subsonic outside of the nozzle exit. This is caused by a strong normal shock that occurs inside the nozzle. The scope of this thesis only involves supersonic flow, thus only an NPR greater than NPR_d will be investigated, which leaves curves e, f, and g in Figure 1.1.

Curve e pertains to an over-expanded jet condition. The NPR for this conditions refers to $\mathrm{NPR_d} < \mathrm{NPR} < \mathrm{NPR_f}$. The static pressure at the exit is less than the ambient pressure. To correct for the deficit in pressure, oblique/bow shock waves are formed.

In order for the static pressure at the exit to be equal to the ambient pressure, the NPR has to be equal to $\mathrm{NPR_f}$. When this is the case, shock waves and expansion fans are not needed as the pressures are already equal. However, it is extremely rare for this condition to occur because of the complex nozzle geometries and operating conditions of the nozzle. If this condition is met, it is considered to be perfectly expanded or "on design".

Finally, if the NPR is greater than $\mathrm{NPR_f}$, the pressure at the nozzle exit is greater than the ambient pressure. To correct for the pressure difference, expansion fans are generated to reduce the nozzle exit pressure. When a jet is operating at this condition it is considered under-expanded.

1.2.2 Structure of the Supersonic Jet Flow-field

The previous section gave a summary of the basic fluid mechanics and boundary conditions of various jet conditions. The different jet conditions correspond to respective NPRs. This section explores the structure of the flow field generated by the nozzle.

Every numerical simulation and experiment presented in this thesis is for an over-expanded jet condition. The flow field of this case will be analyzed for the baseline and fluidic insert case, with varying numbers of injectors, at different nozzle sizes.

1.2.2.1 Flow Field of Axisymmetric Nozzle

The baseline nozzle is an axisymmetric nozzle, which has a design Mach number of 1.65. A detailed description of the numerical simulations is given in Chapter 2. Figure 1.2 presents a numerical schlieren for the baseline nozzle operating at an over-expanded jet condition. The NPR is 3.0 and the M_j is 1.36. The image is taken through the centerline of the nozzle.

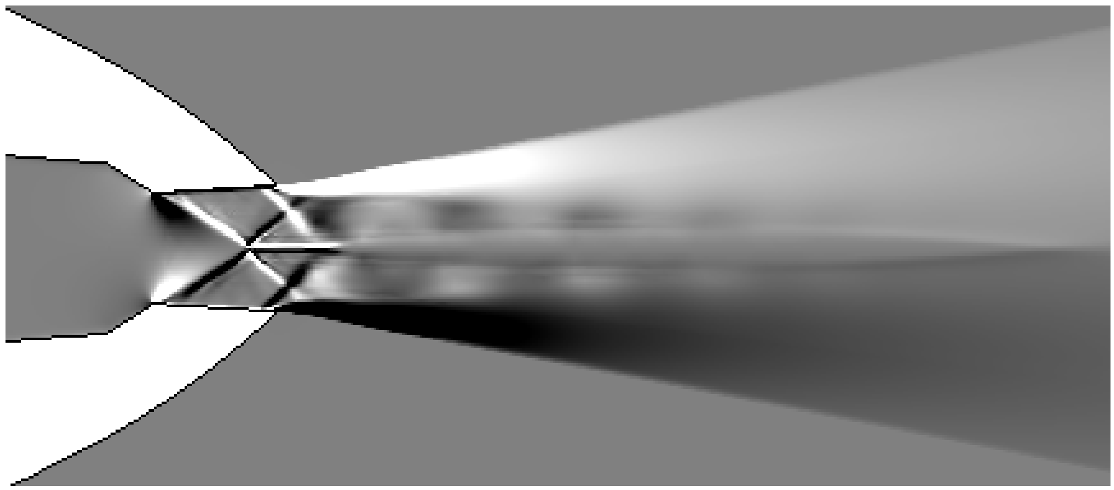

Figure 1.2. Numerical Schlieren of Military Style Nozzle

The Mach number in the converging section of the nozzle is always less than one. When the flow meets the throat the Mach number is equal to one. The Mach number then continues to increase until the flow reaches the exit, where it then equals the operating M_j. Inside the nozzle there are shocks and expansions, these waves will always be present as there is a sharp edge at the throat, even when the nozzle is operating on design. The waves appear because the geometry of the nozzle does not match the characteristic Mach waves, thus the reflection does not cancel.

Two oblique shock waves are created at the throat. The two waves merge and form a small Mach disk or barrel shock. The coalescence of the waves generates a subsonic region behind the Mach disk. Surrounding this region is a slip line and it occurs near the centerline of the nozzle. This flow pattern has been observed in previous numerical simulations. For instance it has appeared in the Large Eddy Simulations (LES) performed by Munday [6] which had a similar nozzle geometry.

Oblique shock waves are formed at the nozzle exit because the nozzle is being operated at an over-expanded jet condition. The exit pressure is lower than the ambient pressure so a shock has to be formed at the nozzle lip. This is always the case when the jet is over-expanded. A second Mach disk is formed where the oblique shocks meet. After the Mach disk subsides, the remaining jet plume contains oblique shocks and expansions. In this region the fluid is continuing to accelerate. This is because there is a pressure gradient that is less than one. There is a diamond shaped pattern in this region as well, which is known as the shock cell structure. This is due to the Mach waves interacting with the shear layer of the jet plume. The cross-sectional shape of the plume is circular for the entire length of the plume.

There is a turbulent shear layer which occurs in all jet plumes, whether it is a subsonic or supersonic jet. This shear layer is formed because of the high speed jet core interacting with the much slower or stationary freestream. The interaction creates instabilities, which are known as Kelvin-Helmholtz instabilities [7], whose growth generates the turbulent shear layer. Additional toroidal and helical vortices are created due to the nozzle not being perfectly circular. The divergent section of the nozzle is made up of flaps and seals that are used to control the area of the nozzle to better perform at different operating conditions. These instabilities and vortices are what causes the flow to become turbulent. This turbulent region surrounds the shock cell structure. The turbulent dissipation from this region weakens the shock cells. These interactions between the turbulent shear layer and the shock cell structure is the source of broadband shock associated noise(BBSAN).

1.2.2.2 Flow Field of Nozzle with Fluidic Inserts

All the design considerations that went into the baseline nozzle are also applied to a nozzle with fluidic inserts. The only geometric change is the addition of the fluidic injectors. The flow field structure is changed drastically due to the injected fluid. These changes can be seen in Figure 1.3.

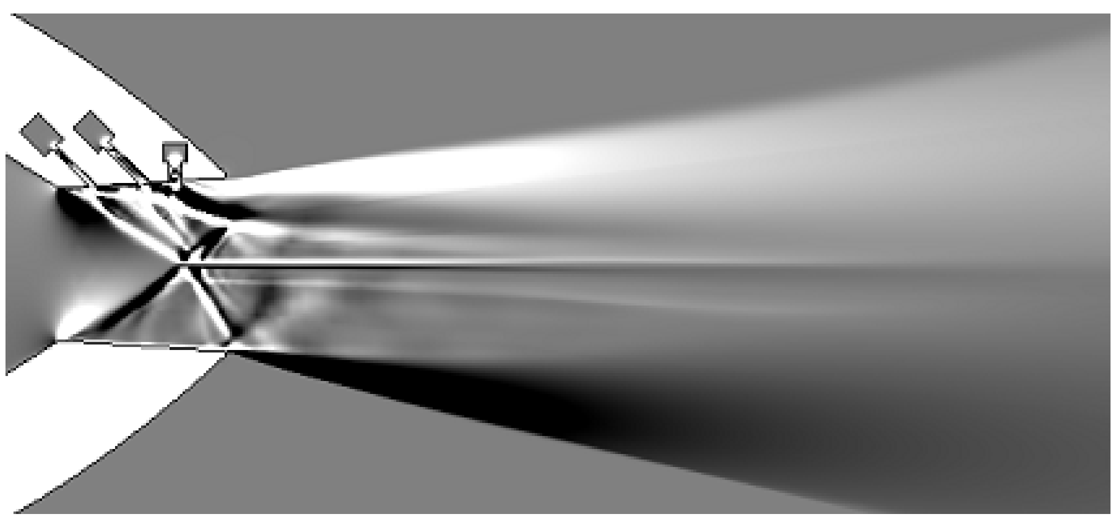

Figure 1.3. Numerical Schlieren of Military Style Nozzle with Fluidic Inserts

The injected fluid creates a bow shock in front of each injector. The first bow shock merges with the oblique shock from the throat practically immediately. The bow shocks ahead of the other injectors are easier to locate as there is no other shock for them to merge with. The two downstream bow shocks are in close proximity to one another. There is also an expansion that accompanies each injector, which appears downstream of the injector. The flow loses velocity due to the injected fluid but it still remains at supersonic speeds. The Mach disk that was seen in the baseline nozzle is reduced in size and severely disrupted.

The cross-sectional shape of the plume also changes with the addition of fluidic inserts. The cross section now has a triangular shape as apposed to the previous circular shape. This change in shape can be seen in Figure 1.4. The jet plume also becomes shorter with the addition of the injectors. Experiments by Powers [8] demonstrate this occurrence.

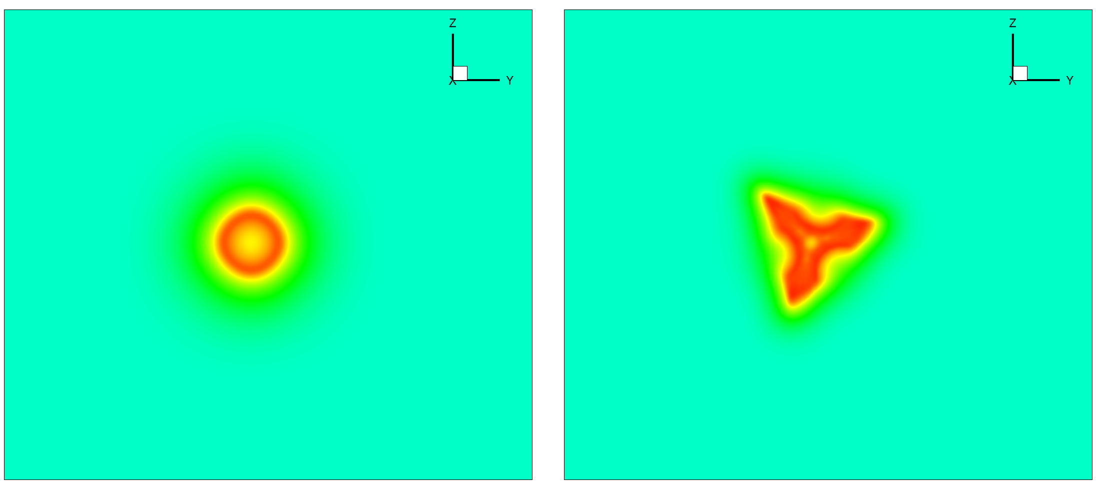

(a) (b)

Figure 1.4. Total pressure cross stream shape comparison at $2D_{Nozzle}$ downstream: (a) baseline (b) nozzle with fluidic inserts

1.2.3 Three Components of Noise Generation

The most common noise source is from the interactions between the turbulent eddies in the shear layer. This is referred to as turbulent mixing noise. This is occurs in both for supersonic and subsonic jets. Two further noise components occur when a supersonic jet is operating off design known as screech tones and turbulent mixing noise. The generated noise from the jet can be shown as a spectrum as a function of a non-dimensional parameter called the Strouhal number,St. The Strouhal number is defined by equation 1.7, where f_c is the characteristic frequency. The characteristic frequency is determined by the operating conditions of the nozzle.

$$f_c = \frac{u_j}{D_j} \tag{1.6}$$

$$St = f/f_c \tag{1.7}$$

The experimental data of the pressure time history of an acoustic signal is converted into a spectral density to obtain the SPL. An example of a jet noise spectrum can bee seen in Figure 1.5. This is taken from an experiment by Seiner. [9]

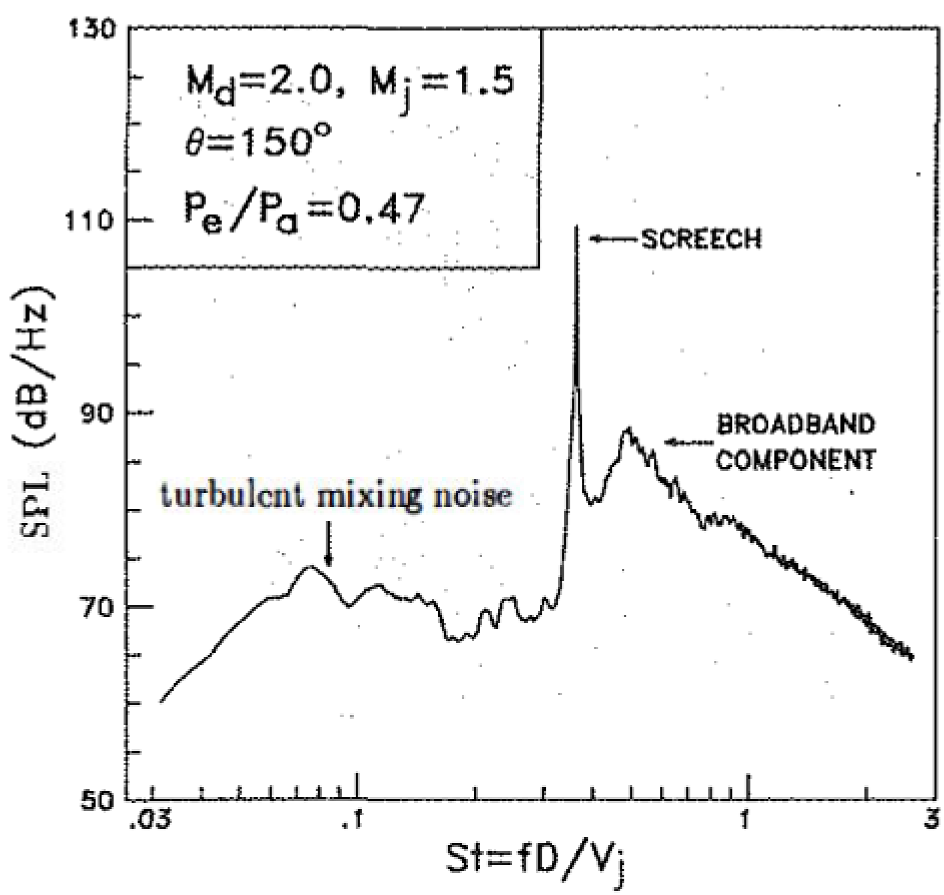

Figure 1.5. Supersonic Noise Components

If the jet is not operating on design, shock waves will form in the jet plume. This then results in broadband shock associated noise being created. This occurs as broad peaks in the acoustic spectrum. The noise radiated from the shocks largely depends on the geometry of the nozzle and the operating conditions. It also is very directional. Screech tones are a second component of noise created by a supersonic nozzle. They appear as a high amplitude, sharp peak in the noise spectra and are at an individual frequency. The three components, broadband shock associated noise, screech tones, and turbulent mixing noise, will be discussed in the following section.

1.2.3.1 Broadband Shock Associated Noise

As stated in a previous section, broadband shock associated noise (BBSAN) is created by the interaction of shock waves or expansion fans with the shear layer of the jet exhaust. BBSAN is nearly omnidirectional in nature. However, it is primarily observed upstream and is the largest noise contributor in that direction. It was not always confirmed that BBSAN was present in the far-field. The first acoustic experiment to determine if BBSAN was present in the far-field was conducted by Harper-Bourne and Fisher, who made use of a unheated, round convergent divergent nozzle. [10] Viswanathan showed that the turbulent mixing noise can have the same level as BBSAN at high frequencies, thus BBSAN needs to be carefully extracted when conducting experiments. [11] Whenever there is a change in the TTR there is a small increase in BBSAN. However, there is a point where the BBSAN stops increasing as the TTR increases. This is thought to be caused by the stabilization of the large scale structures in the shear layer, which causes the constant BBSAN. These differences in BBSAN when the jet is unheated or heated have been documented by Bridges. [12]

1.2.3.2 Screech Tones

A screech tone is a harsh tonal noise that occurs at well defined frequencies. Tam et al. [13] argue that screech tones are generated because of a feedback loop. The instabilities associated with the BBSAN travel upstream towards the nozzle. The traveling waves then interact with the thin shear layer at the nozzle lip. This interaction creates additional instability waves. The new waves are at first small in amplitude. However, they become excited near the nozzle lip. They become excited because the thin shear layer where they are forming is susceptible to external excitation. They then travel downstream, grow quickly, and interact with the jet's shock cell structure. This interaction generates BBSAN, which results in the upstream traveling acoustic waves, thus completing the feedback loop.

Structural damage to the nozzle can occur because of the high intensity noise. However, screech tones typically only appear in model size jets and generally do not appear in full size nozzles. The main factors in the creation of screech tones are the geometries of the lip and of the nozzle, the jet Mach number, and the temperature of the jet stream.

1.2.3.3 Turbulent Mixing Noise

Turbulent mixing noise is comprised of two components. These are related to the large scale and fine scale structures. [14] In terms of the noise spectra, the large scale structures correspond to a narrower spectrum shape, whereas the fine structures generate a flatter spectrum. The fine structures are more uniform than the large scale spectrum. The fine scale turbulence noise is mainly observable in the sideline and upstream directions. These characteristics can occur in both subsonic or supersonic jet conditions.

The large scale turbulence generates noise in the downstream direction of the jet and is the dominant source of noise. Mach wave radiation is generated by the supersonic convection of the large scale turbulent structures, relative to the ambient speed of sound. The noise caused by the Mach wave radiation is intenser than the noise generated in the upstream direction by the fine scale structures. [15]

1.3 Thesis Overview

The inspiration of this project was discussed in this chapter. A background of the characteristics of a supersonic nozzle, the flow field generated by the nozzle, and the three components of noise generation was presented. Chapter 2 will include information on the numerical methods used to generate the simulations. The governing equations that were used, the numerical solver, turbulence model, grid generation, and simulations strategy will be discussed. Chapter 3 will give a description on the generated numerical simulations for a simple geometry and a more complex geometry. The simple geometry is a supersonic boundary layer with three injectors exhausting into the freestream. This geometry will be used to give a description of the flow field generated by the fluidic inserts. A study will also be discussed on the effect of a change in downstream injector angle. The more complex geometry is a high speed military style nozzle with fluidic inserts. A comparison between a two injector and three injector per fluidic insert will be discussed. The results of a study on an increase in Reynolds number will also be discussed. The findings of an attempt to correlate noise reduction to flow parameters is also given. Chapter 4 provides a summary of all important results and gives suggestions for future work.

Chapter 2
Numerical Methods

This chapter provides a background of the flow solver and grid generation software that was used. ANSYS-CFX was used to produce all numerical results. ANSYS-ICEM was used as the grid generation software. The turbulence model and numerical method used in the flow solver will be described as well as the simulation strategy.

2.1 Governing Equations

To model the military style nozzle, the Reynolds-Averaged Navier-Stokes(RANS) equations were used. The conditions that were modeled are unsteady in nature and turbulent. However, the fine details of the turbulence was not needed. Only a basic understanding of how the average flow was affected by the fluidic inserts was investigated.

The RANS equations can be written in the terms of a fluctuating and mean component (2.1), where the overbar denotes the mean component and the lowercase denotes the fluctuating component.

$$U_i = \bar{U_i} + u_i \tag{2.1}$$

In the cases that are compressible flows, the averaging is weighted by density. This is known as Favre averaging. When the mean and fluctuating components are substituted into the original transport equations and the equations are averaged, the RANS equations are formed.

The following equations are the resulting RANS continuity, momentum, and energy equations (2.2), (2.3), and (2.4). The overbar is dropped for averaged quantities except for the products of fluctuating quantities.

$$\frac{\partial \rho}{\partial t} + \frac{\partial}{\partial x_j}(\rho U_j) = 0 \tag{2.2}$$

$$\frac{\partial \rho U_i}{\partial t} + \frac{\partial}{\partial x_j}(\rho U_i U_j) = -\frac{\partial p}{\partial x_i} + \frac{\partial}{\partial x_i}(\tau_{ij} - \rho \overline{u_i u_j}) + S_M \tag{2.3}$$

$$\frac{\partial h_{tot}}{\partial t} - \frac{\partial \rho}{\partial t} + \frac{\partial}{\partial x_j}(\rho U_j h_{tot}) = \frac{\partial}{\partial x_j}(\lambda \frac{\partial T}{\partial x_i} - \rho \overline{u_j h}) + \frac{\partial}{\partial x_j}[U_i(\tau_{ij} - \rho \overline{u_i u_j})] \tag{2.4}$$

Where the shear stress tensor is given by:

$$\tau_{ij} = \mu_t(\frac{\partial u_i}{\partial x_j} + \frac{\partial u_j}{\partial x_i} - \frac{2}{3}\frac{\partial u_k}{\partial x_j}\delta_{ij}) - \frac{2}{3}\rho k \delta_{ij} \tag{2.5}$$

The continuity equation (2.2) remains the same after it is broken up into the mean and fluctuating components. The momentum and energy equations have a new term added, $\rho \overline{u_i u_j}$, which is the Reynolds stress tensor. The Reynolds stress tensor contains the turbulent fluxes, which occurs due to the presences of the non-linear convection term of the unaltered governing equations.

2.2 Numerical Solver

ANSYS-CFX version 15 was used as the flow solver in all numerical simulations. ANSYS-CFX makes use of finite volume method to predict the flow. Each simulation performed was three dimensional. There are three software tools inside of CFX 15, which include CFX-PRE, CFX-SOLVER, and CFX-POST.

CFX-Pre is used to set up the problem. When using CFX-Pre, each part of the domain is defined as various boundaries, such as inlets and walls. The conditions of the simulation are also set, such as the NPR and TTR. The exit conditions are also set, where the minimum residual value or the maximum number of iterations has to be met. CFX-Solver is used to run the simulation in either series or parallel. When using the parallel version the computational speed is increased. CFX-Solver makes use of the conservative form of the Navier-Stokes equation to produce a solution.

CFX-Post can be used as a post processing tool of the simulation results. However, multiple post processing tools can be used such as Tecplot or Paraview. [16] Tecplot has been used for all post processing.

2.3 Turbulence Model

The Navier-Stokes equations can be used for both laminar and turbulent flows. If the equations remain unaltered when simulating flow, it is called Direct Numerical Simulation (DNS). DNS has been used for simple geometry flows with low Reynolds numbers, but it is very computationally expensive for higher Reynolds number. In high Reynolds number flows turbulence develops due to instabilities in the flow. Turbulence is three dimensional, unsteady, and has a continuous range of length and time scales by nature. These characteristics make turbulence complex. In order to properly simulate turbulence using DNS, the mesh would need to have an extremely high number of nodes with very fine grid spacing, which modern computing computers can not handle and many believe will never be able to handle. [16] To make reasonable predictions for the turbulenced, Large Eddy Simulations (LES) and Detached Eddy Simulations (DES) have been used. However, for RANS calculations a turbulence model is needed to provide the characteristics of the turbulent flow. Oftentimes a transitional turbulence model is needed as well, but this is not the case for the scope of this thesis as the Reynolds number is sufficiently high for fully turbulent flow to occur.

2.3.1 Menter SST Model

There are multiple turbulence models available with ANSYS-CFX for the Reynolds-averaged Navier-Stokes (RANS) equations. One equation, two equation, and algebraic Reynolds-averaged models can be used. The one equation models are based on an algebraic eddy viscosity while the two equation models are two transport equations. Two of the most widely used two equation models are the k-epsilon, (k-ϵ), and k-omega, (k-ω), turbulence models. The Reynolds stress is related to the mean velocity gradients and turbulent viscosity by using the gradient hypothesis method in both these models. To calculate the viscosity, the product of the turbulent length and velocity scales are used. [16]

The k-ϵ turbulence model gets its name from making use of the turbulent kinetic energy, k, and the turbulent dissipation rate, ϵ, as the basis for the two transport equations. This model is best used for free-shear flows that have a weak pressure gradient. This model is very sensitive to the grid resolution near walls. The results of this model will often be inaccurate if the flow is wall bounded and has a high pressure gradient. [17] The key attribute that relates this model to the Mentor SST model is the free stream independence.

The k-ω uses the turbulent frequency, ω, as apposed to the turbulent dissipation rate in the k-ϵ model for the basis of the two transport equations. This model is not as sensitive in the near wall regions and is numerically stable. This gives good results in the logarithmic region of the boundary layer. This model also does not make use of a non-linear damping function, unlike the k-ϵ model. Without a damping function, the model is more robust and stable. [16] This numerical stability is what relates the k-ω model to the Menter SST model. However, this model is sensitive to the conditions in the free stream unlike the k-ϵ model. [17]

These two models both fail whenever separation occurs, thus any flow simulations that have the potential for separation should not make use of these models. If the strengths of these two models are combined, a more robust and turbulence model can be developed. This is how the two equation Menter SST model was developed. The Menter SST model has both the free stream independence of the k-ϵ model and the numerical stability in the near wall region of the k-ω model. The resulting turbulence models are given by,

$$\frac{D\rho k}{Dt} = \tau_{ij}\frac{\partial u_i}{\partial x_j} - \beta^* \rho\omega k + \frac{\partial}{\partial x_j}[(\mu + \sigma_k \mu_t)\frac{\partial k}{\partial x_j}], \tag{2.6}$$

$$\frac{D\rho\omega}{Dt} = \frac{\gamma}{\nu_t}\tau_{ij}\frac{\partial u_i}{\partial x_j} - \beta\rho\omega^2 + \frac{\partial}{\partial x_j}[(\mu + \sigma_\omega \mu_t)\frac{\partial \omega}{\partial x_j}] + 2(1-F_1)\rho\sigma_{\omega^2}\frac{1}{\omega}\frac{\partial k}{\partial x_j}\frac{\partial \omega}{x_j}. \tag{2.7}$$

The SST model achieves highly accurate simulations until there is flow separation due to an adverse pressure gradient. The model does not account for the turbulent shear stress transport. This results in an over prediction for the eddy-viscosity. To overcome this problem a limiter can be used on the eddy-viscosity

$$\nu_t = \frac{a_1 k}{max(a_1 \omega_2 S F_2)}. \tag{2.8}$$

The limiter is implemented by using blending functions, which are based on the distance to the closest surface, y. The blending of $F1$ and $F2$ are pertinent for the success of the SST model [16]. Whenever the simulation is in the near wall region, the two functions should converge to unity and should be zero when far away from the surface. The blending functions are given by,

$$F_1 = tanh([min(max(\frac{\sqrt{k}}{0.09\omega y}, \frac{500\nu}{y^2\omega}), \frac{4\rho\sigma_{\omega^2} k}{CD_{k\omega} y^2})]^4), \tag{2.9}$$

$$F_2 = tanh([max(\frac{2\sqrt{k}}{0.09\omega y}, \frac{500\nu}{y^2\omega})]^2). \tag{2.10}$$

In equation (2.9), the term $CD_{k\omega}$ represents the cross diffusion given by,

$$CD_{k\omega} = max(2\rho\sigma_{\omega^2} \frac{1}{\omega} \frac{\partial k}{\partial x_j} \frac{\partial \omega}{\partial x_j}, 10^{-20}). \tag{2.11}$$

All computations in this thesis make use of the SST turbulence model.

2.4 Grid Generation

2.4.1 ANSYS-ICEM

ANSYS-Icem was used to create all the grids used to generate the simulations.

ICEM is a grid generation software package inside the ANSYS suite that is capable of creating advanced grids made up of complex geometry components and in turn creating optimized meshes. In order to create an optimized mesh, the geometry that is being modeled has to conform closely to the generated mesh. ICEM offers many formats and tools that allow this to happen. The offered mesh formats include, multiblock structured,unstructured hexahedral, unstructured tetrahedral, Cartesian with H-grid refinement, hybrid meshes, and quadrilateral and triangular surfaces. The unstructured hexahedral format was used to generate all meshes that were used in the present study. In addition to the multitude of formats, there is a mesh smoothing tool that helps alleviate the tedious effort of mesh refinement. The mesh smoothing tool allows the user to indicate a value for the quality that each element needs to meet, and then ICEM moves individual nodes until each element is at the desired value. [2]

2.4.2 Hexa Mesh

Inside ANSYS-ICEM there is a package, called Hexa, that allows for the generation of hexahedral meshes. Three dimensional, multi-block surface and volume meshes can be generated using Hexa. The meshes can also be either structured or unstructured. Hexa generates the block topology directly onto the CAD geometry. Tools within Hexa can then be used to better relate the block topology to specific parts of the geometry. This can be done by moving block vertices, associating edges with specific curves of the CAD geometry, and associating faces of the blocks to surfaces of the geometry. Hexa is a projection-based mesh generator, which means that edges and faces are associated to the nearest corresponding curve or surface automatically. [2] This useful feature allows for minimal manual block association. The blocks can also be altered by splitting edges, faces, or the block themselves. Furthermore, there are tools that allow the blocks to be rotated, translated, scaled, or copied.

There are three block types that can be used within HEXA. They are mapped/structured, swept, and free unstructured. A visualization of the block types can be seen in Figure 2.1. Different block types are better used for different models. The mapped/structured blocks are used for both the fluidic injectors in a supersonic boundary layer and the military-style nozzle.

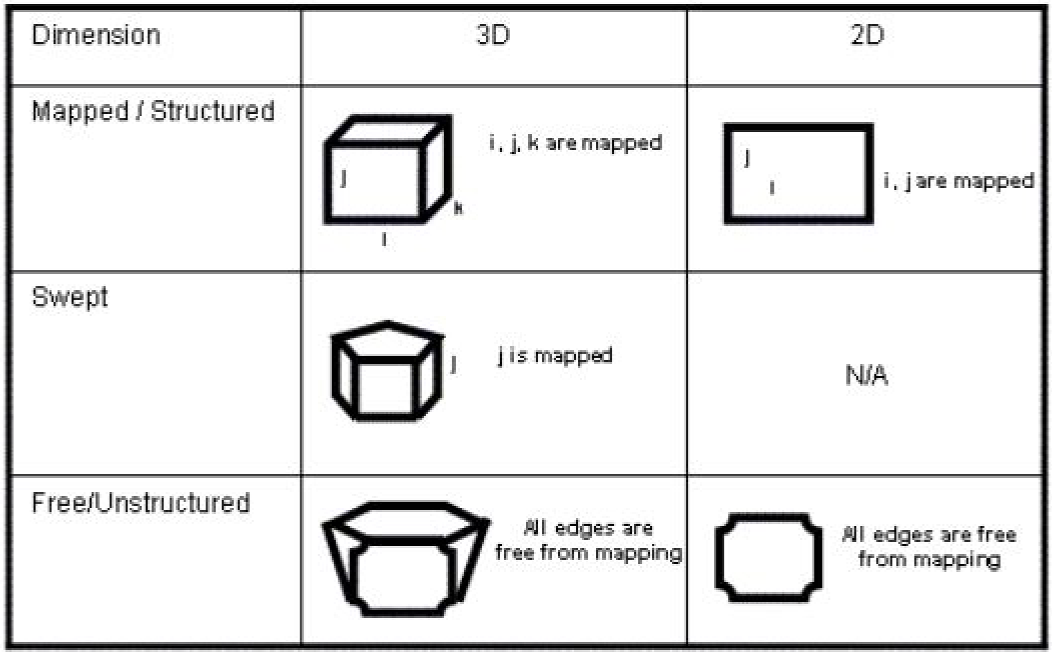

Figure 2.1. Block Types Offered in HEXA [2]

Whenever a circular geometry is being meshed an O-grid needs to be used. A circular geometry generates singularities that create problems for the numerical solver. An O-grid overcomes this problem by taking a single block and splitting it into five separate blocks, which is demonstrated in Figure 2.2. O-grid generation is automatic in ICEM with the O-grid interactive tool. The user only has to select the block to alter and then the desired faces to associate to the surface if necessary.

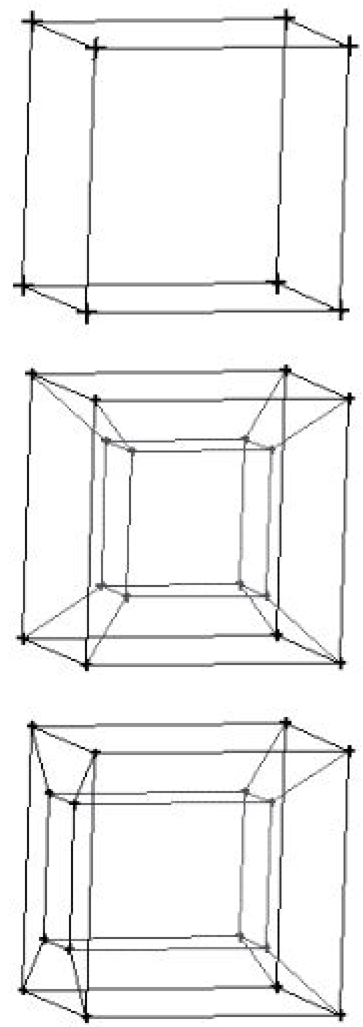

Figure 2.2. Single unalterd block, O-grid, O-grid with Face Association [2]

The quality of the pre-mesh can be checked within ICEM. The two most useful parameters to check are the determinant and the minimum angle of the cells. The determinant is used to check the deformation of the mesh by computing the Jacobian of each hexahedron and normalizing it with the determinant of the corresponding matrix. The values of the determinant range from zero to one, where zero is an inverted cell with a negative volume and one is a perfect cube. It is good practice to have all cells have a determinant of 0.2 or greater, but ANSYS-CFX has been shown to work at values of 0.1 with little problems. The minimum angle is a measure of internal angle deviation and the skewness of the cell. The smaller the angle the less effective the numerical solver will be. It is good practice to have the angle be above 18°, but ANSYS-CFX can operate safely around 14°. [2]

2.5 Simulation Strategy

Past simulations were performed using Wind-US and then later ANSYS-CFX. These original runs were of a high-speed military jet nozzle with the addition of rectangular injectors. This design did not match the experiments, as the experiments made use of circular injectors. The rectangular injectors made the mesh generation easier. The mesh was generated using Pointwise Gridgen and run using Wind-US. The decision was then made to have circular injectors to better match the experiments. The mesh generation became more complex because of the cylindrical interface on a Cartesian surface. Problems with Wind-US also appeared. These factors lead to the decision to use ANSYS-CFX and ANSYS-ICEM.

The previous completed simulations gave a lot of knowledge and familiarity of how ANSYS-CFX and ANSYS-ICEM work. However, the military nozzle mesh and results are highly complex and have a large wall clock time to execute. Due to the long computation times and complexity of the military nozzle, a supersonic boundary layer was used to see the effect of a change in the injectors on the fluidic insert. Specifically, the effect of the addition of a third injector and a change of angle on the downstream injector were examined. The supersonic boundary layer was computationally less expensive and had a much faster wall clock time. This allowed for quicker understanding of the changes and if they merited being added to the military style nozzle.

For this thesis previous simulations were used to look for a correlation between noise reduction and flow parameters. In these cases the upstream injector was always at a 45° angle and the downstream injector was at a 90° angle relative to the jet centerline. The injectors also had the same diameter. Also, a third injector was added to the military style nozzle mesh. In these cases the middle injector was at 45° and the upstream and downstream injectors remained at the same angles as before. The area ratio for the injectors were 1, 2, and 4, for the upstream, middle, and downstream injectors, respectively. The meshes were also scaled so there would be an increase in Reynolds number to follow along with the experiments.

This section provides the boundary conditions for the computational domain and the different input conditions for the fluidic inserts and the core flow. The dimensional properties of the geometry and mesh parameters are also provided.

2.5.1 Three Fluidic Injectors in a Supersonic Boundary Layer

To understand the effect of the addition of a third injector, a study was preformed by adding a third injector to the existing supersonic boundary layer mesh. The injector spacing changed to 20%, 50%, and 70% of the divergent section of the nozzle length from the the previous 30% and 70%. The injector area ratio also changed from 1 to 1, to 1:2:4. Figure 2.3 illustrates the supersonic boundary layer with three fluidic injectors entering the freestream at 45°, 45°, and 75° respectively. There are also meshes that have a 60°, 90° with and without a bend, and the original two injector mesh. The upstream injection pressure ratio is labeled as IPR_1, while the middle and downstream injection pressure ratios are labeled as IPR_2 and IPR_3. The computational domain spanwise length and height are $100D_{Nozzle}$ while the streamwise length is $200D_{Nozzle}$. The outer domain extends enough so that the flow from the injectors are independent of the outer boundaries. This is important for the Menter SST turbulence model to operate correctly due to the dependence on freestream conditions.

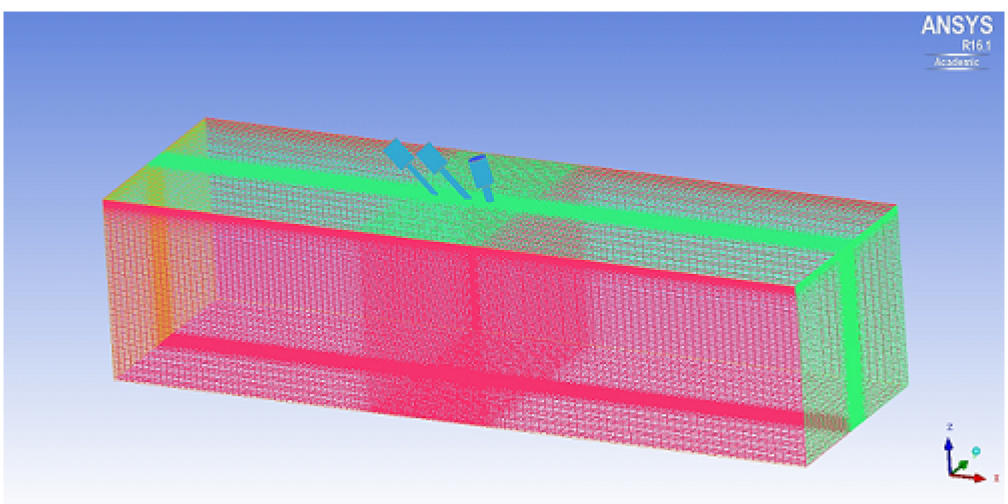

Figure 2.3. Full computational domain for three injectors in a supersonic boundary layer

The mesh is an unstructured mesh composed of quads and hexas. The mesh is a single domain and independent of the number of blocks in the model. All block interfaces are merged. There is little complexity in the mesh, and the most complex part is where the injectors interface with the wall of the flat surface.

The boundary condition for the inlet for all simulations was set to a Mach number of 1.5. The inlet can be seen in Figure 2.4. To ensure numerical stability the sides and bottom of the computational domain were given a streamwise velocity and maintained a static pressure condition of 101008 Pa and a temperature condition of 288 K. This is shown in Figure 2.5. The flow then travels out of the supersonic outlet boundary illustrated in Figure 2.6.

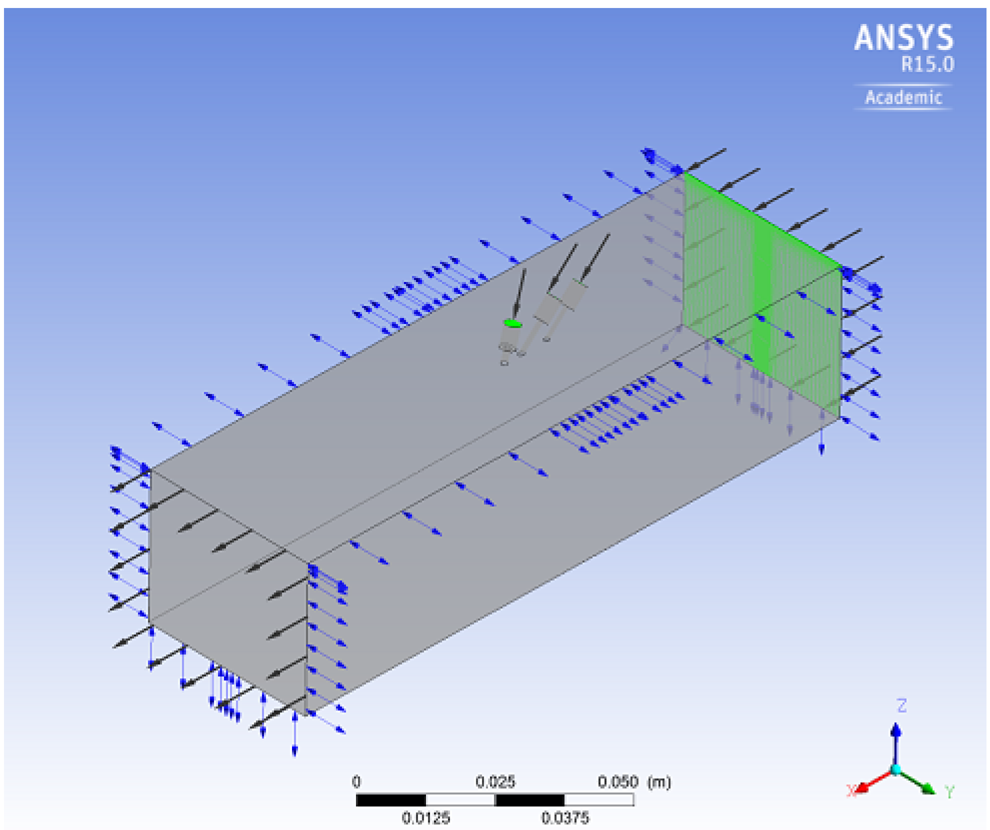

Figure 2.4. Inlet boundary condition for supersonic boundary layer with fluidic injection

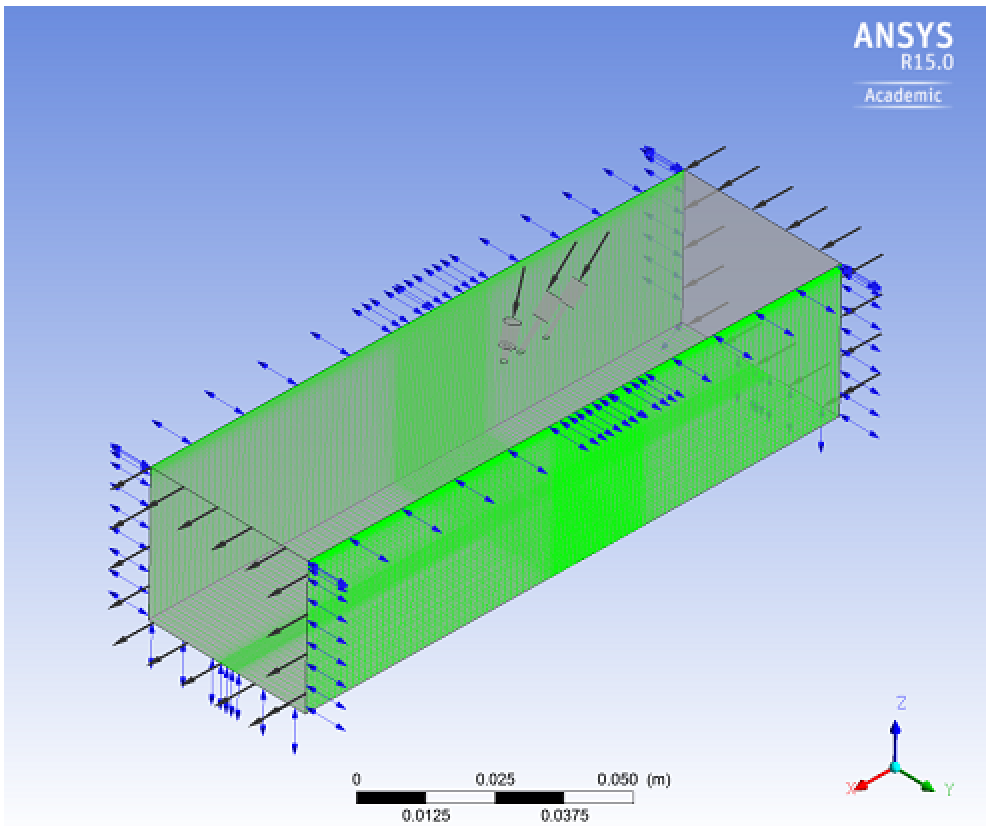

Figure 2.5. Freestream boundary conditions for supersonic boundary layer with fluidic injection

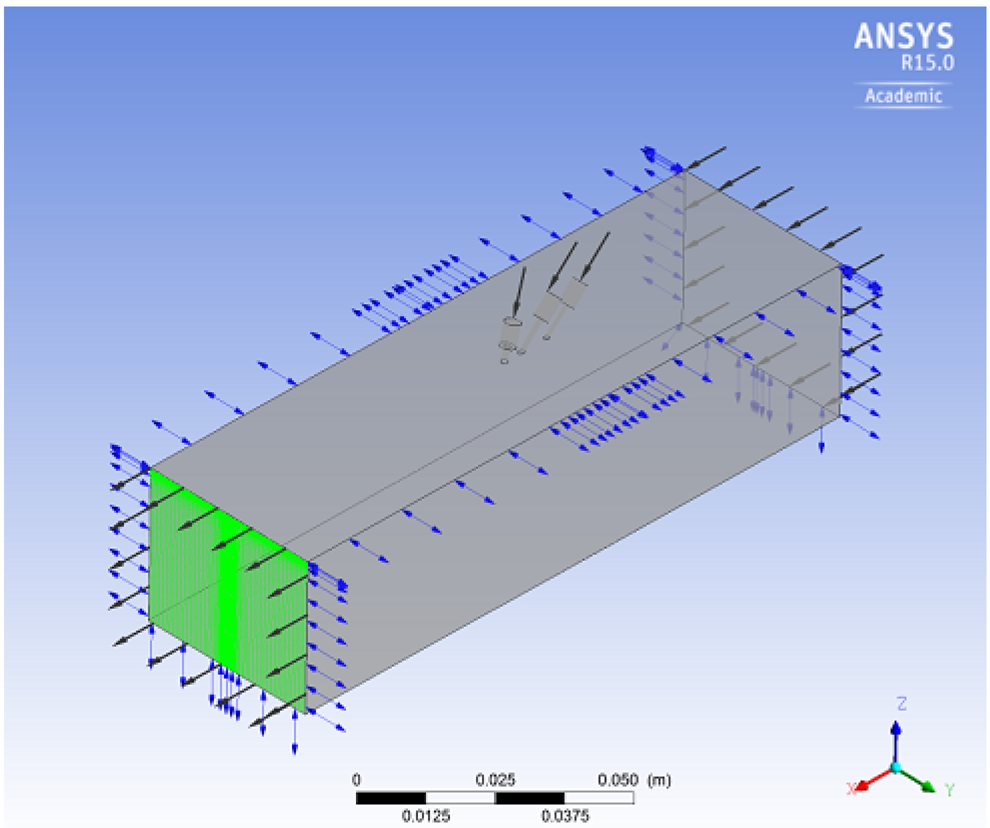

Figure 2.6. Outlet condition for supersonic boundary layer with fluidic injection

The flat surface of the supersonic boundary layer is a no-slip adiabatic wall. It begins $50D_{Nozzle}$ before the upstream injector. Because of this, the boundary layer can grow adequately. The walls of the injectors are also adiabatic, no-slip walls. The wall boundary conditions are illustrated in Figure 2.7. The inlet conditions for the injectors is specified by the total pressure, total temperature, and flow direction. The injection pressure ratios (IPR), P_0/P_1, as well as other operating conditions for all relevant simulations are listed in Table 2.5.1.

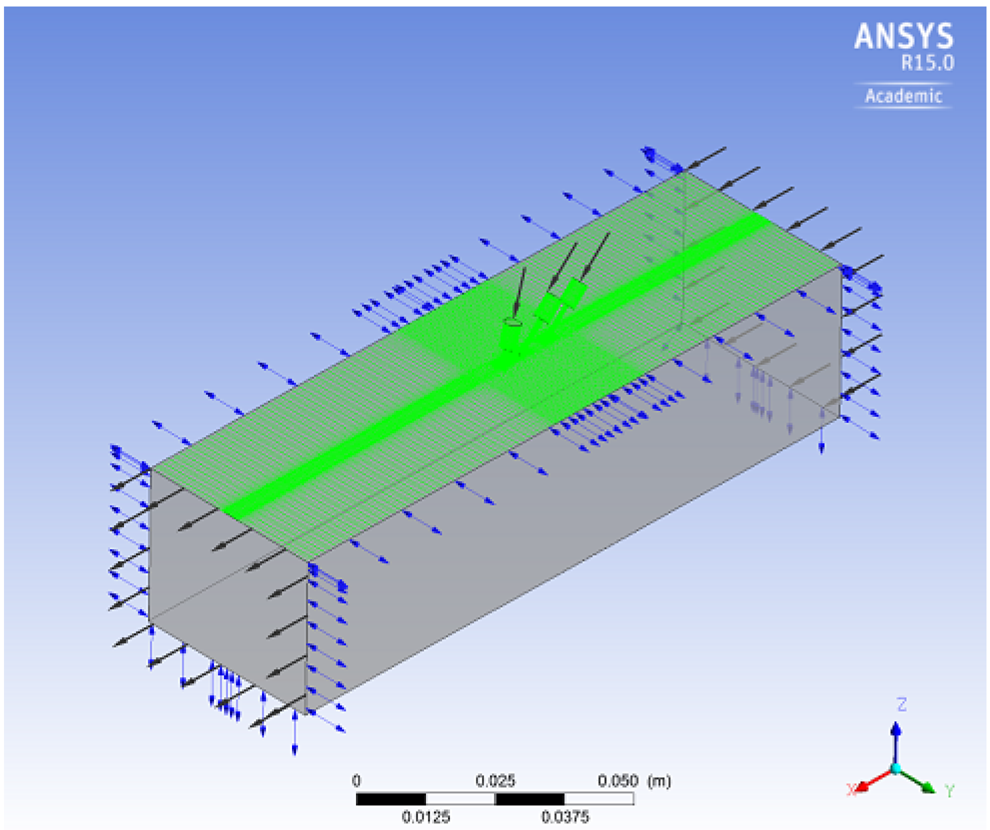

Figure 2.7. Wall boundary conditions for supersonic boundary layer with fluidic injection

Supersonic Boundary Layer Conditions					
M	TTR	All IPR	Inj_1 Angle	Inj_2 Angle	Inj_3 Angle
1.5	1	2.7	45	45	60
1.5	2	2.7	45	45	75
1.5	3	2.7	45	45	90 with 45 degree bend
1.5	4	2.7	45	45	90 without bend

Table 2.1. Supersonic Boundary Layer Operating Conditions

2.5.2 Military Style Nozzle Baseline and with Fluidic Inserts

The meshes used in this thesis were created by altering the original meshes used in previous research by Kapusta [18]. The original meshes included a baseline case with no fluidic inserts and a nozzle with 3 fluidic inserts with two injectors per insert. The injectors had the same hole diamater and were located at 30% and 70% of the nozzle diverging section. The upstream injector is at an angle of 45°and the downstream is at 90°. The nozzle exit diameter, D_{exit}, was 0.885 inches which corresponds to the Generation 1B nozzle. The mesh is a single domain unstructured mesh and consists only of hexahedral and quadrilateral cells. There were approximately 12.7 million nodes. The completed simulation results for this mesh were further analyzed in this thesis to find a correlation between noise reduction and flow parameters. The operating conditions for these simulations can be seen in Table 2.2.

Generation 1B Conditions for Past Nozzle Simulations				
NPR	Case Number	M_J	IPR_1	IPR_2
3.0	1	1.36	1.5	1.9
3.0	2	1.36	1.5	3.0
3.0	3	1.36	1.5	4.5
3.0	4	1.36	1.8	2.4
3.0	5	1.36	1.8	3.7
3.0	6	1.36	2.1	1.9
3.0	7	1.36	2.1	3.0
3.0	8	1.36	2.1	4.5
3.0	9	1.36	2.4	2.4
3.0	10	1.36	2.4	3.7
3.0	11	1.36	2.7	1.9
3.0	12	1.36	2.7	3.0
3.0	13	1.36	2.7	4.5

Table 2.2. Generation 1B Conditions for Past Nozzle Simulations

The mesh was then altered to include an additional middle injector. The three injectors were located at 20%, 50%, and 70% of the diverging section. The two upstream and middle injectors are at an angle of 45° while the downstream injector is at 90°. The area ratio of the injector holes were 1:2:4 starting with the upstream injector. The addition of the middle injectors increased the number of nodes to approximately 13.7 million nodes.

The mesh was also altered to have an increase in scale. The exit diameter was scaled to be 1.06 inches from 0.885 inches to achieve the Generation 2 nozzle size. The nozzle was then scaled to 5.07 inches, which is the nozzle size used in the GE experiments. The full computational domain of the Gen 2 nozzle can be seen in Figure 2.8.

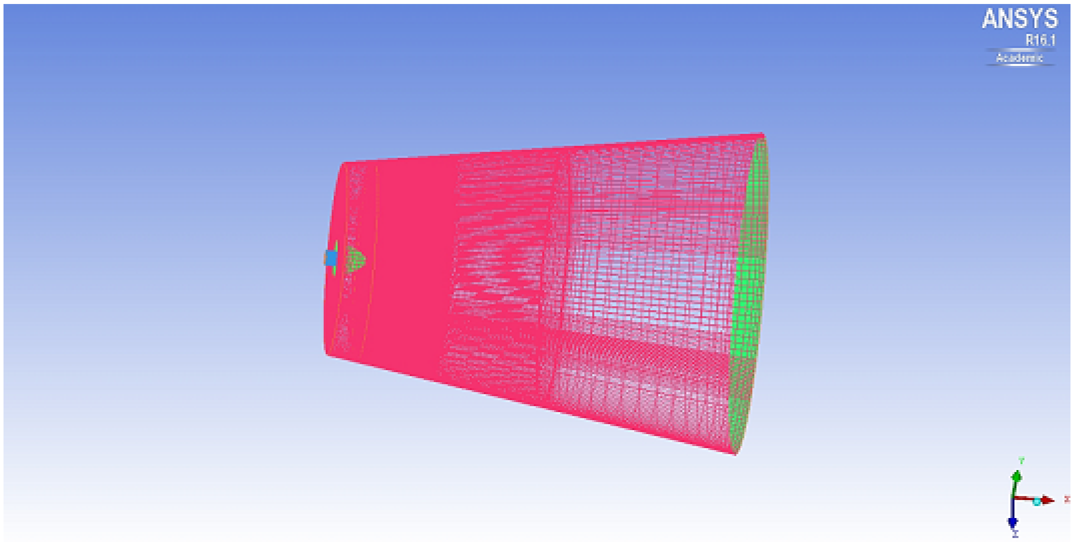

Figure 2.8. Fluidic insert 3 injector Generation 2 nozzle whole domain

The boundary conditions for each simulation were set to be the same for all meshes, except the injector inlet conditions. Only the boundary conditions for the Gen 2 nozzle will be shown due to the similarity of all meshes. The outer computational domain consists of an opening and outlet boundary conditions. The opening boundary condition specified the ambient static pressure to be 101,008 Pa and the temperature to 288 K. It also had a streamwise Mach number of 0.1. The opening condition surrounds the entire domain until it reaches the outlet boundary condition, which can be seen in Figure 2.9. The outlet boundary condition is specified to be in the subsonic flow regime and the average static pressure over the domain area. The outlet boundary is illustrated in Figure 2.10.

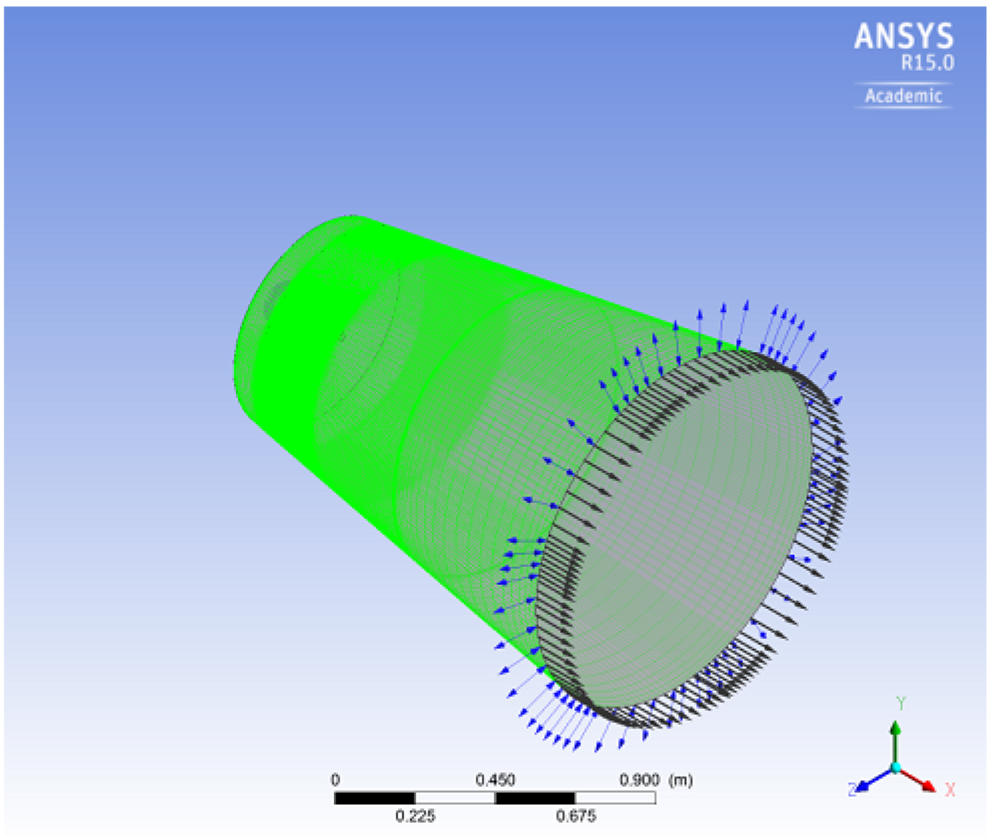

Figure 2.9. Opening condition for Generation 2 nozzle with 3 fluidic injectors per fluidic insert

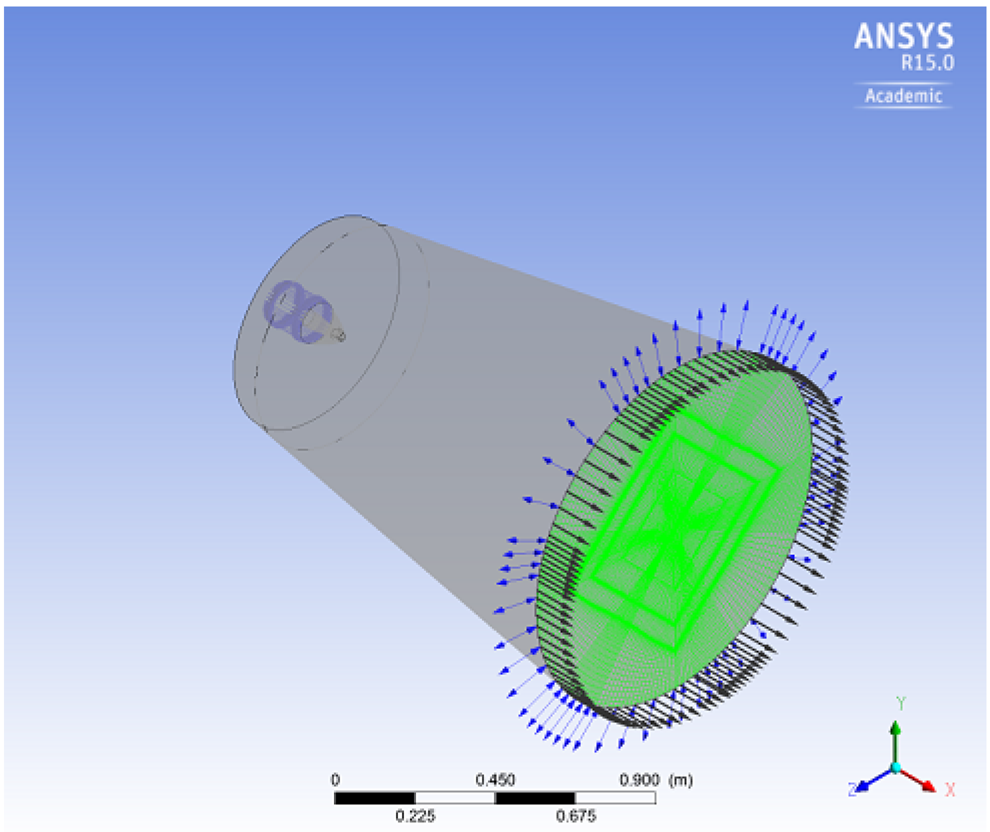

Figure 2.10. Outlet condition for Generation 2 nozzle with 3 fluidic injectors per fluidic insert

The nozzle wall is a no slip, adiabatic wall boundary condition. The nozzle lip is also a no slip, adiabatic wall. The CD nozzle can be seen in Figure 2.11.

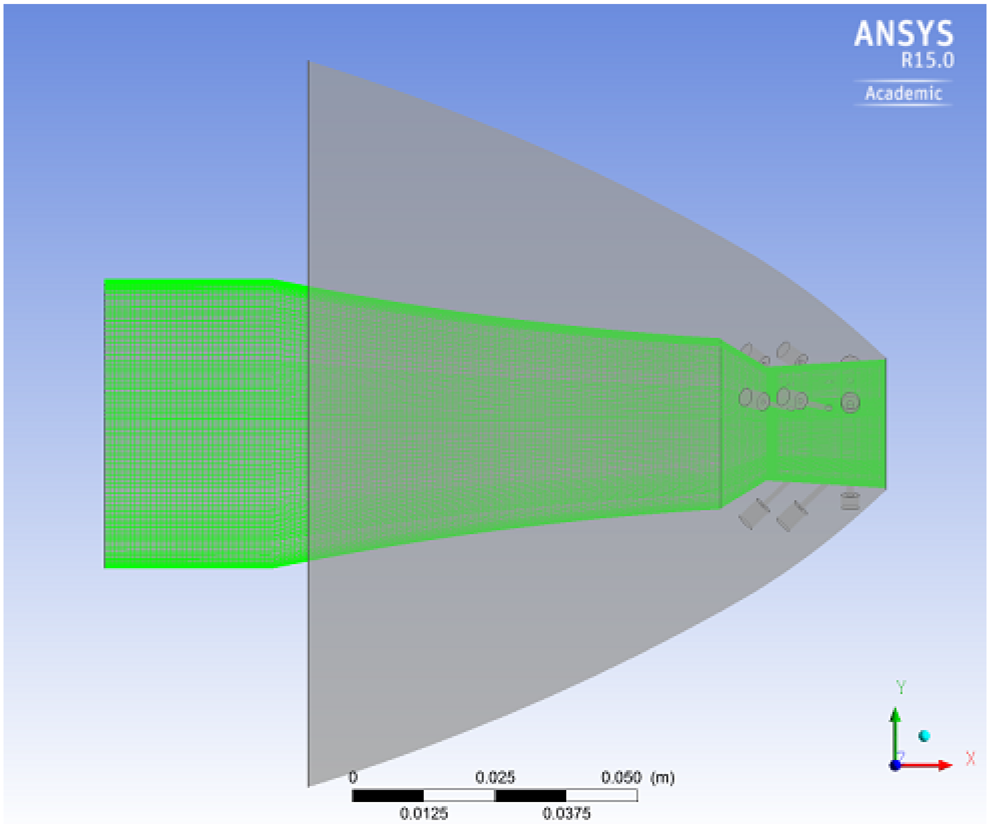

Figure 2.11. Nozzle wall condition for Generation 2 nozzle with 3 fluidic injectors per fluidic insert

The nozzle shroud was designed so it would completely encompass all of the fluidic injectors. Whenever the injectors were not inside of the shroud, ANSYS-CFX would encounter a problem and pull the flow in the freestream through the injectors. This would cause convergence issues. The shroud does differ from the one used in experiments. In the case of numerical simulations there is no gap between the nozzle lip and the shroud. The experimental nozzle and shroud have a small gap between them. The gap was ignored due to the complexity it would add to the mesh. Also the purpose of the shroud is to smooth the flow over the nozzle by specifying an inviscid wall boundary condition which is seen in Figure 2.12.

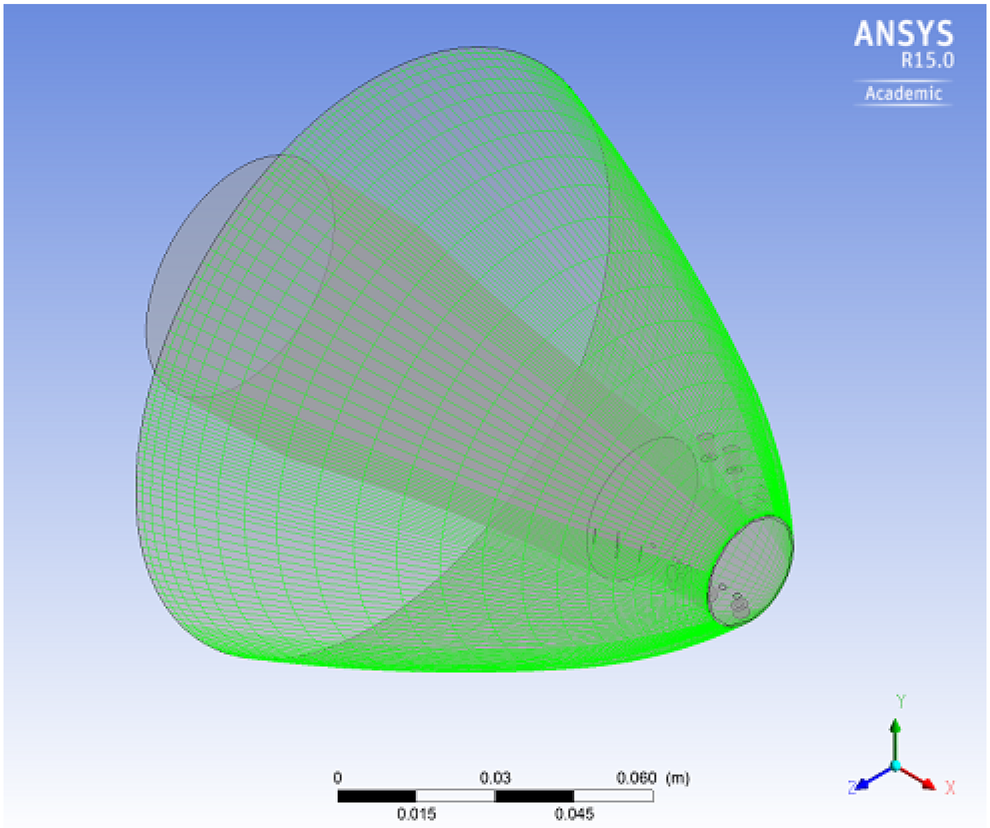

Figure 2.12. Shroud inviscid wall condition for Generation 2 nozzle with 3 fluidic injectors per fluidic insert

The inlet boundary condition was set to have an NPR of 3 for all simulations. This corresponds to a M_j of 1.36, which is an over-expanded jet condition. A TTR of 3.0 and 1.0, where 1.0 is an unheated jet, were used in all Gen 1B and the GE test scale cases. A TTR of 2.5 and 1.0 were also used for the Gen 2 cases. A TTR of 2.5 was used because of the limited amount of helium that could be used in the experimental cases. The inlet boundary condition can be seen in Figure 2.13.

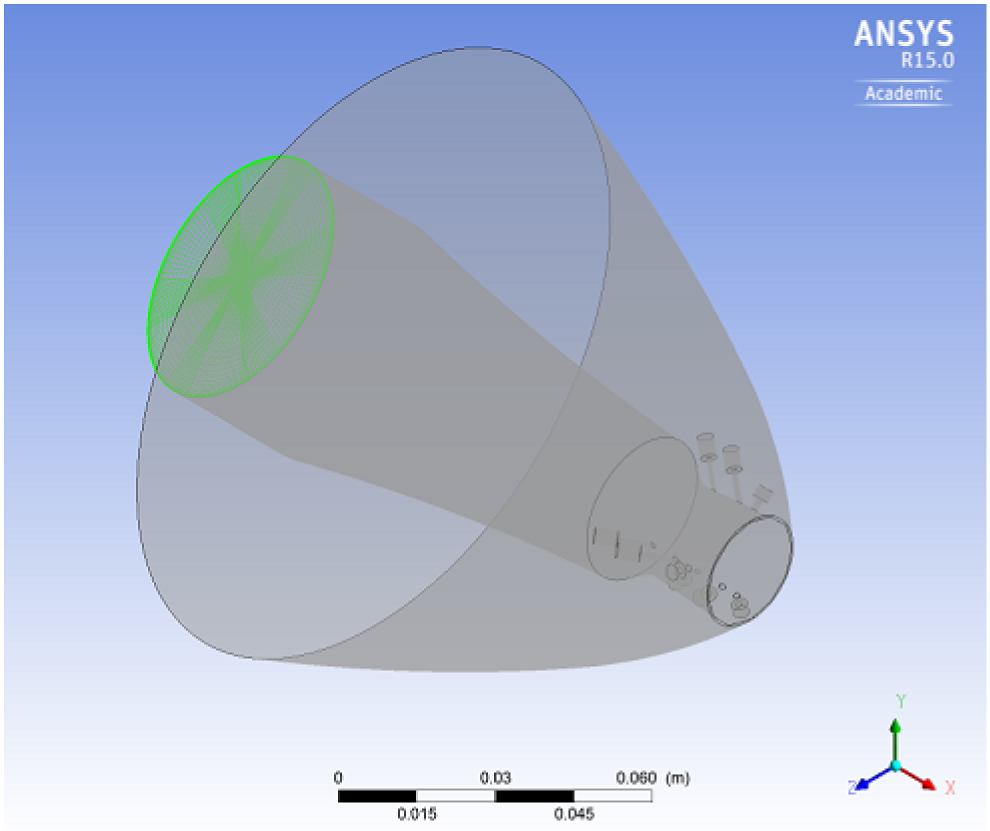

Figure 2.13. Inlet condition for Generation 2 nozzle with 3 fluidic injectors per fluidic insert

The fluidic injectors' locations and angles for each mesh were specified earlier in this section. The Gen 2 injectors can be seen in Figure 2.14. The interface between the injectors and the nozzle wall are perfectly matching. As seen in the previous figures in this section, the mesh is not completely symmetrical. This is because of the complex O-grid blocking structure that is inside the nozzle and the injector and where they interface. A close up of the interface O-grid can be seen in Figure 2.15. The injectors are made up of a larger diameter portion and a smaller diameter portion. The larger component is to represent the feed tube of the experiments that supply the injector. The walls of the injectors are the same as the nozzle wall, no-slip and adiabatic. The inflow is specified by total pressure, total temperature, and flow direction. The TTR for all injector inlets was 1.0 as the injection air was unheated.

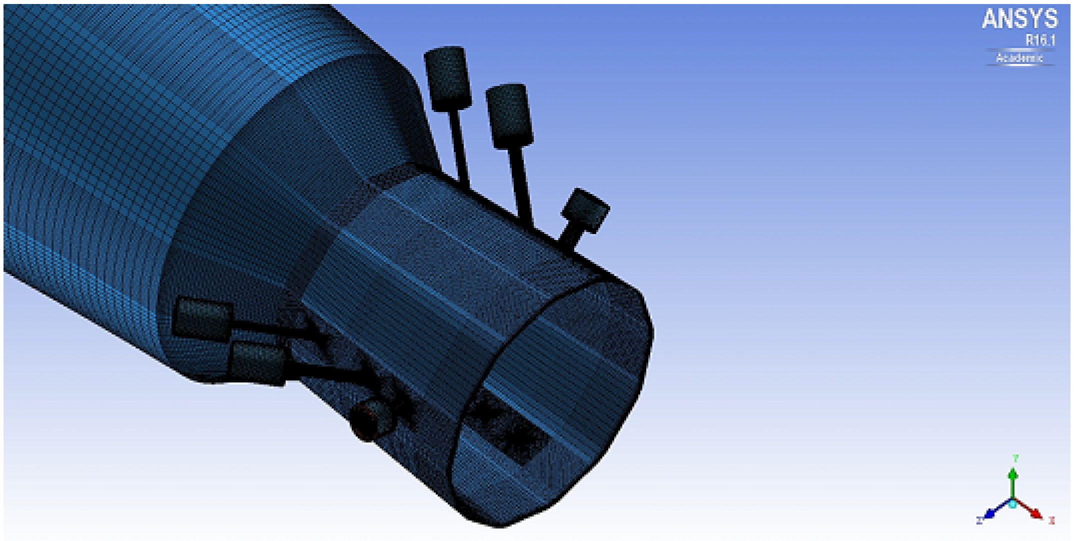

Figure 2.14. Fluidic Injector boundary condition in nozzle computational domain for Generation 2 nozzle

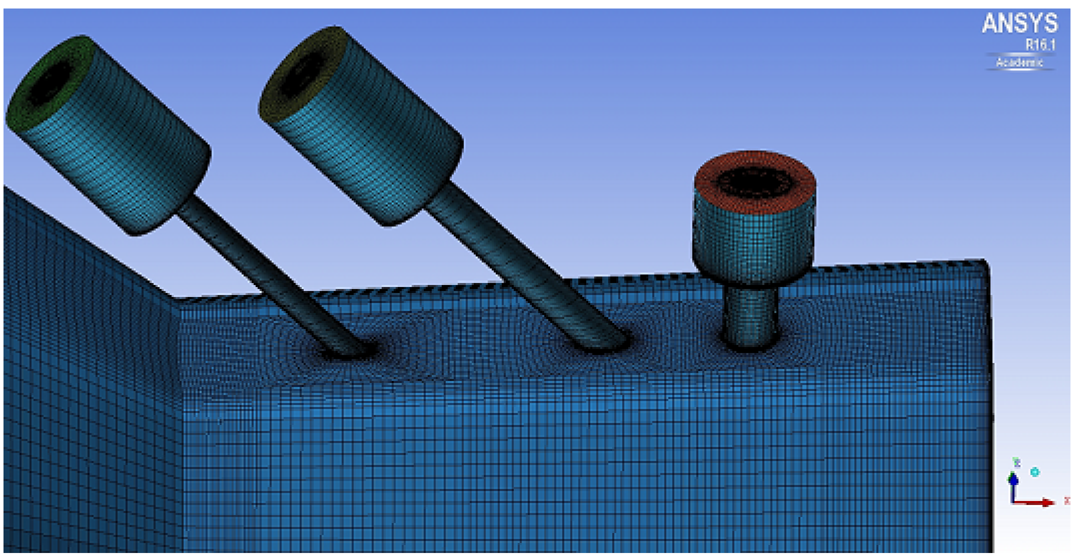

Figure 2.15. Close up of O grid around fluidic injector for Generation 2 nozzle

The numerical methods used were discussed in this chapter. A description of the RANS governing equations was given. The numerical solver ANSYS-CFX was also described. The Menter SST turbulence model's characteristics, advantages, and disadvantages were discussed. A description of the grid generation software package ANSYS-ICEM and its features were given as well as the general simulation strategy for each geometry.

The next chapter will will give a description on the generated numerical simulations for a simple geometry and a more complex geometry. The simple geometry is a supersonic boundary layer with three injectors exhausting into the freestream. This geometry will be used to give a description of the flow field generated by the fluidic inserts. A study will also be discussed on the effect of a change in downstream injector angle. The more complex geometry is a high speed military style nozzle with fluidic inserts. A comparison between a two injector and three injector per fluidic insert will be discussed. The results of a study on an increase in Reynolds number will also be discussed. The findings of an attempt to correlate noise reduction to flow parameters is also given.

Chapter 3
Numerical Simulations

Past studies have determined that the simulations give accurate results when compared to experimental measurements [3]. This section describes a study of fluidic injection into a supersonic boundary layer, and a military-style nozzle with fluidic inserts, and attempts to find a correlation between observed noise reduction and flow parameters. The supersonic boundary layer is discussed first. This will give a background of the flow field generated by a fluidic insert. The supersonic boundary layer is not as complex as the nozzle flow and it is easier to distinguish the characteristics of the flow. The flow of the military-style nozzle is then shown and the different meshes are compared. There is a comparison between a two and three injector nozzle, a study on the effect of an increase of Reynolds number, and an attempt to find a correlation between observed noise reduction and nozzle flow parameters.

3.1 Fluid Insert over Supersonic Boundary Layer

The numerical simulations for a supersonic boundary layer with fluidic injectors were performed using ANSYS-CFX. These simulations were performed to specifically to look at the effect of fluidic injectors on the core flow field within the jet nozzle and the effect of a change of downstream injector angle. A study of the effect of a change in downstream injector angle makes use of the supersonic boundary layer because it is simpler than the military-style nozzle and quicker to run. The lack of pressure gradient in the supersonic boundary layer is not a problem as the results are found to be very similar to those for the military-style nozzle.

The injectors have equivalent spacing and diameters to those in the military style nozzle. They are located at 20%, 50%, and 70% of the diverging section. The downstream injector has a diameter, $D_{inj3} = 0.053$ inches. The middle injector has an area of half the downstream injector and the upstream injector has an area of a quarter of the downstream injector. The injectors are connected to a larger tube which has a diameter of 0.125 inches to better replicate the experiments. The upstream and middle injectors are at an angle of 45° to the centerline. The downstream injector angle is set to 60°, 75°, 90° with a 45° bend, or 90° without a bend depending on which mesh is used.

This section will discuss the flow field generated by the fluidic injectors. The visual background in this study will provide an understanding of the complex flow. After understanding the basic flow field, a study is performed on the effect of a change in downstream injector angle.

3.1.1 Description of Flow Field Generated by Fluidic Inserts

The numerical schlieren of three fluidic injectors into a supersonic boundary layer shows bow shocks forming in front of each injector. Then there are expansions directly behind the injectors. Figure 3.1 illustrates these characteristics. The IPR of each injector is equal to 2.7. And the physical dimensions of the injectors are the same as described in the previous section.

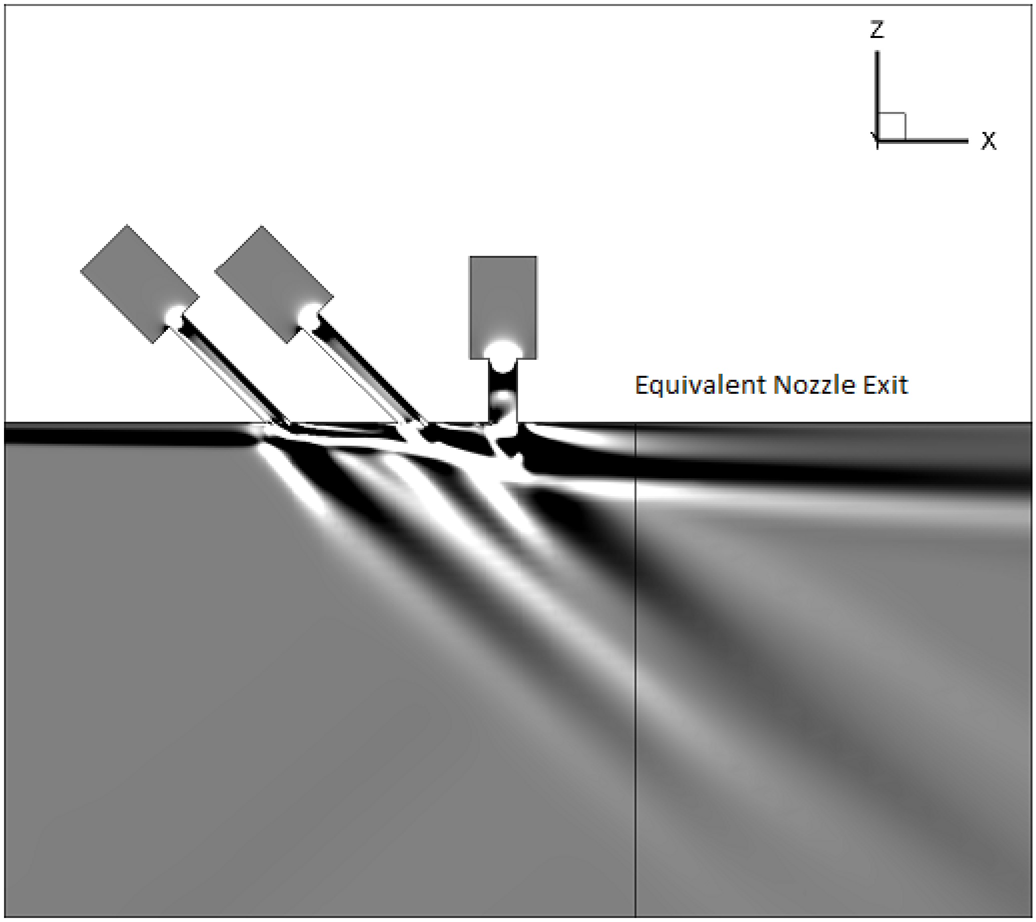

Figure 3.1. Numerical Schlieren of three injectors into a supersonic boundary layer with all $IPR = 2.7$

The effect of the shocks and expansions on the velocity field can be seen in Figure 3.2. There is a decrease in speed when traveling through the bow shocks. However, the flow does remain supersonic. A high velocity region is also found directly behind each injector port. This is the expansion around the corner of the injector into the supersonic freestream. There is also a region of very low velocity behind the high velocity region for the middle and downstream injector. The low velocity region in between the middle and downstream injector is due to a recirculation of the flow. The low velocity region behind the downstream injector occurs because the flow has separated from the wall.

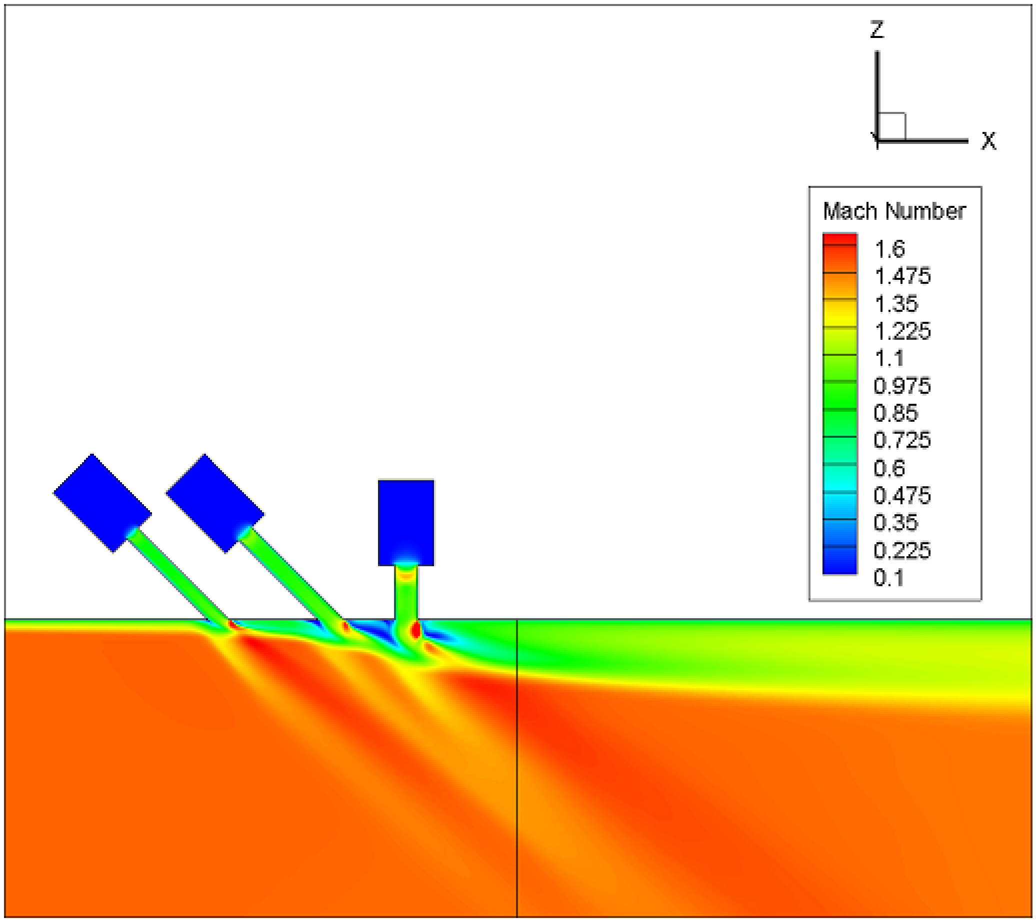

Figure 3.2. Mach number contour of three injectors into a supersonic boundary layer with all $IPR = 2.7$

Using the supersonic boundary layer as an example, a parameter to distinguish the shape of the fluidic insert can be found. Streamlines can be used to find this parameter. The two properties that have been found to best describe the insert shape are the total pressure and the total temperature. Figure 3.3 shows these two properties. However, if the jet is unheated, TTR equal to 1.0, then the only property that can be used to visualize the shape is the total pressure. The separation of flow from the wall can also be easily seen in Figure 3.3(a) as the dark blue region behind the downstream injector.

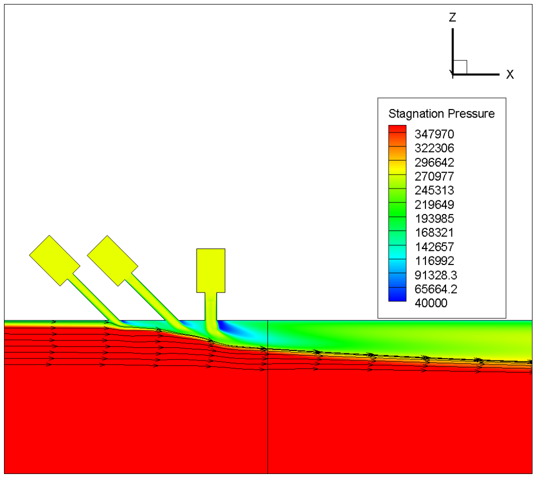

(a)

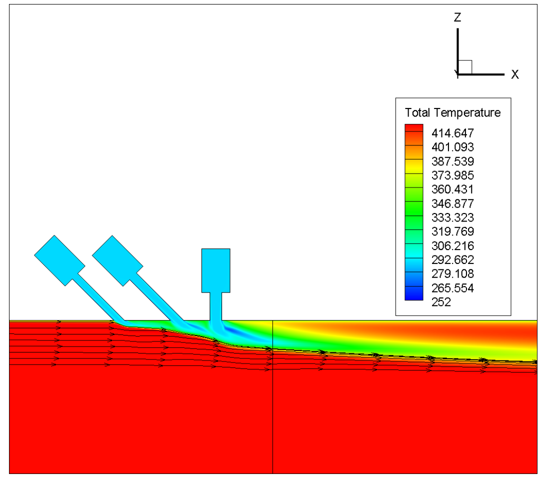

(b)

Figure 3.3. Streamlines of fluidic insert shape with conditions M = 1.5, TTR = 1.45, and all IPR = 2.7: (a)Total pressure contours, (b) Total temperature contours

One of the goals of using fluidic inserts is to match the shape of the hard wall corrugations. The purpose of the first injector is to slightly deflect the core flow and reduce the momentum behind the injector. The shape of the hard wall corrugation starts off thin and gradually increases so deep penetration by the first injector is not necessary. The same can be said about the middle injector. It is primarily used to help smooth the shape between the upstream and downstream injector. Whenever only two equal sized injectors are used there is a sudden increase in penetration as opposed to a gradual increase, which can be seen in Figure 3.4. Another interesting observation is that the two cases appear to have the same downstream penetration even though the IPR_2 of the simulation with two injectors is much greater than the respective IPR of the three injector simulation. This can be attributed to the middle injector further reducing the momentum of the flow allowing the downstream injector to penetrate further into the core flow, when compared to a two injector system.

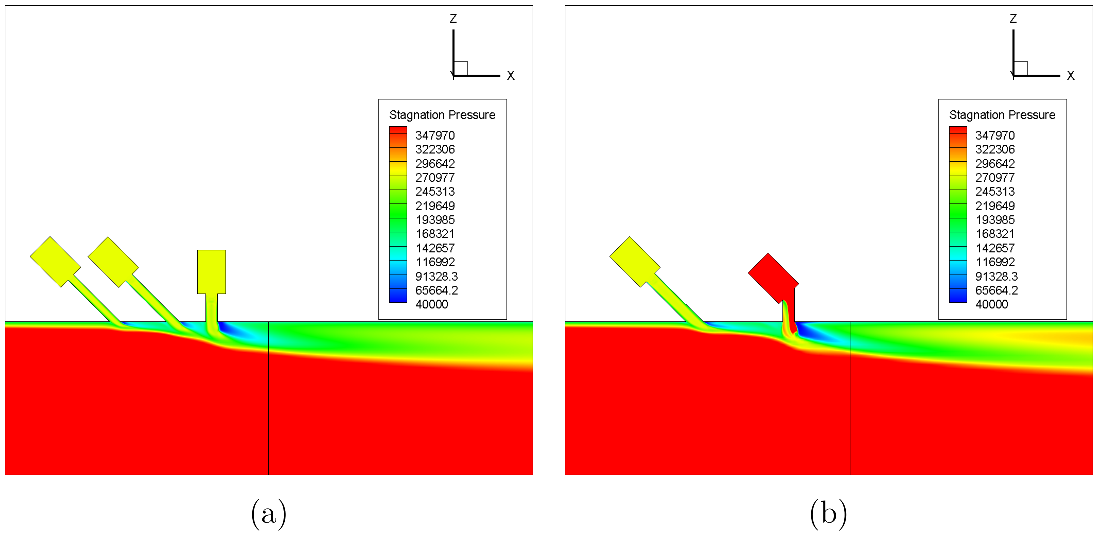

Figure 3.4. Comparison of streamlines of fluidic insert shape with conditions M = 1.5 and TTR = 1.45: (a) 3 injectors all $IPR = 2.7$, (b) 2 injectors $IPR_1 = 2.7$ $IPR_2 = 4.5$

Cross stream slices have been taken to understand how the flow evolves in the downstream direction. The slices are taken at the following locations downstream of the last injector, $0D_{inj}$, $1D_{inj}$, $3D_{inj}$, and the equivalent nozzle exit. The flow parameters that are analyzed are the total pressure, Mach number, and streamwise vorticity. There is also a line that appears in the middle of the slices which represents the equivalent jet centerline.

When comparing the fluidic inserts to the hard wall corrugations, it is important to understand how the injected fluid interacts with the core flow. In the case of the hard wall corrugations there are no fluid-to-fluid interactions that are present with the fluidic inserts. The total pressure gives a visualization of the penetration into the core flow and spreading of the fluidic insert. The Mach number provides insight into how the fluidic insert changes the speed of the core flow. The interactions between the fluidic inserts and core flow create a strong, high amplitude pair of streamwise vortices. These are confined to the fluidic insert, whereas they occur outside the hardwall corrugations.

As stated earlier the total pressure gives an accurate visual description of the shape of the corrugation. The downstream evolution of the corrugation can be seen in Figure 3.5. The first noticeable difference between the fluidic insert and hardwall corrugation is that the fluidic insert is not nearly as thin. The hardwall corrugations can be seen in Figure 3.6. It is more bulbous and becomes more circular the further downstream. As seen in Figure 3.5(c) and (d), the fluidic insert begins to separate from the flat wall. The initial penetration from the downstream injector can be seen in Figure 3.5(a). The dark blue region at the $1D_{inj}$ slice is the separation seen in the streamwise slice in Figure 3.3t.

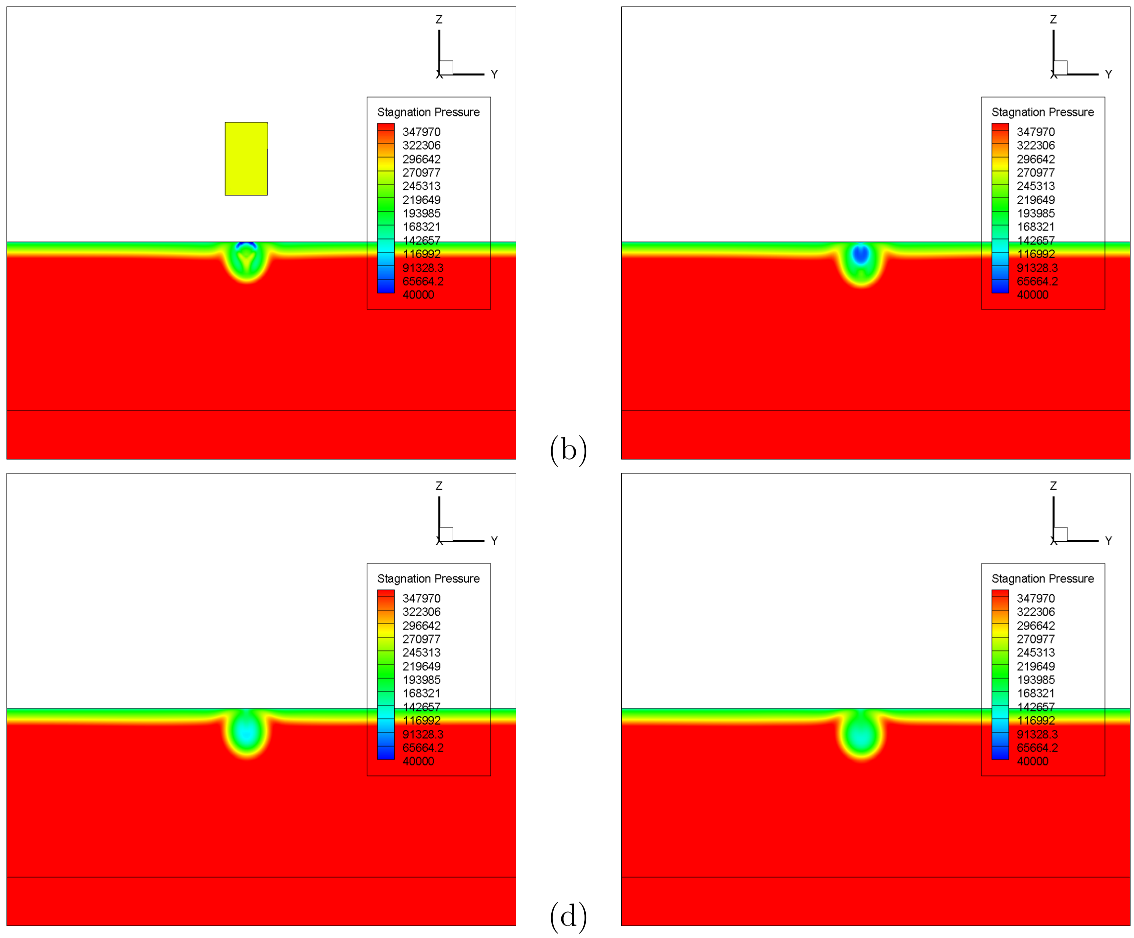

(a) (b) (c) (d)

Figure 3.5. Downstream evolution of total pressure of three injectors into a supersonic boundary layer M = 1.5, TTR = 1.45, and all IPR = 2.7: (a) $0D_{inj}$, (b) $1D_{inj}$, (c) $3D_{inj}$, (d) Nozzle Exit

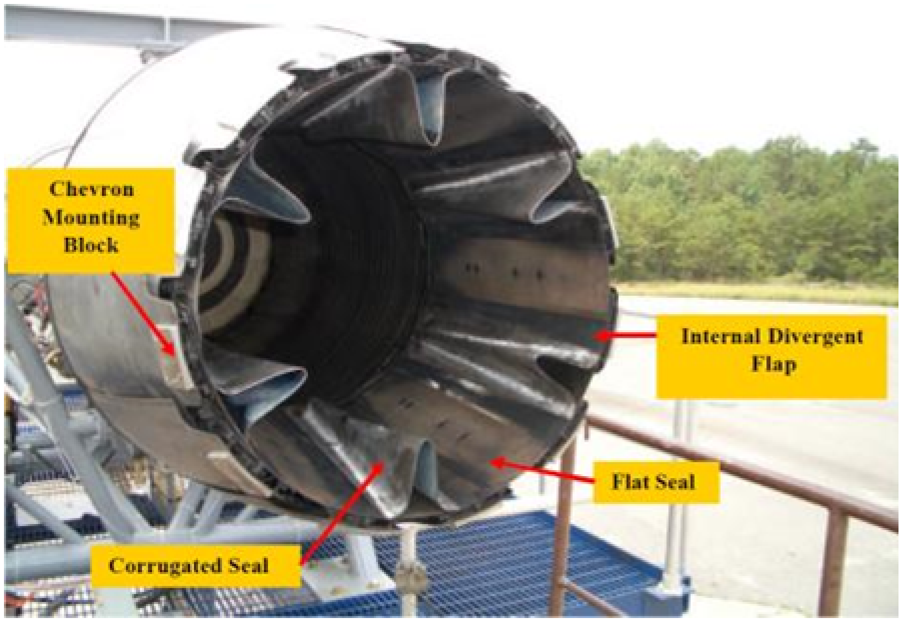

Figure 3.6. Photograph of a nozzle with the addition of hardwall corrugations [5]

The Mach number provides good insight into the changes of speed in the flow. At the point of injection as seen by Figure 3.7(a), there is a region of slower supersonic flow compared to the core flow speed. It appears in a "U" shape around the fluidic insert. This is caused by the bow shock that appears in front of the injector. The bow shock's effect can be seen to increase in size while appearing farther away from the fluidic insert as the nozzle exit is approached. An expansion can also be seen directly behind the injector, Figure 3.7(a), and then the flow quickly separates as indicated by the blue region, Figure 3.7(b). However, the flow speed continues to increase in Mach number around the fluidic insert and exceeds the freestream Mach number of 1.5.

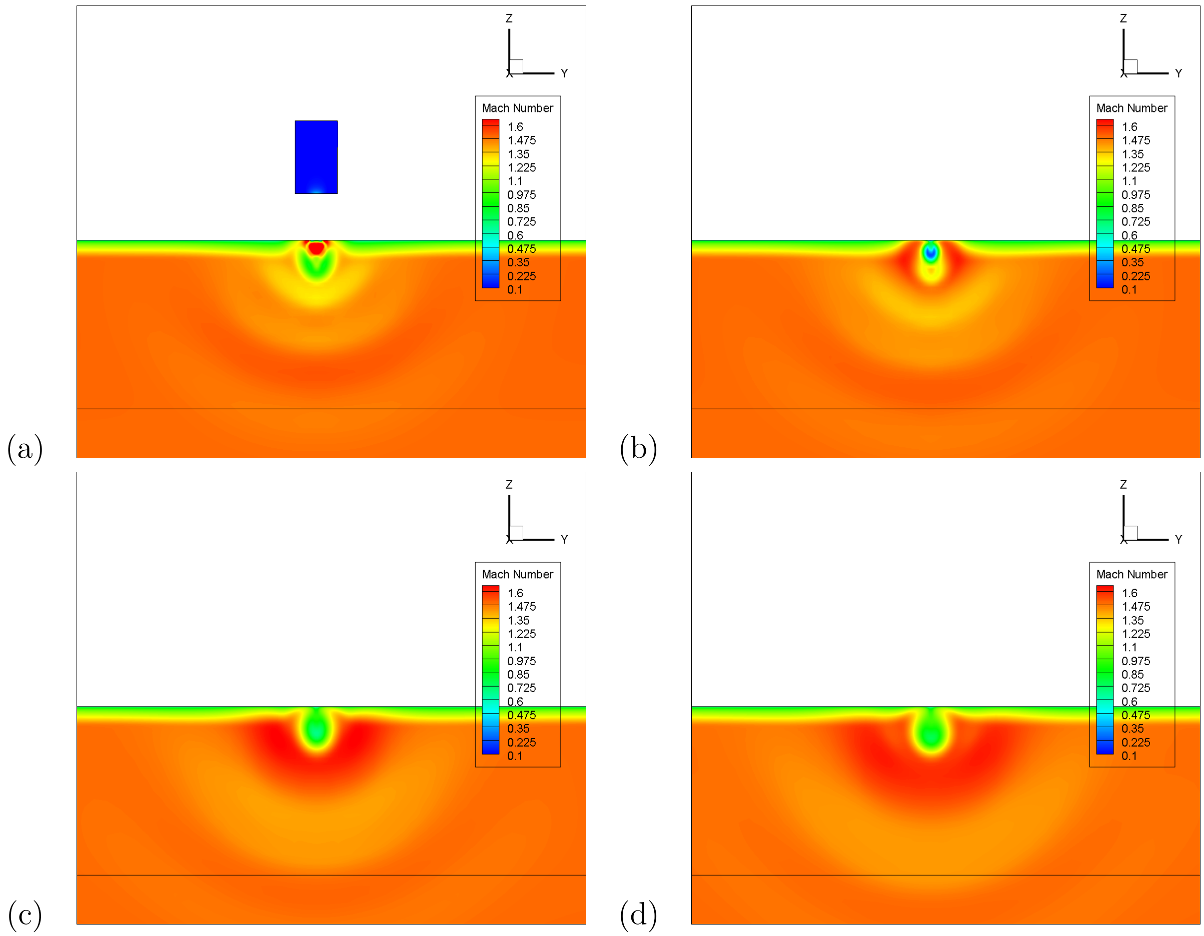

Figure 3.7. Downstream evolution of Mach number of three injectors into a supersonic boundary layer M = 1.5, TTR = 1.45, and all IPR = 2.7: (a) $0D_{inj}$, (b) $1D_{inj}$, (c) $3D_{inj}$, (d) Nozzle Exit

Inside the fluidic insert are a pair of counter-rotating vortices, which can be seen in Figure 3.8. The streamwise vortices form instantaneously due to the fluid-fluid interaction of the injected flow and freestream. These vortices form two vortex tubes that travel downstream. The vortex tubes fill the fluidic insert and give a shape to the insert.

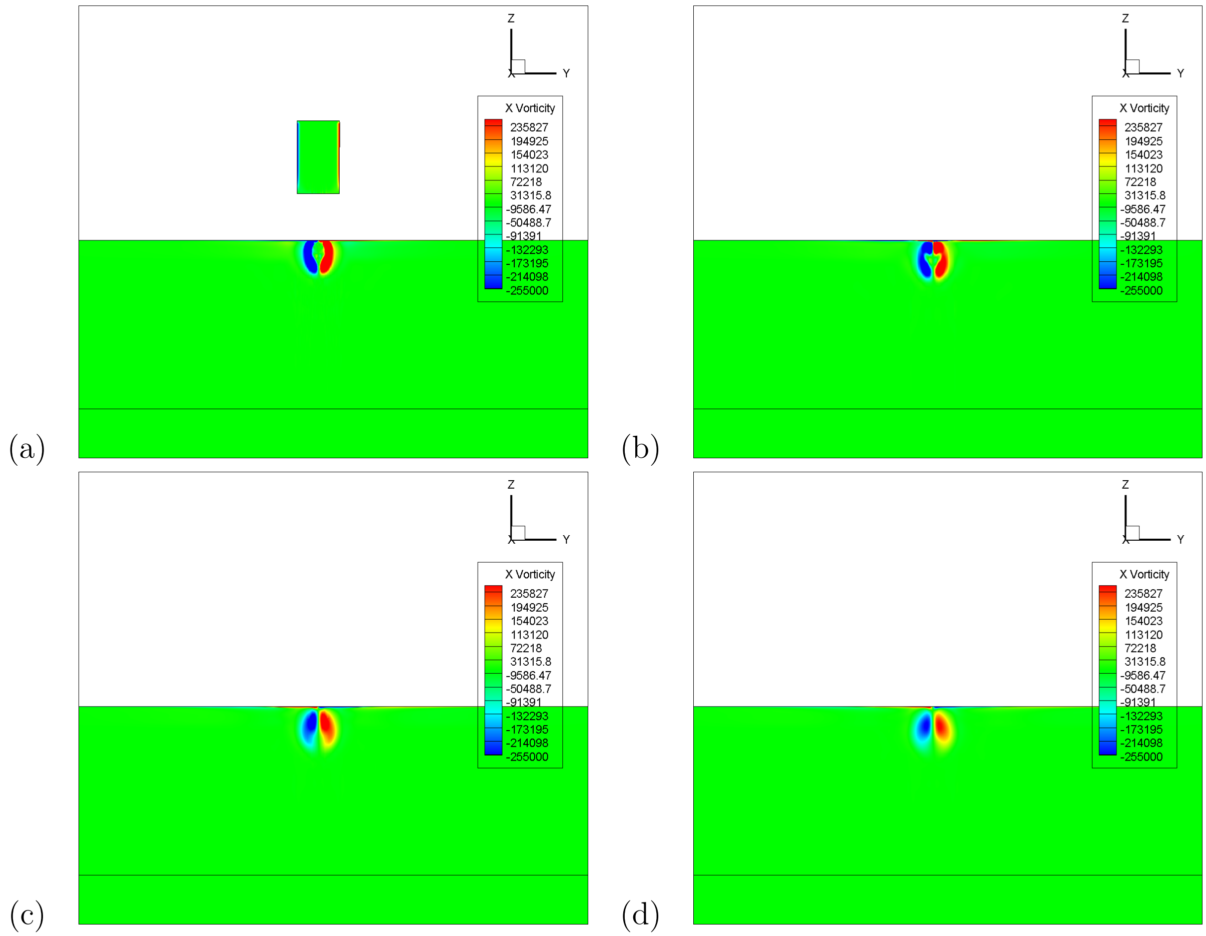

Figure 3.8. Downstream evolution of Mach number of three injectors into a supersonic boundary layer M = 1.5, TTR = 1.45, and all IPR = 2.7: (a) $0D_{inj}$, (b) $1D_{inj}$, (c) $3D_{inj}$, (d) Nozzle Exit

Spanwise slices have been taken parallel to the flat plate to gain an understanding of the vertical evolution of the fluidic insert. The slices are taken at $0.1D_{inj}$, $0.5D_{inj}$, and $1D_{inj}$ away from the flat plate. The shape as defined by the total pressure can be seen in Figure 3.9. Close to the flat plate, Figure 3.9(a), the fluidic insert increases in width at each injector and decreases in width between the injectors. The further away from the wall, the less of an effect the upstream and middle injector have on the shape. The width of the fluidic insert is smoother and there is a gradual increase in width to the downstream injector. The separation behind the downstream injector is also apparent in Figure 3.9(b). The fluidic insert width behind the downstream injector shrinks as the insert moves away from the flat plate. This is further confirmed by the fact that the width increases behind the injector further away from the flat plate, Figure 3.9(c).

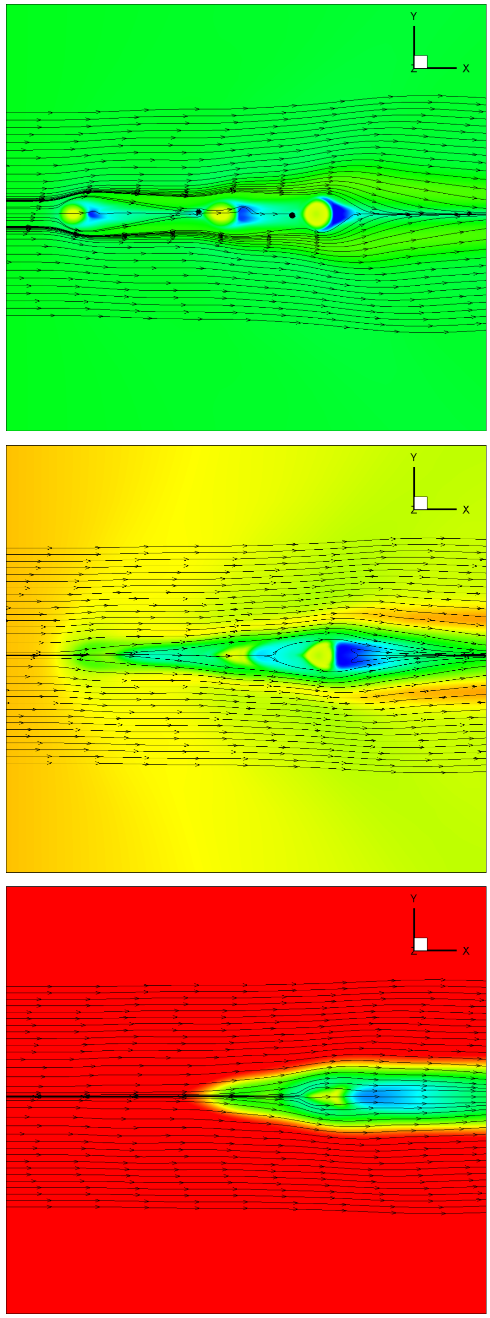

(a) (b) (c)

Figure 3.9. Vertical Evolution of Total Pressure with streamlines of three injectors into a supersonic boundary layer M = 1.5, TTR = 1.45, and all IPR = 2.7: (a) $0.1D_{inj}$, (b) $0.5D_{inj}$, and (c) $1D_{inj}$

3.1.2 Supersonic Boundary Layer Injector Angle Study

A description of all the operating conditions for the simulations that have been run involving the supersonic boundary layer is given in Table 2.5.1. These simulations compare the effect the angle of the downstream injector had on the fluidic insert. The motivation of this study was a possible limitation of the downstream injector angle due to physical restrictions. In a real world scenario, the shroud of the nozzle would not be as large as it was in the laboratory experiments. A 90° injector would most likely not have enough space for a feed tube to be attached in a way that would not impede the flow with the current design.

The shape of the fluidic insert can be visualized by the total pressure as shown in Figure 3.10. At first glance, the penetration of the injectors into the freestream seems to be identical. However by exporting and plotting a single streamline generated at the same point for each case, minor differences can be identified, as seen in Figure 3.11. The dotted black line is a streamline from the two injector configuration seen in Figure 3.4(b) as a comparison to past simulations and experiments. The furthest penetrating three injector condition is the 90° injector without a bend, followed by the 75° injector, then the 90° injector with a bend, and the least penetrating is the 60° injector. The 90° injector without a bend also has as much penetration as the two injector configuration even though there is a sizable difference in IPR as discussed in the previous section. The region of separation also increases as the injector angle is increased. This would cause the fluidic insert to lift off the wall more quickly. Figure 3.11 also shows how the three injector system has a smoother and more gradual shape. The upstream injector in both systems penetrates approximately the same distance. The middle injector then smooths the region between the upstream and downstream injectors so there is not as sharp of an increase in depth. The middle injector lowers the momentum even further, which allows the downstream injector to operate at a lower IPR and still achieve the same penetration.

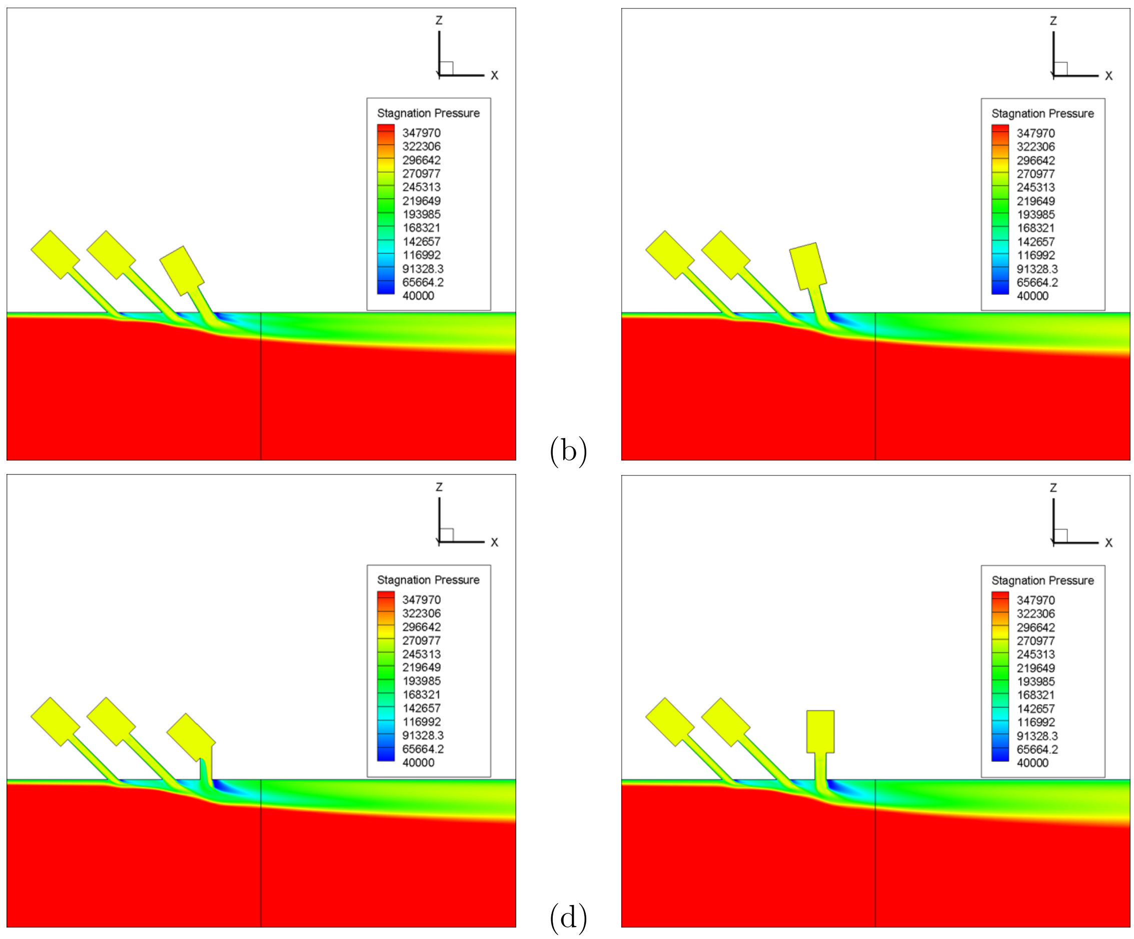

(a) (b) (c) (d)

Figure 3.10. Streamwise Total Pressure contours of three injectors into a supersonic boundary layer M = 1.5, TTR = 1.45, and all IPR = 2.7: Downstream injector angle (a) 60°, (b) 75°, (c) 90° with a bend, (d) 90° without a bend

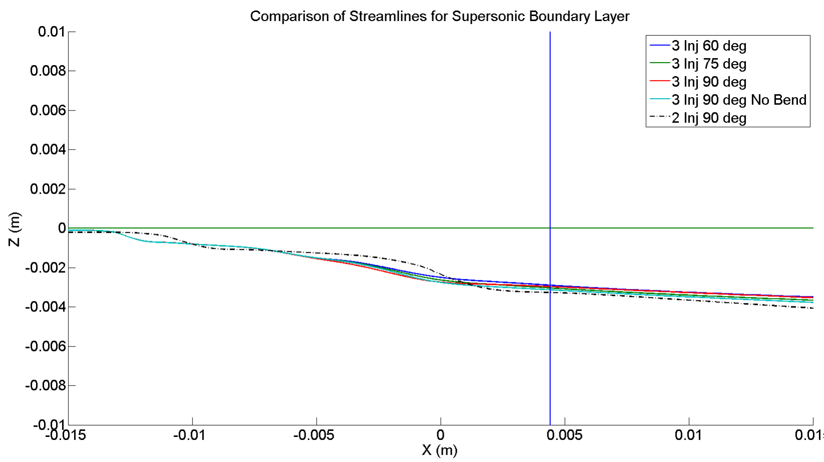

(a)

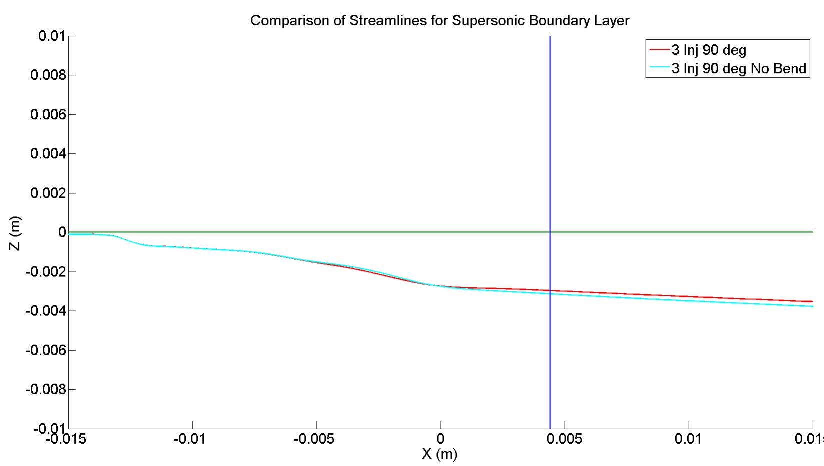

(b)

Figure 3.11. Injector penetration distance comparison by exported streamlines for (a) all conditions and (b) direct comparison between 90° with and without feed tube bend

The effect of the downstream injector angle on Mach number can be seen in Figure 3.12. As the angle is increased, the strength of the downstream bow shock increases. The orange-yellow region becomes larger. This region also merges with the bow shock from the middle injector more and more as the angle is increased. The expansions that occur behind each downstream injector is largest in the 60° injector and become smaller as the injector angle is increased with the smallest area being from the 90° injector with a bend. The separation behind the downstream injector is similar between Figures 3.12(b),(c), and (d). They each extend about the same distance as well as have equal strength. The separation behind the 60° injector is much smaller than the other three configurations. The same can be said about the area of recirculation between the middle and downstream injectors.

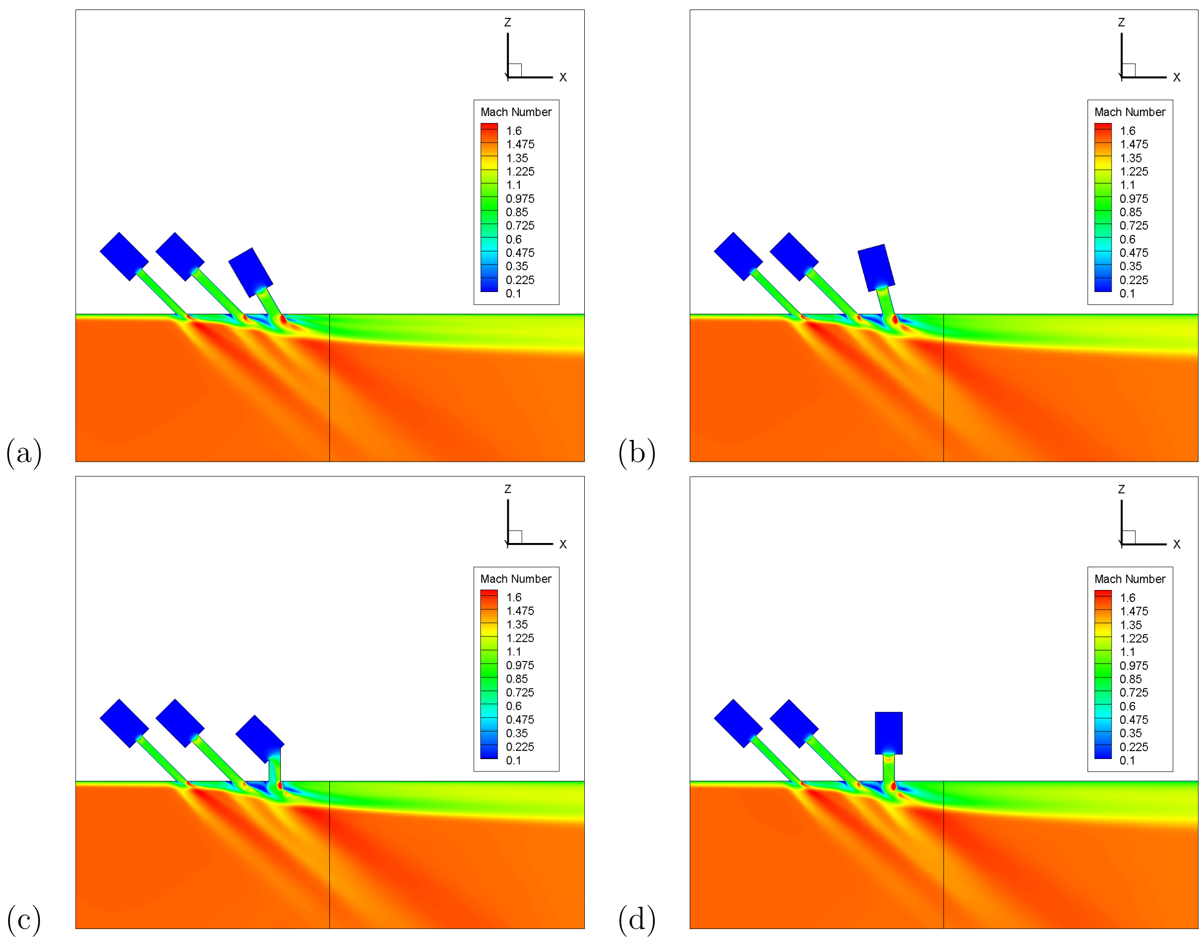

Figure 3.12. Streamwise Mach number contours of three injectors into a supersonic boundary layer M = 1.5, TTR = 1.45, and all IPR = 2.7: Downstream injector angle (a) 60°, (b) 75°, (c) 90° with a bend, (d) 90° without a bend

Decreasing the amount of turbulent kinetic energy (TKE) in a supersonic jet could reduce the amount of noise by reducing the radiated efficiency. Papamoschou et al. [19] determined that there is a 3 dB noise reduction by halving the volume of high TKE within the jet. The TKE of the supersonic boundary layer is shown in Figure 3.13. There are no interactions with exterior flow in these simulations as there is in the nozzle flow, however, the initial strength of the TKE and length of the highe TKE region can be seen. The primary source of TKE is from the downstream injector. This injector creates more cross flow than the other two,and this generates a high amount of mixing. As the downstream injector angle is increased the area of high TKE behind the downstream injector increases.

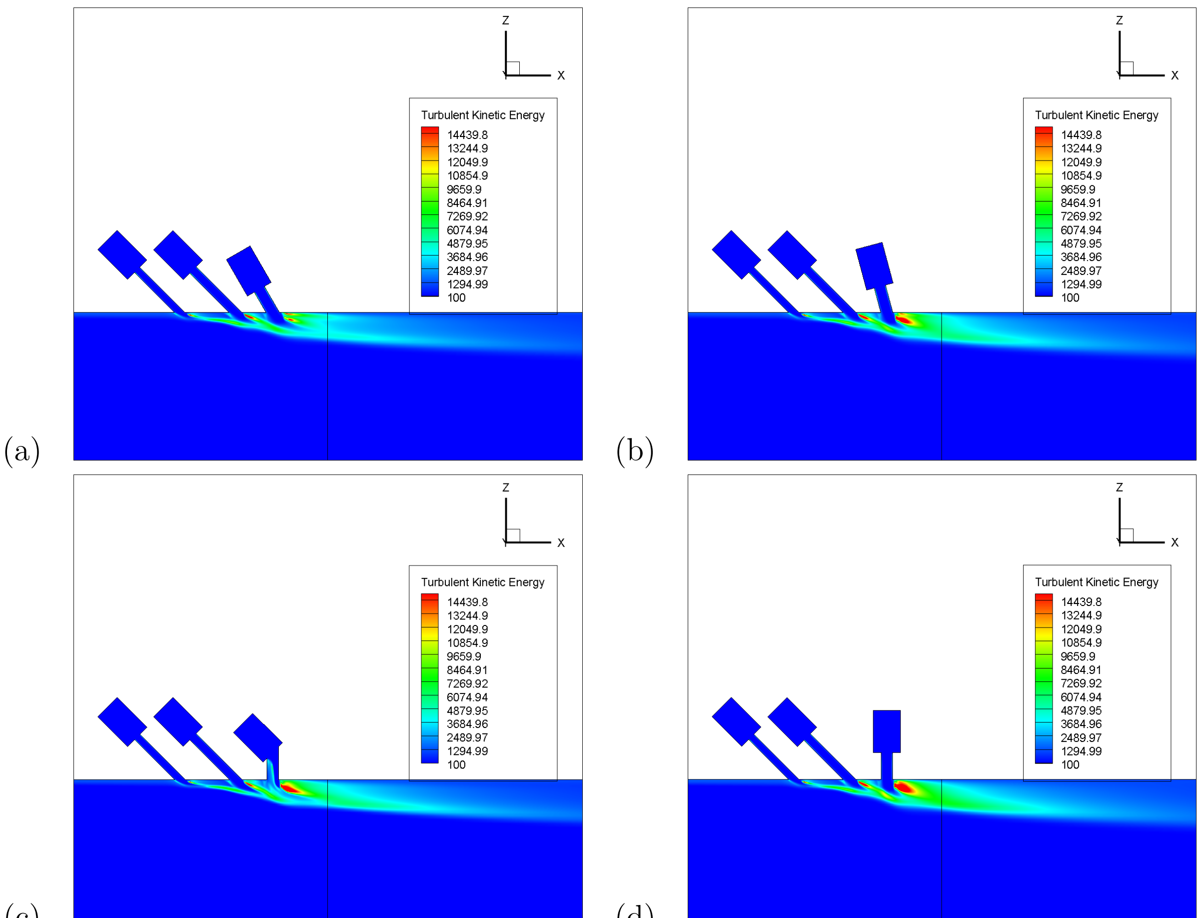

Figure 3.13. Streamwise Turbulent Kinetic Energy contours of three injectors into a supersonic boundary layer M = 1.5, TTR = 1.45, and all IPR = 2.7: Downstream injector angle (a) 60°, (b) 75°, (c) 90° with a bend, (d) 90° without a bend

When comparing the different configurations in the wall normal direction only the slice corresponding to the equivalent nozzle exit is shown. The flow conditions and the effective area at the nozzle exit could correlated with observed noise reduction. The flow further downstream is not studied as it does not provide any correspondence to the military style nozzle. The lack of a wall bounded flow in the nozzle case generates a significantly different result.

The results are not perfectly symmetrical however, which is not expected. However, the meshes used to generate the results are symmetric. The asymmetry is most likely a result of the numerics of the flow solver or how the solver sweeps across the cells. [20] Supersonic flow is difficult to predict even when using steady RANS equations and the additional cross flow from the injectors further increases the difficulty. The simulations that were run however did reach a residual with a root mean square (rms) of 10^{-7} which is usually adequate for convergence.

The shape of the fluidic insert can be described using the total pressure and total temperature as presented in Figure 3.14 and Figure 3.15 respectively. The flow has a bulbous shape for all the different injector configurations. The only slight difference is in the case of the 90° injector with a bend. In this case the shape is more circular than the other configurations. The biggest difference between the four cases is the distance that the fluidic insert separates from the wall, which can be better seen in the total temperature in Figure 3.15. The two lowest injector angle configurations are more attached to the wall, with the 60° injector being attached more than the 75° injector. The two 90° configurations have lifted completely off the wall. The 90° without a bend has separated the furthest out of all configurations. The penetrations from all injectors are also still far away from the equivalent jet centerline.

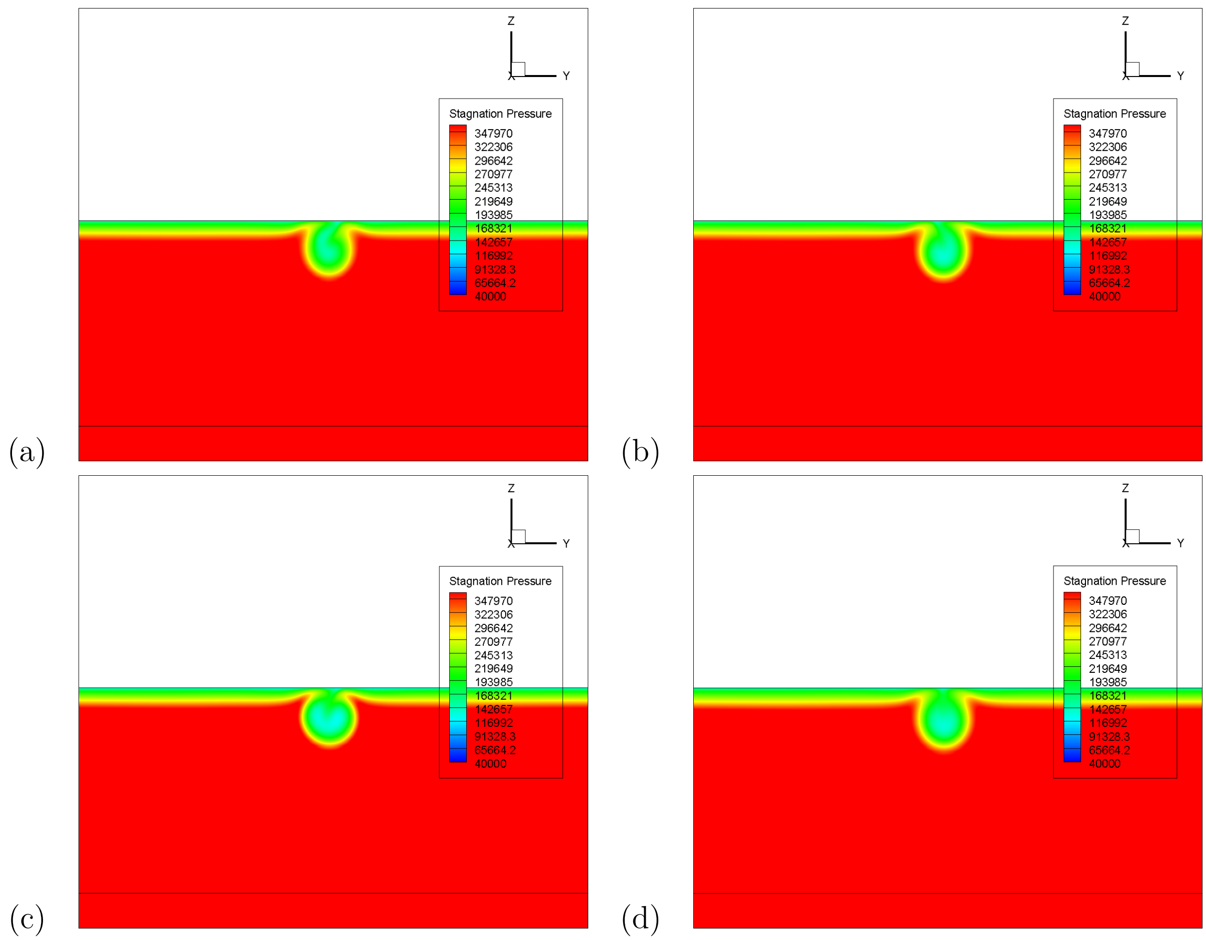

Figure 3.14. Wall normal slice with total pressure contours at the equivalent nozzle exit of three injectors into a supersonic boundary layer M = 1.5, TTR = 1.45, and all IPR = 2.7: Downstream injector angle (a) 60°, (b) 75°, (c) 90° with a bend, (d) 90° without a bend

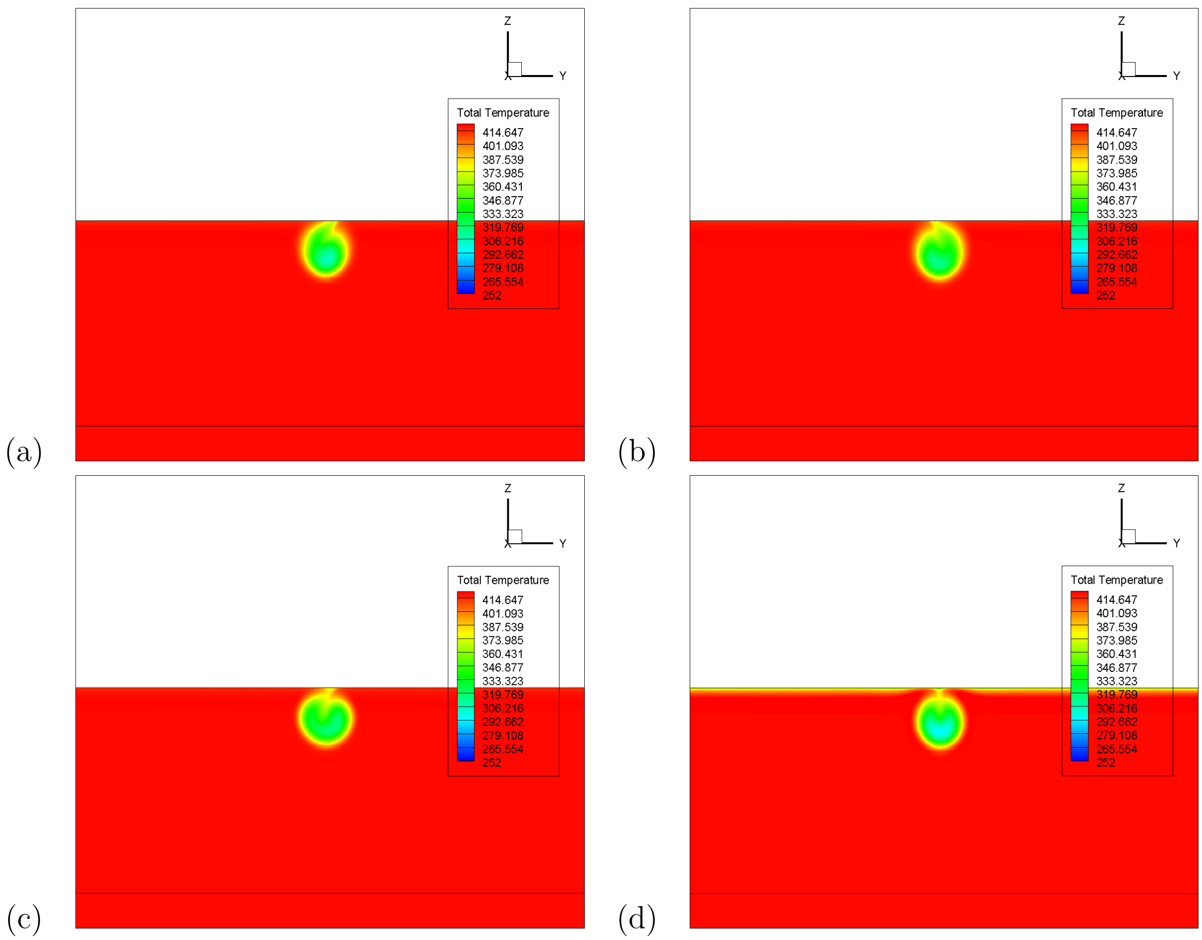

Figure 3.15. Wall normal slice with total temperature contours at the equivalent nozzle exit of three injectors into a supersonic boundary layer M = 1.5, TTR = 1.45, and all IPR = 2.7: Downstream injector angle (a) 60°, (b) 75°, (c) 90° with a bend, (d) 90° without a bend

The Mach number gives insight of the speed of the flow as well as the strength of the generated bow shocks. The contours of Mach number can be seen in Figure 3.16. Between the merged bow shocks, as seen in Figure 3.12, and the fluidic insert the flow is exceeding the freestream Mach number of 1.5. This region also has a slightly higher Mach number in the two 90° cases, as it is a slightly darker red. The strength of the merged bow shocks also grow as the downstream injector angle is increased. The bow shocks have a lighter orange color the steeper the angle, indicating a lower Mach number. Another important characteristic to note is that in all cases the bow shocks extend past the equivalent nozzle exit, which could cause the shocks to interact in the military style nozzle.

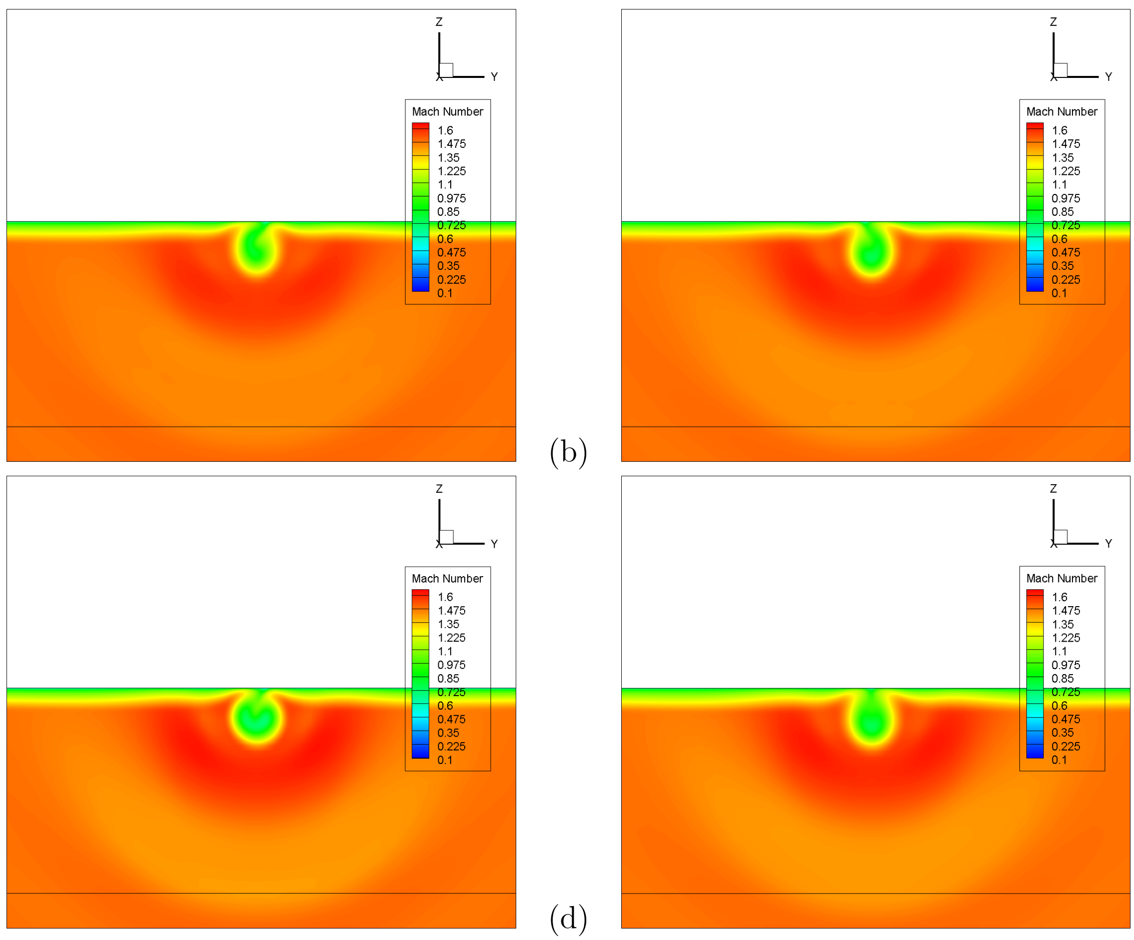

(a) (b) (c) (d)

Figure 3.16. Wall normal slice with Mach number contours at the equivalent nozzle exit of three injectors into a supersonic boundary layer M = 1.5, TTR = 1.45, and all IPR = 2.7: Downstream injector angle (a) 60°, (b) 75°, (c) 90° with a bend, (d) 90° without a bend

The high amplitude vortices described in the previous section can also be seen in Figure 3.17. The asymmetry seen in the shape of the fluidic insert can be attributed to the asymmetry of the streamwise vorticity. However, the three injector configurations without a bend have an elongated oval when compared to the more circular vorticies of the 90° without bend, Figure 3.17(c). The strengths of the vortices are slightly higher in the two 90° configurations as there are more darker reds and blues when compared to the other configurations.

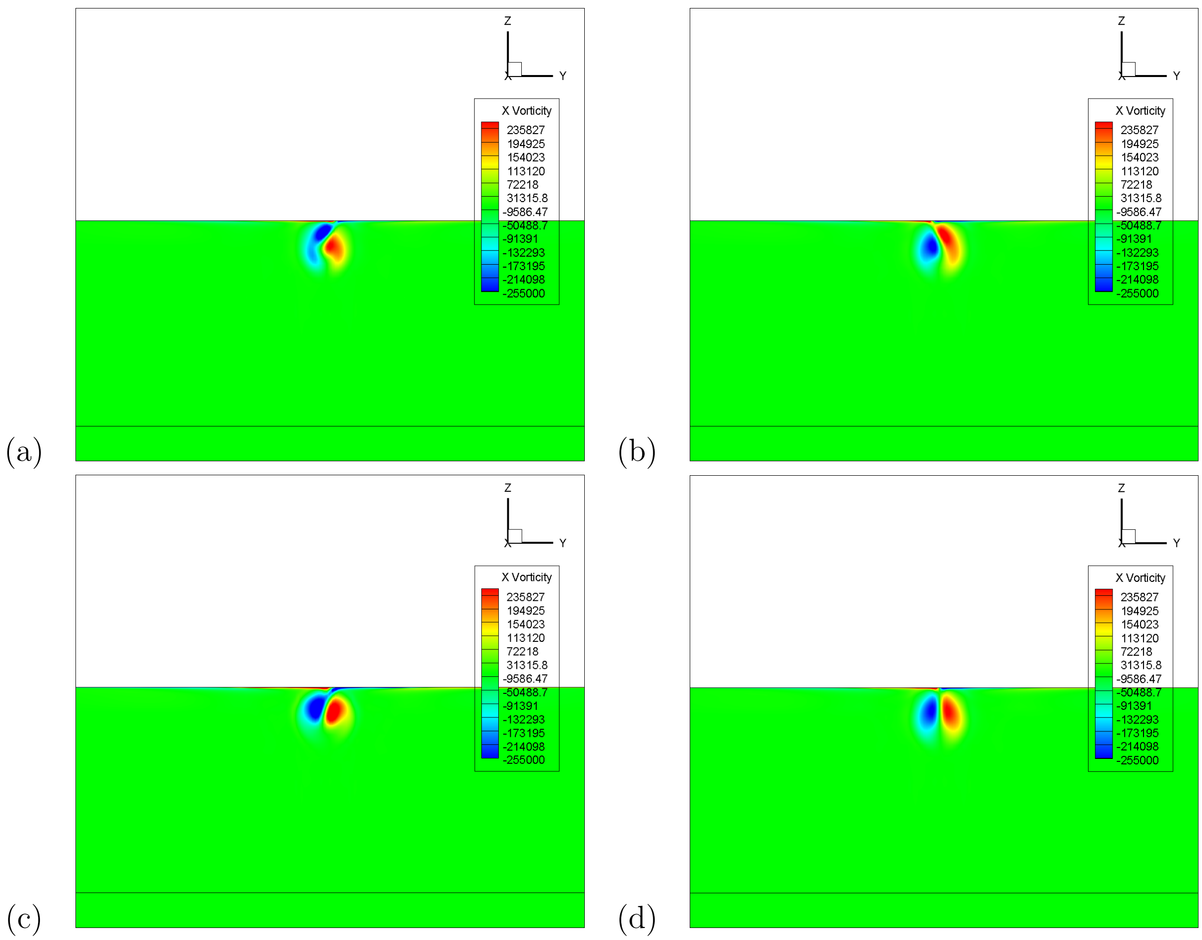

Figure 3.17. Spwanwise slice with streamwise vorticity contours at the equivalent nozzle exit of three injectors into a supersonic boundary layer M = 1.5, TTR = 1.45, and all IPR = 2.7: Downstream injector angle (a) 60°, (b) 75°, (c) 90° with a bend, (d) 90° without a bend

The effect of the vortices can be seen in the turbulent kinetic energy. This is shown in Figure 3.18. The bulbous high TKE region is separated from the wall in all configurations. The TKE has the lowest magnitude for the smaller injector angles and increases as the angle is increased. The TKE was similar in the streamwise direction as seen in Figure 3.13. However, the TKE did not spread downstream as far when the injector angle was smaller, which is why the magnitude is greater in the 90° configurations in Figure 3.18.

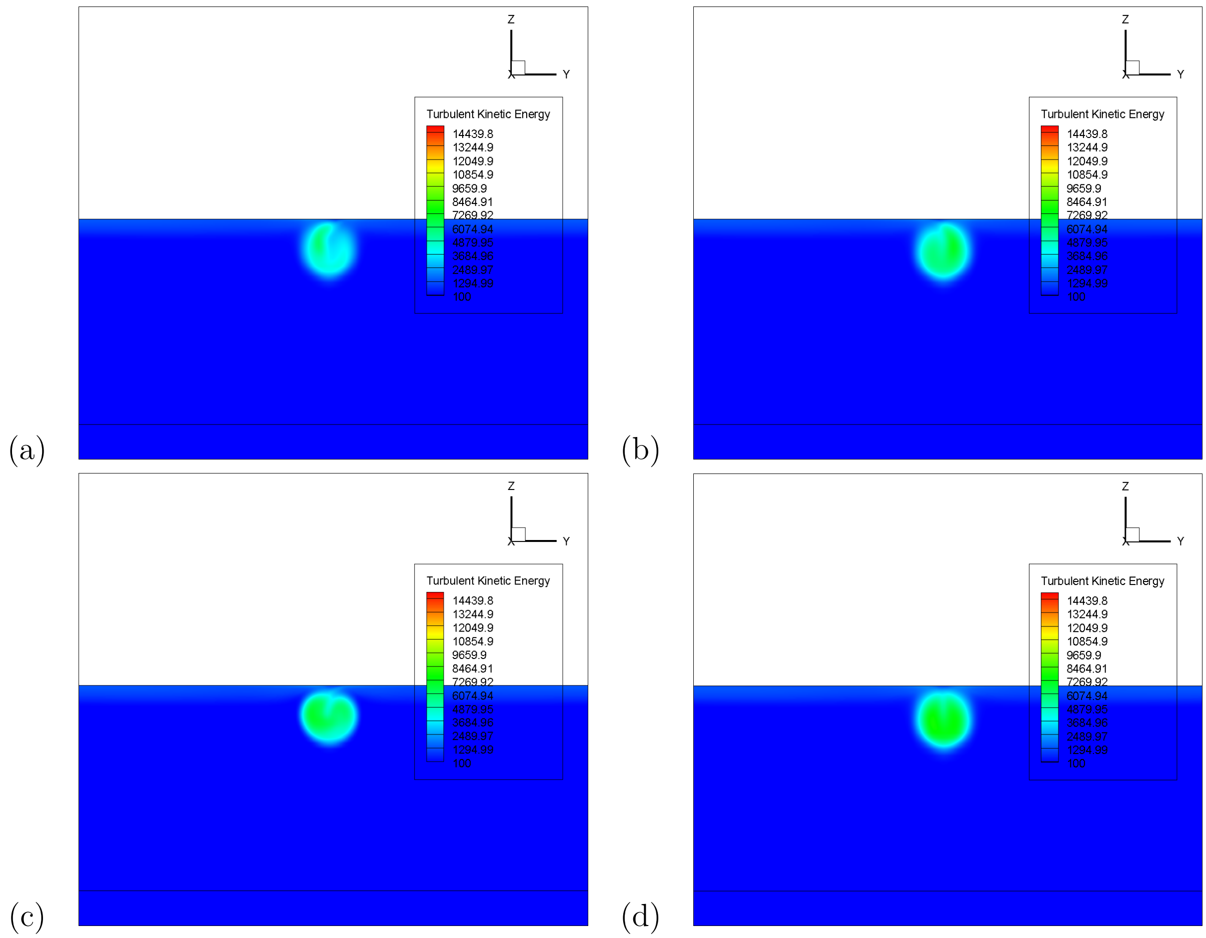

Figure 3.18. Spwanwise slice with turbulent kinetic energy contours at the equivalent nozzle exit of three injectors into a supersonic boundary layer M = 1.5, TTR = 1.45, and all IPR = 2.7: Downstream injector angle (a) 60°, (b) 75°, (c) 90° with a bend, (d) 90° without a bend

3.2 High-Speed Military Nozzle with Fluidic Inserts

In this section four different nozzle configurations are described. The different configurations can be seen in Table 3.2. The main differences between the different nozzle configurations are the number of injectors per fluidic insert, the injector locations, the injector area ratios, and the diameter of the nozzle exit, D_{exit}. Each configuration uses three fluidic inserts with a total of six or nine total injectors. All downstream injectors are located at 70% of the diverging section. In the case of there being only two injectors per insert the upstream is located at 30% of the diverging section, and if there is a third injector the upstream is located at 20%. The middle injector is located at 50% of the diverging section. The two injector configurations have an injector area ratio of 1:1, whereas the three injector configurations have an area ratio of 1:2:4. The Gen 1B, Gen 2, and GE Test Scale have D_{exit} of 0.885, 1.06, and 5.07 inches respectively. All of the different configurations were simulated using ANSYS-CFX.

Military Style Nozzle Configurations					
Family	# of Inj	Inj Location	Inj Area Ratio	D_{inj}	Nozzle D_{exit}
Gen 1B	2	30%, 70%	1:1	0.053 in	0.885 in
Gen 1B	3	20%, 50%, 70%	1:2:4	0.053 in	0.885 in
Gen 2	3	20%, 50%, 70%	1:2:4	0.0635 in	1.06 in
GE Test Scale	2	30%, 70%	1:1	0.303 in	5.07 in

Table 3.1. Military Style Nozzle Configurations

The differences between a two injector and three injector per fluidic insert nozzle were observed. The purpose of this discussion is to see if more smaller injectors accomplishes the same results of two larger injectors. In a real world setting, having injector holes could cause the nozzle to erode more quickly, especially with large holes inside the nozzle.

The different nozzle configurations are all modeled after the same nozzle. To achieve a different nozzle exit diameter, the whole nozzle was scaled by the same factor. By holding all other components constant, a Reynolds number study can be conducted. Similar nozzle configurations were compared and analyzed.

A correlation between noise reduction and flow parameters was also attempted to be found. Various parameters that are known to give insight into noise reduction have been analyzed. They have been compared to experimental data where the observed noise reduction is known.

3.2.1 Comparison between Two and Three Injector Fluidic Inserts

The two nozzle configurations that will be used to show the difference between two and three injector fluidic inserts are the two Gen 1B nozzles. The differences between the two nozzles are the locations of the injectors, the area ratio of the injectors, and the IPR of the injectors. The specific physical differences can be seen in Table 3.2. The nozzle pressure ratio for the simulations was 3.0, which corresponds to a jet Mach number of 1.36. The total temperature ratio was 3.0 and the ambient temperature and pressure was 288K and 101,008 Pa respectively.

The first comparisons were done between a two injector with $IPR_1 = 2.7$ and $IPR_2 = 4.5$ and for the three injector configuration each IPR was set to 2.7. This gives comparable results but the injector mass flow rates between the two configurations are not equal, which can be seen in Table 3.2. To achieve the same injector mass flow rates, the ratio of mass flow rates were calculated and then multiplied by the IPR of three injector configuration to get a new IPR. The result was an IPR of 3.6. When comparing the new simulation to the two injector simulation the mass flow rates were almost exact, which can be seen in Table 3.3. The IPR = 3.6 case was then used to make comparisons between the two configurations.

Mass Flow Rate Comparison				
Configuration	Three Inj	IPR	Two Injector	IPR
Inj_1 Mass Flow Rate	0.000926 kg/s	2.7	0.00229 kg/s	2.7
Inj_2 Mass Flow Rate	0.001398 kg/s	2.7	0.00378 kg/s	4.5
Inj_3 Mass Flow Rate	0.002312 kg/s	2.7	-	-
Total Mass Flow Rate	0.004636 kg/s		0.00607 kg/s	

Table 3.2. Mass Flow Rate Comparison between three injector fluidic insert IPR =2.7 and two injector fluidic insert $IPR_1 = 2.7$ $IPR_2 = 4.5$

Mass Flow Rate Comparison				
Configuration	Three Inj	IPR	Two Injector	IPR
Inj_1 Mass Flow Rate	0.001241 kg/s	3.6	0.00229 kg/s	2.7
Inj_2 Mass Flow Rate	0.001863 kg/s	3.6	0.00378 kg/s	4.5
Inj_3 Mass Flow Rate	0.003085 kg/s	3.6	-	-
Total Mass Flow Rate	0.006189 kg/s		0.00607 kg/s	

Table 3.3. Mass Flow Rate Comparison between three injector fluidic insert IPR =3.6 and two injector fluidic insert $IPR_1 = 2.7$ $IPR_2 = 4.5$

3.2.1.1 Streamwise Comparison of Military Nozzle

A basic understanding of the flow field generated by a three injector and a two injector per fluidic insert nozzle can be gained by taking a slice through the center of the nozzle and injectors. Mach number contours are shown in Figure 3.19. The flow in the nozzle is where there are the most differences. There are three bow shocks in the three injector configuration, Figure 3.19(a), and only two in the two injector configuration, Figure 3.19(b). The bow shocks from the middle and downstream injector in the three configuration merge into one shock as seen in the supersonic boundary layer study. The upstream bow shock in the three injector configuration is also smaller and does not penetrate as far as the upstream bow shock in the two injector configuration. This is because the injector diameter is significantly smaller than the two injector configuration. The shock cell structure is very similar between the two configurations. A slip line can be seen along the centerline in both configurations. The Mach disk is present in both but is reduced outside of the nozzle exit.

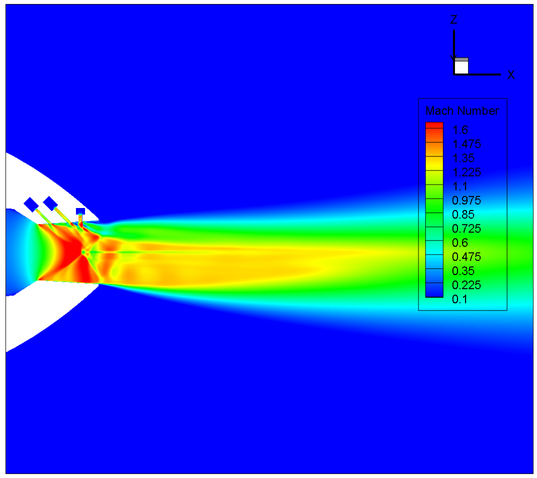

(a)

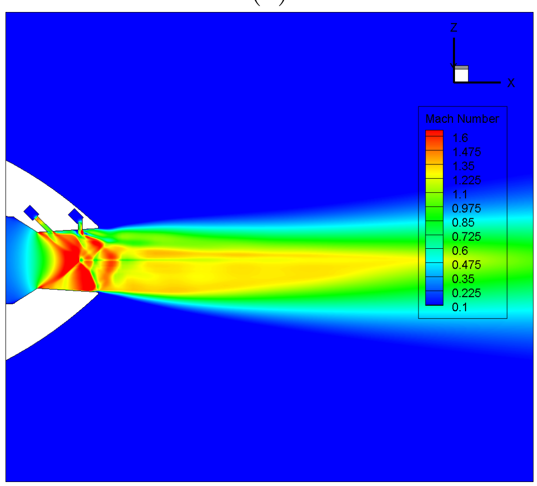

(b)

Figure 3.19. Comparison of streamwise slice with Mach number contours for two configurations of a military style nozzle NPR =3.0, M_j = 1.36, TTR = 3.0: (a) 3 Injectors per fluidic insert all IPR = 3.6, (b) 2 Injector per fluid insert IPR_1 = 2.7, IPR_2 = 4.5

The total pressure and total temperature are still the best parameters to visualize the fluidic insert and can be seen in Figure 3.20 and Figure 3.21. The total pressure gives some more insight than the total temperature however. The first notable difference inside of the nozzle is that the fluidic insert has a smoother gradual slope in the three injector configuration. This is the same behavior shown in the supersonic boundary layer study. The flow also separates more behind the downstream injector in the three injector configuration than the two injector configuration. Also at the nozzle exit the penetration of the fluidic insert is slighty farther in the three injector configuration. Outside of the nozzle the two injector configuration has a stronger shock cell structures than the three injector configuration. This is evident by the more severe total pressure drop as there is more yellow than red region. This is due to the fluidic insert penetrating further in the three injector case. The shock cell structure of the baseline nozzle as seen in Figure 1.2 is contained by the top and bottom shear layers. The addition of the fluidic inserts creates a weaker shock cell structure by breaking the plume into separate sections. The flow properties of the areas of the jet plume containing the fluidic inserts are vastly different than core flow. This makes the angle of the shock waves and strength remarkably weaker in theses areas. The jet plume also is shorter in the three injector configuration due to the further penetration.

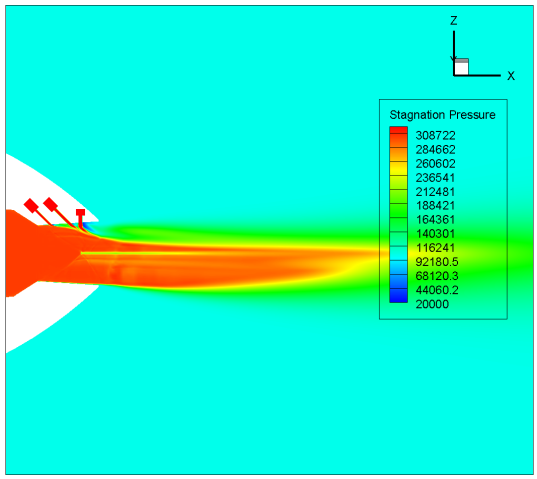

(a)

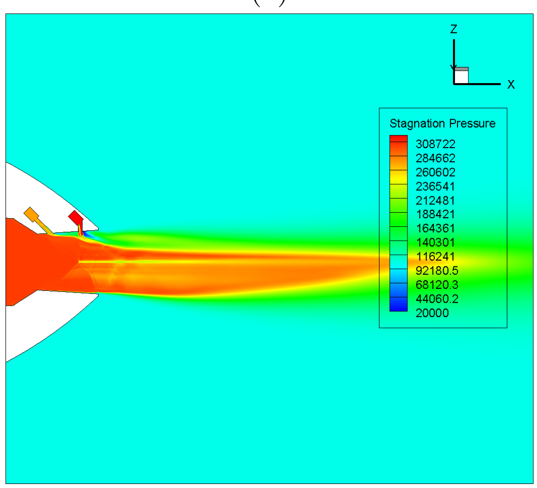

(b)

Figure 3.20. Comparison of streamwise slice with total pressure contours for two configurations of a military style nozzle NPR =3.0, M_j = 1.36, TTR = 3.0: (a) 3 Injectors per fluidic insert all IPR = 3.6, (b) 2 Injector per fluid insert IPR_1 = 2.7, IPR_2 = 4.5

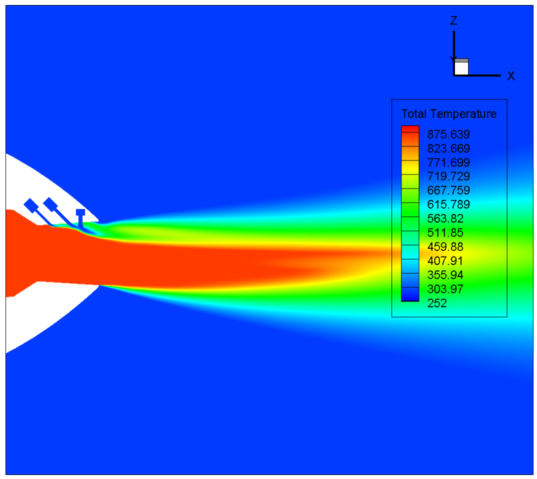

(a)

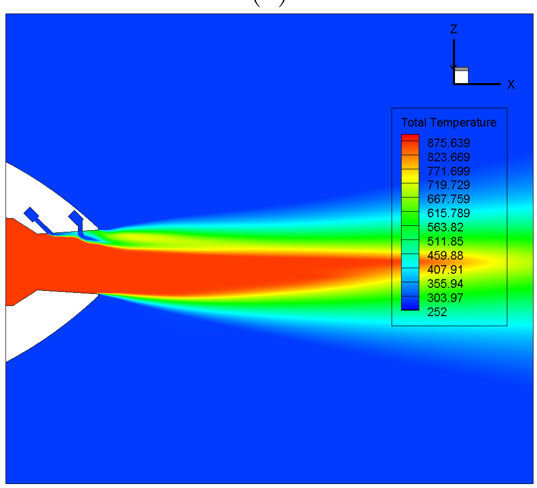

(b)

Figure 3.21. Comparison of streamwise slice with total temperature contours for two configurations of a military style nozzle NPR =3.0, M_j = 1.36, TTR = 3.0: (a) 3 Injectors per fluidic insert all IPR = 3.6, (b) 2 Injector per fluid insert IPR_1 = 2.7, IPR_2 = 4.5

The turbulent kinetic energy of the two configurations is presented in Figure 3.22. There are only a few key differences between the two configurations. Inside of the nozzle there is less areas of high TKE between the upstream and downstream injectors in the three injector configuration. This is due to the addition of the middle injector giving the flow inside the insert more stability and strength in this region. There is more TKE behind the downstream injector in the three injector configuration when comparing it to the two injector. This high TKE also extends further down stream in the three injector configuration than the two injector configuration. This is due to there being more cross stream flow from the downstream injector in the three injector configuaration. There is more cross stream flow because the middle injector creates more of a streamwise momentum loss than the two injector configuration. Other than this further extension of high TKE from the nozzle exit, there is little difference outside of the nozzle.

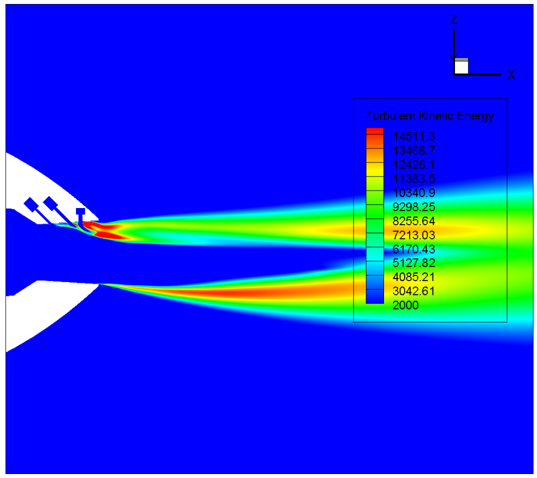

(a)

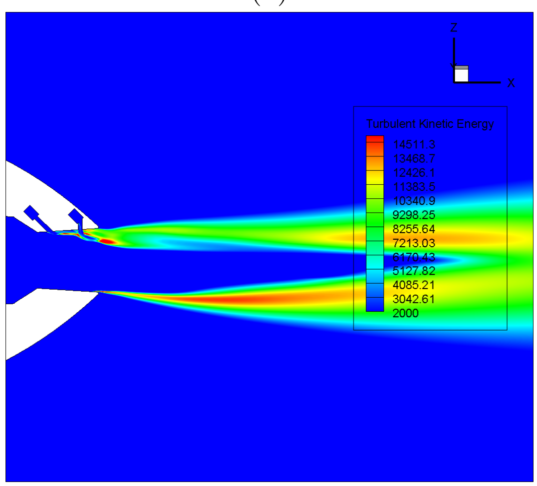

(b)

Figure 3.22. Comparison of streamwise slice with turbulent kinetic energy contours for two configurations of a military style nozzle NPR =3.0, $M_j = 1.36$, $TTR = 3.0$: (a) 3 Injectors per fluidic insert all $IPR = 3.6$, (b) 2 Injector per fluid insert $IPR_1 = 2.7$, $IPR_2 = 4.5$

3.2.1.2 Downstream Evolution Comparison of Military Nozzle

To further understand the shape of the fluidic inserts axial slices were compared at the nozzle exit, $0.5D_{Nozzle}$, and $2D_{Nozzle}$ for the two configurations. The total pressure contours can be seen in Figure 3.23 and the total temperature can be seen in Figure 3.24. The shape of the corrugations are similar to what was seen in the injectors into a supersonic boundary layer. There are subtle differences of the fluidic inserts when comparing the three and two injector configurations. At the nozzle exit, the three injector configuration has a more consistent total pressure than the two injector configuration. There are more yellow and orange regions of total pressure compared to the almost uniform red region of the three injector configuration. The same can be seen the further downstream the fluidic insert travels. The shape of the fluidic insert is similar between the two configuraitons as well. The only difference is the three injector configuration appears to be slightly larger in size. The size difference can especially be seen at the $2D_{Nozzle}$ location. The shape of the plume progressively changes into a triangular shape as the flow travels downstream. This was seen in the flow measurements of the two injector configuration performed by Powers. [8]

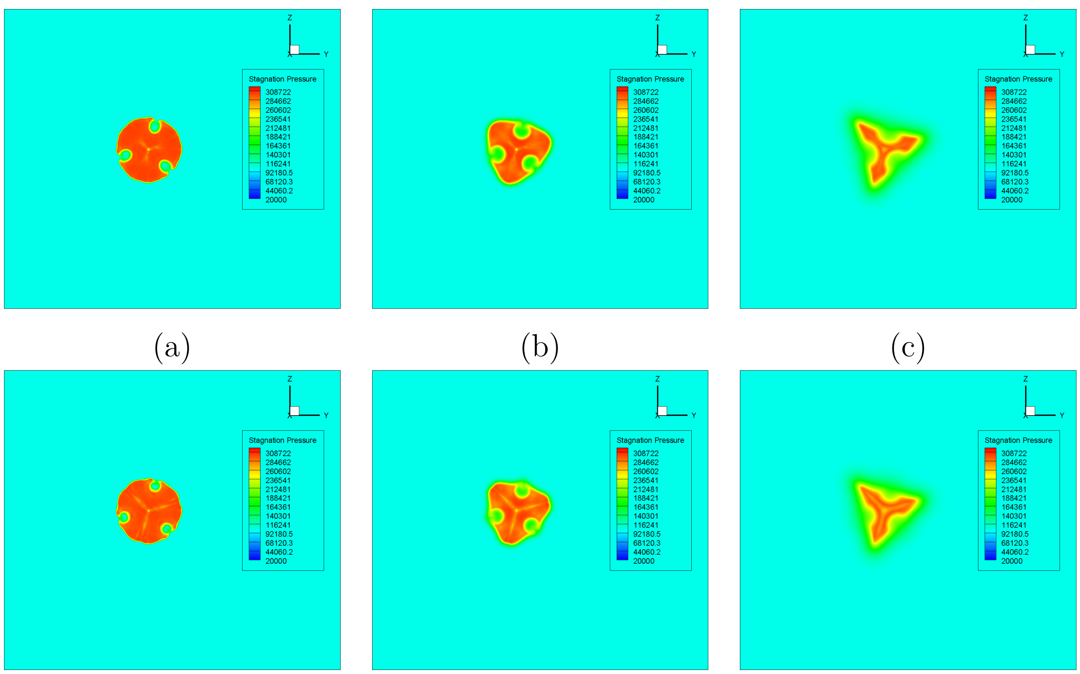

(a) (b) (c)

(d) (e) (f)

Figure 3.23. Comparison of downstream evolution of total pressure for two configurations of a military style nozzle NPR =3.0, M_j = 1.36, TTR = 3.0: 3 Injectors per fluidic insert all IPR = 3.6 (a) at nozzle exit, (b) at $0.5D_{Nozzle}$, and (c) at $2D_{Nozzle}$: Injector per fluid insert IPR_1 = 2.7, IPR_2 = 4.5 (d) at nozzle exit, (e) at $0.5D_{Nozzle}$, and (f) at $2D_{Nozzle}$

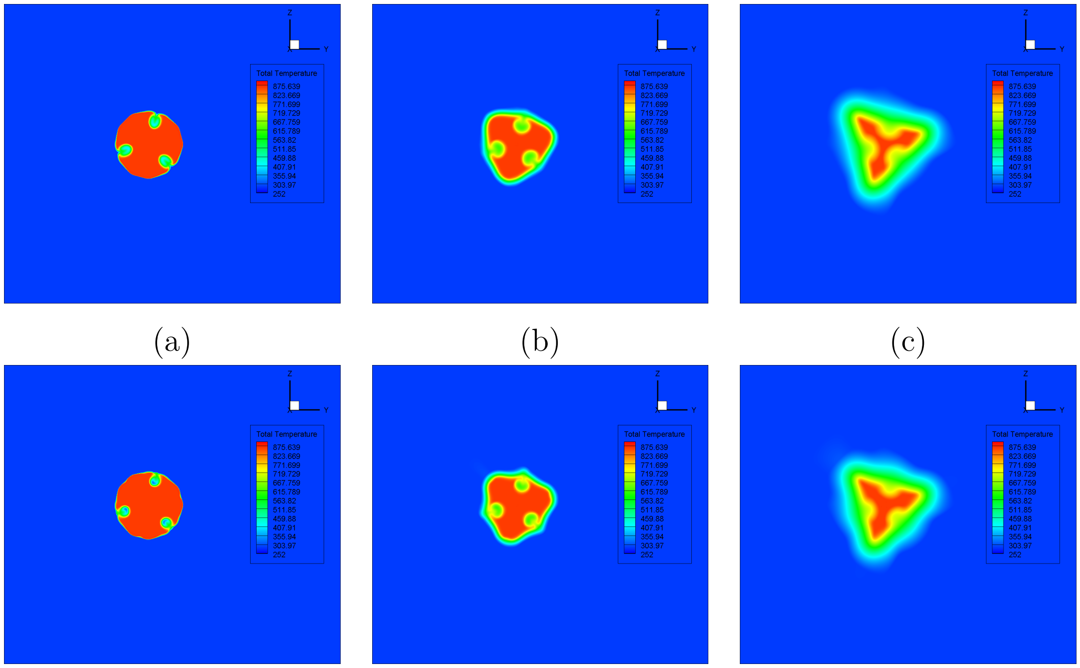

(a) (b) (c)

(d) (e) (f)

Figure 3.24. Comparison of downstream evolution of total temperature for two configurations of a military style nozzle NPR =3.0, M_j = 1.36, TTR = 3.0: 3 Injectors per fluidic insert all IPR = 3.6 (a) at nozzle exit, (b) at $0.5D_{Nozzle}$, and (c) at $2D_{Nozzle}$: Injector per fluid insert IPR_1 = 2.7, IPR_2 = 4.5 (d) at nozzle exit, (e) at $0.5D_{Nozzle}$, and (f) at $2D_{Nozzle}$

The downstream evolution of the Mach for both configurations can be seen in Figure 3.25. At the nozzle exit there is a pinwheel like shape. This region corresponds to the area of the flow that is operating at the intended jet Mach number of 1.36. In both configurations this region is surround by a dark red region, where the Mach number exceeds the jet Mach number. These regions are most likely due to the bow shocks that form off of the injectors. The pinwheel region is larger in the three injector configuration. This is due to the bow shocks from the middle and downstream injectors merging and forming a larger bow shock. Also in the two injector configuration, there are areas near the wall in between two fluidic inserts where the Mach number is approximately equal to one. This area does not appear in three injector configuration due to the bow shocks being stronger and larger. The bow shocks extend all the way to the nozzle wall. At $0.5D_{Nozzle}$ downstream the Mach number is 1.36 in the core of the jet plume. The areas where the fluidic inserts are present have a Mach number closer to one as seen in Figure 3.25(b) and (e). The lower Mach number area is also bigger in the three injector configuration suggesting the fluidic insert is larger, as seen with the total pressure and total temperature. Whenever the flow reaches $2D_{Nozzle}$ downstream, there are only minor differences as the flow has continued to spread and penetrate the jet plume. The three injector configuration has penetrated slightly further than the two injector configuration.

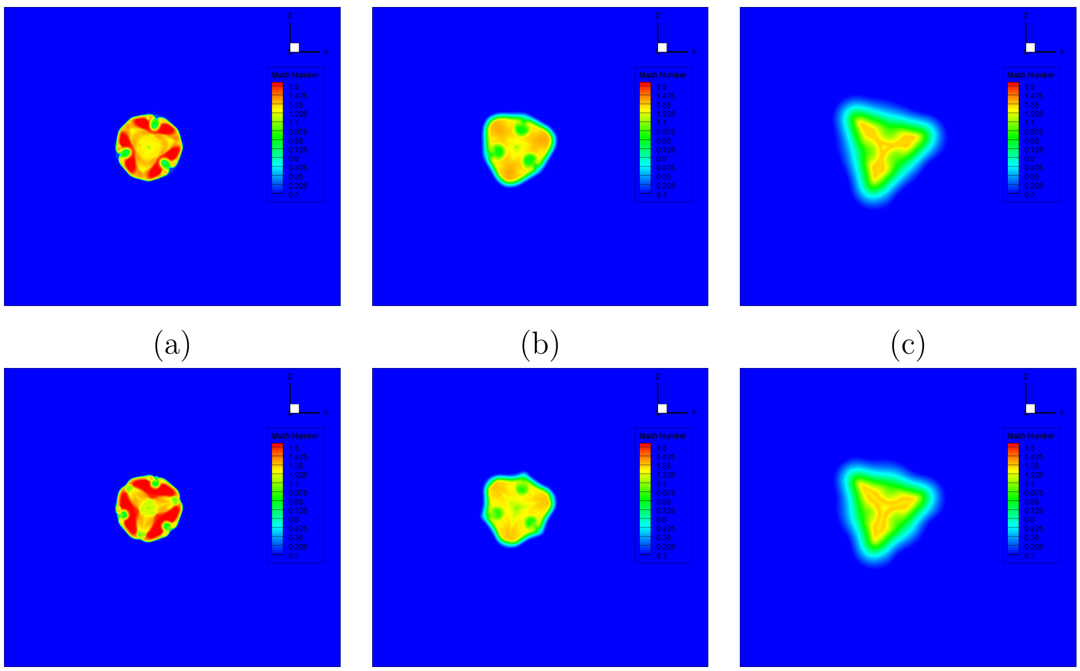

(a) (b) (c)

(d) (e) (f)

Figure 3.25. Comparison of downstream evolution of Mach number for two configurations of a military style nozzle NPR =3.0, M_j = 1.36, TTR = 3.0: 3 Injectors per fluidic insert all IPR = 3.6 (a) at nozzle exit, (b) at $0.5D_{Nozzle}$, and (c) at $2D_{Nozzle}$: Injector per fluid insert IPR_1 = 2.7, IPR_2 = 4.5 (d) at nozzle exit, (e) at $0.5D_{Nozzle}$, and (f) at $2D_{Nozzle}$

The axial slice comparison of turbulent kinetic energy can be seen in Figure 3.26. The only differences in TKE between the two configurations occur between the nozzle exit and $0.5D_{Nozzle}$ downstream. At $2D_{Nozzle}$ downstream, the TKE contours are almost indistinguishable, as seen in Figure 3.26(c) and (f). At the nozzle exit, there is a larger area of high TKE inside the fluidic insert in the three injector configuration than the two injector configuration as there is more cross flow. This was also seen in the streamwise direction in Figure 3.22. The same can be said $0.5D_{Nozzle}$ downstream. The high TKE region spreads farther in the three injector configuration than the two injector configuration.

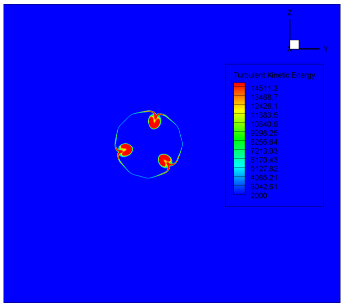

(a)

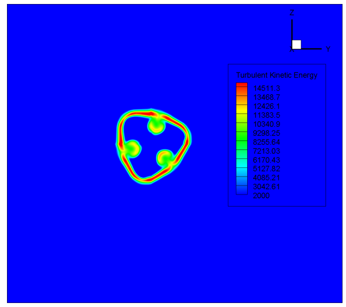

(b)

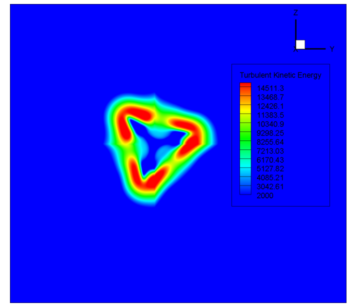

(c)

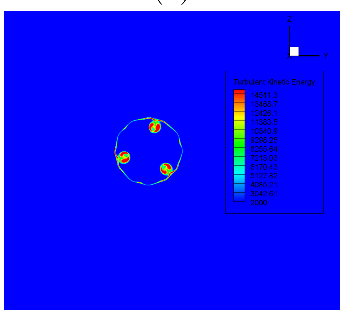

(d)

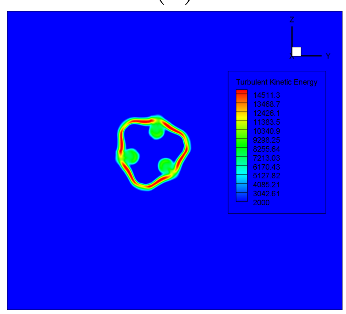

(e)

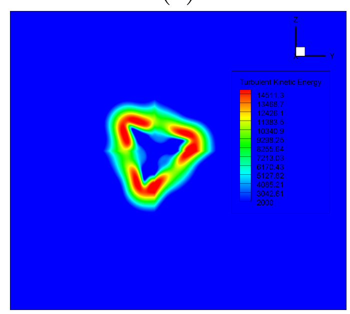

(f)

Figure 3.26. Comparison of downstream evolution of turbulent kinetic energy for two configurations of a military style nozzle NPR =3.0, M_j = 1.36, TTR = 3.0: 3 Injectors per fluidic insert all IPR = 3.6 (a) at nozzle exit, (b) at $0.5D_{Nozzle}$, and (c) at $2D_{Nozzle}$: Injector per fluid insert IPR_1 = 2.7, IPR_2 = 4.5 (d) at nozzle exit, (e) at $0.5D_{Nozzle}$, and (f) at $2D_{Nozzle}$

As seen in the three injectors into a supersonic boundary layer study, the streamwise vorticity contributes to the shape of fluidic inserts. This is also the case for the military style nozzle. The streamwise vorticity is presented in Figure 3.27. The two counter-rotating vortices at the nozzle exit fir the shape of the fluidic inserts for each configuration. In the three injector configuration, the vorticies appear to be slightly large than the two injector configuration, which agrees with the other flow parameters. There are also vortices generated from the flaps and seals of the nozzle that are comparatively much smaller than those generated by the fluidic inserts. As the vorticies travel downstream, they quickly lose strength. At $0.5D_{Nozzle}$ downstream the high amplitude vorticies are barely visible and by

$2D_{Nozzle}$ downstream they seem to have disappeared. This does not mean the vorticies have completely disappeared, rather, they have severely weakened when compared to their initial strength. The vortices continue to travel downstream but their amplitude reduces by several orders of magnitude for each configuration.

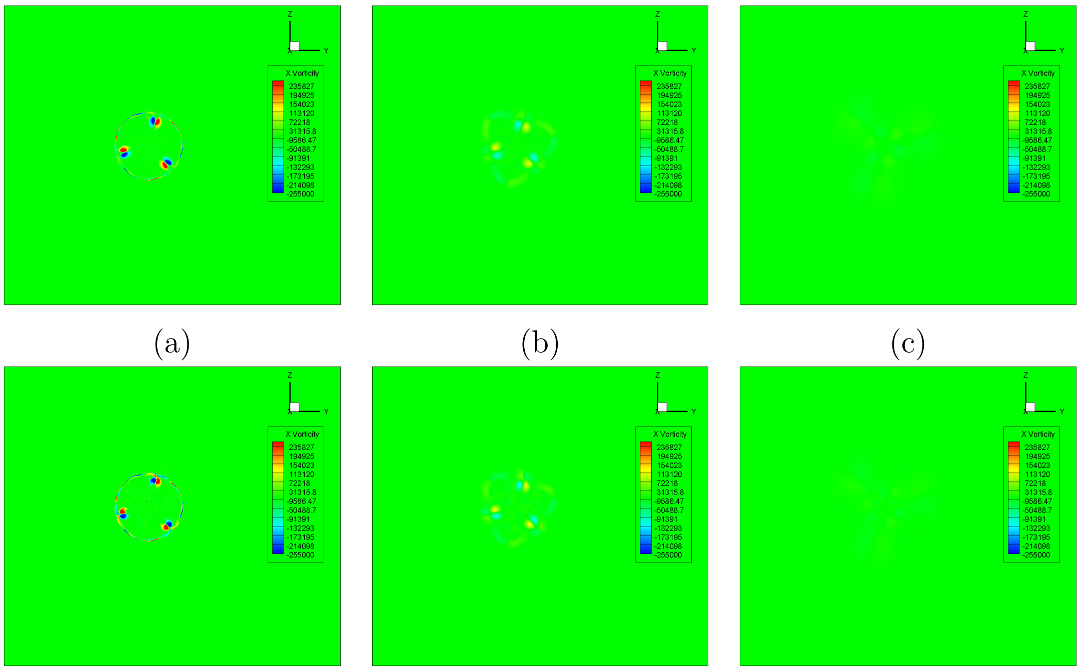

(a) (b) (c)

(d) (e) (f)

Figure 3.27. Comparison of downstream evolution of streamwise vorticity for two configurations of a military style nozzle NPR =3.0, M_j = 1.36, TTR = 3.0: 3 Injectors per fluidic insert all IPR = 3.6 (a) at nozzle exit, (b) at $0.5D_{Nozzle}$, and (c) at $2D_{Nozzle}$: Injector per fluid insert IPR_1 = 2.7, IPR_2 = 4.5 (d) at nozzle exit, (e) at $0.5D_{Nozzle}$, and (f) at $2D_{Nozzle}$

3.2.2 Increase in Reynolds Number Study

The changes in the flow of a military style nozzle when there was an increase in Reynolds number was studied. All conditions were held constant in this study so that only the size of the nozzle was varied. The NPR was set to 3.0 with an ambient pressure of 101,008 Pa, which corresponds to a Mach number of 1.36. The TTR was set to 3.0 with an ambient temperature of 288K. The initial nozzle used was the generation 1B two injector nozzle, which has an exit diameter of 0.885 inches.

The two injectors were located at 30% and 70% of the diverging section and shared a diameter of 0.053 inches. The bend in the downstream injector was also taken out to better model the capabilities of the new and upcoming experiments. The upstream injector pressure ratio, IPR_1, was set to 2.7 and the downstream injector pressure ratio, IPR_2, was set to 4.5. The nozzle geometry and mesh were then scaled by a factor of 5.73 to achieve an exit diameter of 5.07 inches. Streamwise and downstream evolution comparisons were then made between the two configurations. The purpose of the Reynolds number study is to determine if there would be any difficulties and unforeseen differences in the flow when increasing the size of the nozzle in future experiments.

3.2.2.1 Streamwise Comparison of Military Nozzle

As in previous analysis, the total pressure gives the best representation of the shape of the fluidic insert. The total pressure can be seen in Figure 3.28. There are many similarities between the two configurations. The pressure drop in the jet plume is identical and there are no discernible differences. Both plumes seem to have the same total pressure values. However, there is a difference in jet plume length. The jet plume of the GE test scale size nozzle is slightly relatively shorter than the plume of the generation 1B nozzle. The fluidic insert inside of the nozzle are practically identical. The penetration of the fluidic insert appear to be of the same relative depth. In both configurations there is a sharp increase in the shape of the fluidic insert at the downstream injector. Also there is the same relative amount of separation in both area and magnitude behind the downstream injector.

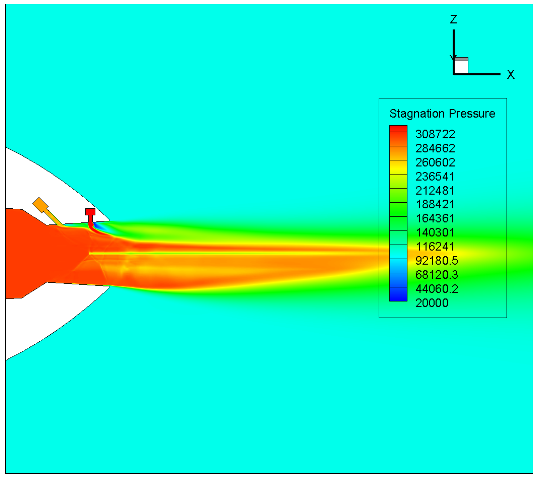

(a)

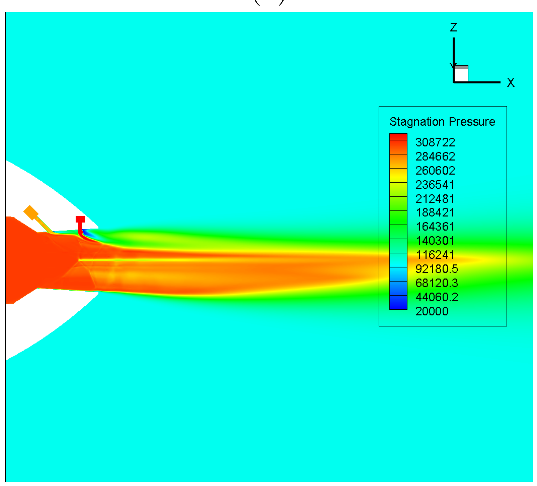

(b)

Figure 3.28. Comparison of streamwise slice with total pressure contours for two configurations of a military style nozzle NPR =3.0, M_j = 1.36, TTR = 3.0, IPR_1 = 2.7, IPR_2 = 4.5: (a) 2 Injector per fluidic insert GE Test Scale (b) 2 Injector per fluid insert Gen 1B

The comparison of Mach numbers in the increase of Reynolds number study is shown in Figure 3.29. There are also little differences in the Mach contours when comparing the two configurations. The only visible difference is the size of the jet plume that was also seen in Figure 3.28. In each configuration, there are two bow shocks that form from the two injectors. They appear to be of equal strength and relative size. The Mach disk seen in Figure 1.2 is significantly smaller due to the addition of the injectors in each configuration. However, the slip line is more apparent in the GE test scale size nozzle than the generation 1B nozzle. The shock cell structure is also slightly more defined in the GE test scale.

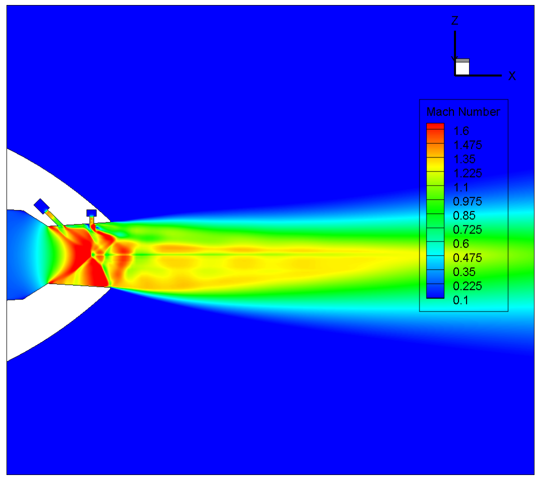

(a)

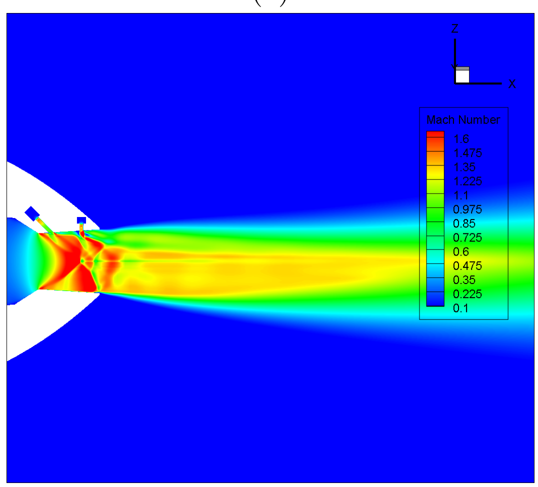

(b)

Figure 3.29. Comparison of streamwise slice with Mach number contours for two configurations of a military style nozzle NPR =3.0, M_j = 1.36, TTR = 3.0, IPR_1 = 2.7, IPR_2 = 4.5: (a) 2 Injector per fluidic insert GE Test Scale (b) 2 Injector per fluid insert Gen 1B

The turbulent kinetic energy streamwise comparison is presented in Figure 3.30. The differences in the flow is more apparent in TKE than the other previous flow parameters. The area of low TKE in the jet plume is more prominent and relatively larger in the generation 1B configuration than the GE test scale size nozzle. The areas of high TKE in the jet plume are relatively larger in the GE test scale size nozzle. This can be seen in the more burnt orange region in the top half of the plume and the darker red region in the lower half of the plume when compared to the generation 1B nozzle. However, inside of the nozzle the flow is almost identical. There is a slight amount more of high TKE relative area behind the downstream injector in the generation 1B configuration. However, this same area also extends passed the nozzle exit the same relative length.

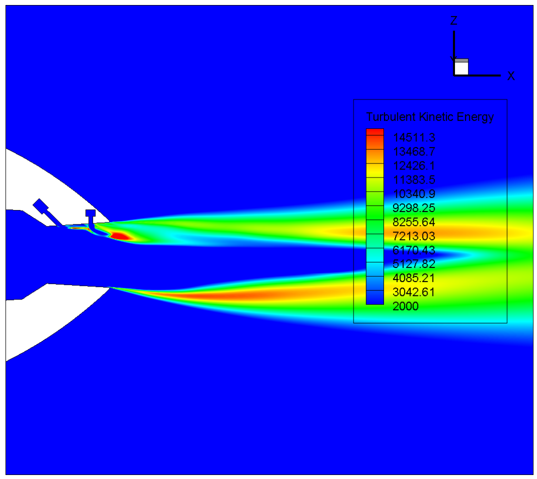

(a)

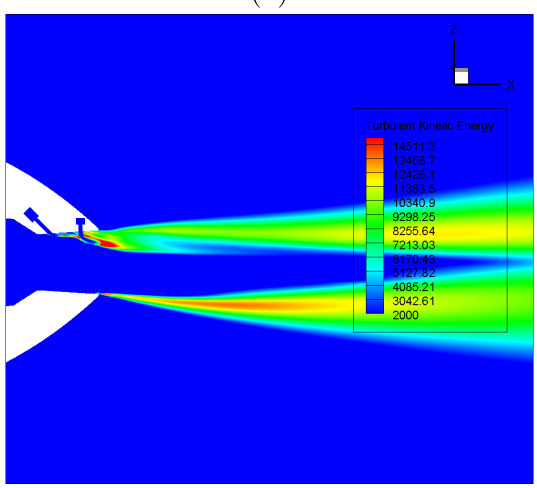

(b)

Figure 3.30. Comparison of streamwise slice with turbulent kinetic energy contours for two configurations of a military style nozzle NPR =3.0, M_j = 1.36, TTR = 3.0, IPR_1 = 2.7, IPR_2 = 4.5: (a) 2 Injector per fluidic insert GE test scale size (b) 2 Injector per fluid insert Gen 1B

3.2.2.2 Downstream Evolution Comparison of Military Nozzle

The downstream evolution comparison of total pressure for the two configurations is shown in Figure 3.31. The shape of the fluidic insert appears to be the same for both configurations. The jet plume shape starts off circular with the three bulbous fluidic inserts. The relative size of the fluidic inserts are almost identical. The plume then forms into a triangular shape the further downstream the flow travels. There is a slight difference in relative size and shape at the $2D_{Nozzle}$ location. The plume is slightly smaller in the GE test size nozzle. The fluidic inserts also seem to penetrate slightly further than the generation 1B nozzle.

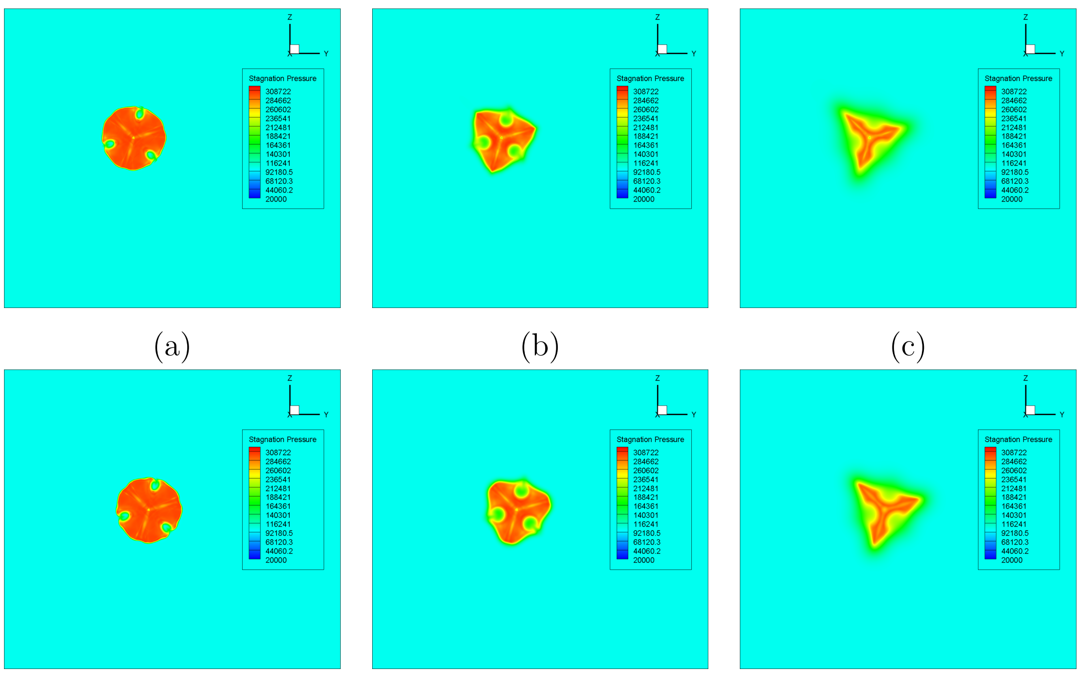

(a) (b) (c)

(d) (e) (f)

Figure 3.31. Comparison of downstream evolution of total pressure for two configurations of a military style nozzle NPR =3.0, M_j = 1.36, TTR = 3.0, IPR_1 = 2.7, IPR_2 = 4.5: GE test scale size (a) at nozzle exit, (b) at $0.5D_{Nozzle}$, and (c) at $2D_{Nozzle}$: Gen 1B (d) at nozzle exit, (e) at $0.5D_{Nozzle}$, and (f) at $2D_{Nozzle}$

The Mach number axial contours are presented in Figure 3.32. The similarities between the two configurations are again very subtle. At the nozzle exit, there is a pinwheel like area where the flow is at the jet Mach number of 1.36 as seen in the previous section and surrounded by a region of higher Mach number. The pinwheel shape is relatively smaller in the GE test scale size nozzle than the generation 1B nozzle. This suggests that the bow shocks from the downstream injector are not as large at this location. The area of smaller Mach number in between the fluidic inserts are also smaller in the GE test scale size nozzle. By $0.5D_{Nozzle}$ downstream, the core flow has reached the jet Mach number of 1.36 and about 1.0 in the fluidic inserts. The Mach number is basically identical from $0.5D_{Nozzle}$ and onward.

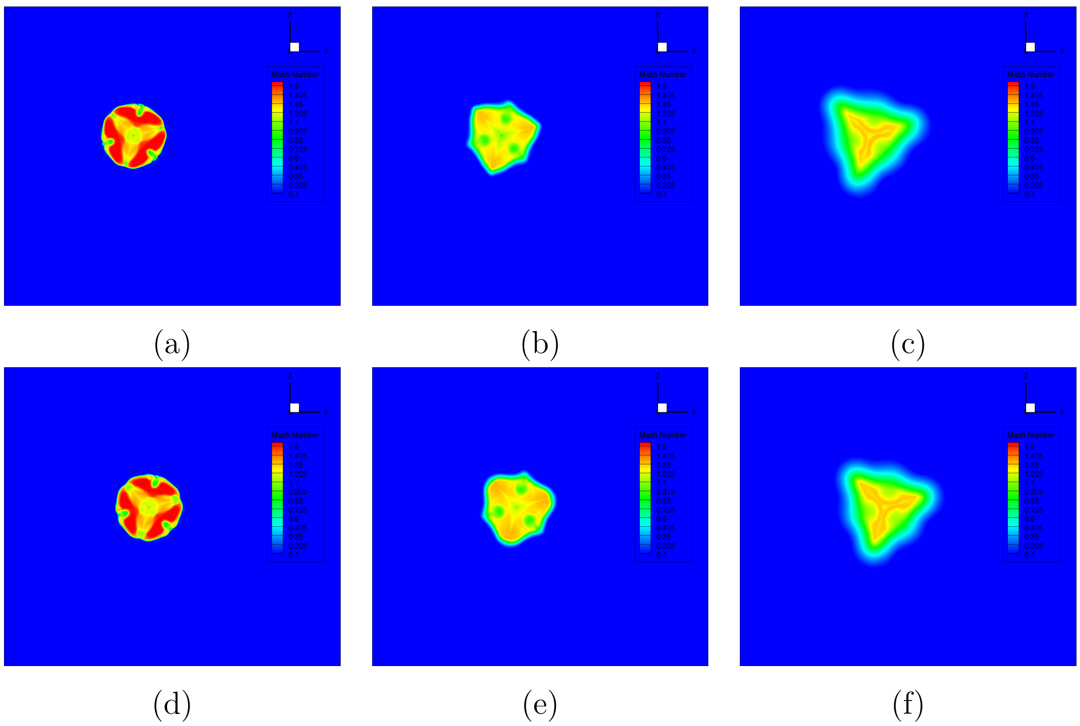

Figure 3.32. Comparison of downstream evolution of Mach number for two configurations of a military style nozzle NPR =3.0, M_j = 1.36, TTR = 3.0, IPR_1 = 2.7, IPR_2 = 4.5: GE test scale size (a) at nozzle exit, (b) at $0.5D_{Nozzle}$, and (c) at $2D_{Nozzle}$: Gen 1B (d) at nozzle exit, (e) at $0.5D_{Nozzle}$, and (f) at $2D_{Nozzle}$

The turbulent kinetic energy downstream evolution comparison between the two configurations are presented in Figure 3.33. The TKE in both configurations follows what was seen in Section 3.2.1.2. The two configurations are almost indistinguishable. There is a region of high TKE in the fluidic inserts at the nozzle exit. The TKE is then lower in the fluidic inserts and higher in the jet plume by a downstream location of $0.5D_{Nozzle}$. The high TKE region then increases in size and the TKE in the fluidic insert further decreases at the downstream location of $2D_{Nozzle}$.

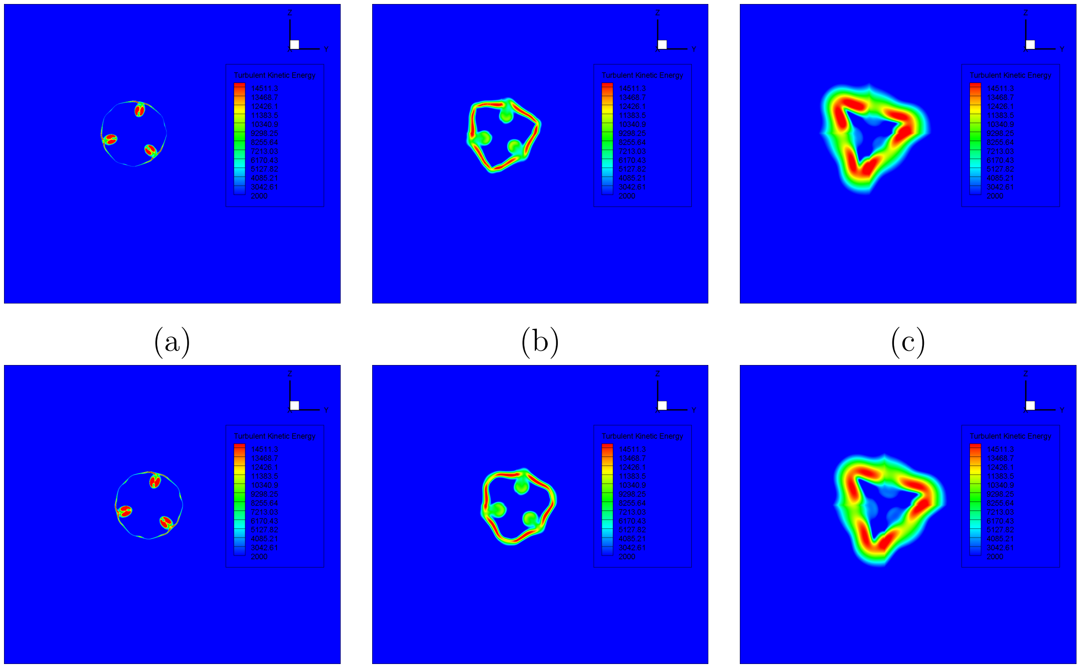

(a) (b) (c)

(d) (e) (f)

Figure 3.33. Comparison of downstream evolution of turbulent kinetic energy for two configurations of a military style nozzle NPR =3.0, M_j = 1.36, TTR = 3.0, IPR_1 = 2.7, IPR_2 = 4.5: GE test scale size (a) at nozzle exit, (b) at $0.5D_{Nozzle}$, and (c) at $2D_{Nozzle}$: Gen 1B (d) at nozzle exit, (e) at $0.5D_{Nozzle}$, and (f) at $2D_{Nozzle}$

There are major differences in the strength of streamwise vorticity between the two configurations. This is shown in Figure 3.34. There appears to be no streamwise vorticity for the GE test scale size nozzle. The generation 1B nozzle is the same as before in the previous section. There are two counter-rotating high amplitude vortices and smaller vortices from the flaps and seals of the nozzle. The vorticies then reduce severely in magnitude the further downstream the flow travels. In reality there are vortices in the GE test scale size nozzle. They are approximately a full order of magnitude in strength lower than the generation 1B nozzle. The contour scale of the GE test scale was changed in Figure 3.35 to better illustrate the generated vortices. On the chaged scale, the same counter-rotating vortices can be seen as well as the vortices from the flaps and seals. The vortices on this scale also severely reduce in amplitude the further downstream the flow travels.

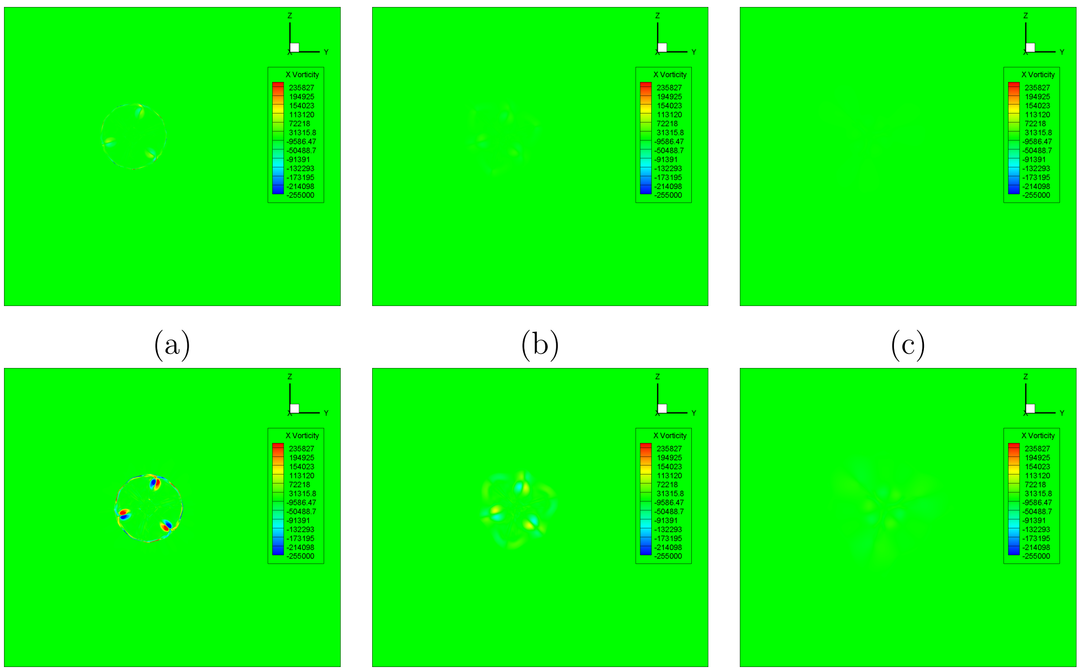

(a) (b) (c)

(d) (e) (f)

Figure 3.34. Comparison of downstream evolution of streamwise vorticity for two configurations of a military style nozzle NPR =3.0, M_j = 1.36, TTR = 3.0, IPR_1 = 2.7, IPR_2 = 4.5: GE test scale size (a) at nozzle exit, (b) at $0.5D_{Nozzle}$, and (c) at $2D_{Nozzle}$: Gen 1B (d) at nozzle exit, (e) at $0.5D_{Nozzle}$, and (f) at $2D_{Nozzle}$

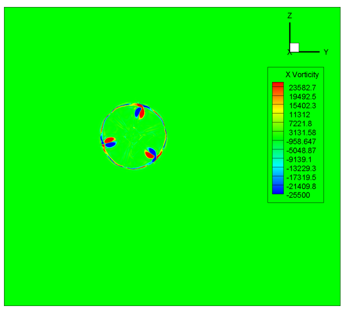

(a)

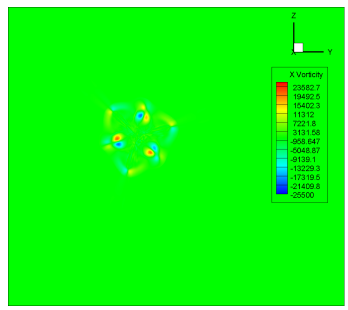

(b)

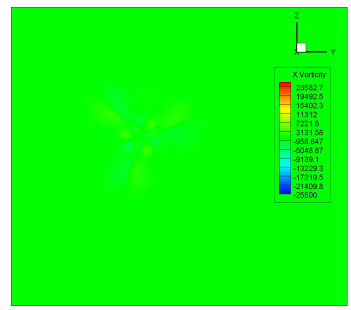

(c)

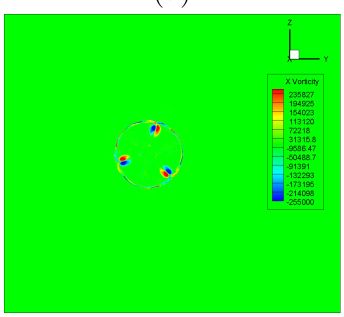

(d)

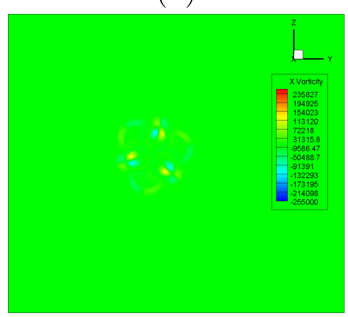

(e)

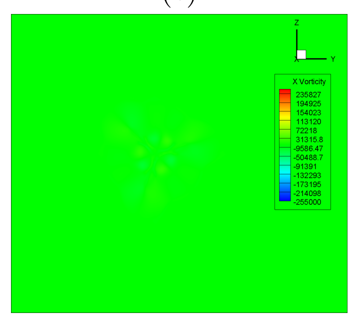

(f)

Figure 3.35. Comparison of downstream evolution of streamwise vorticity for two configurations of a military style nozzle with different scales NPR =3.0, M_j = 1.36, TTR = 3.0, IPR_1 = 2.7, IPR_2 = 4.5: GE test scale size (a) at nozzle exit, (b) at $0.5D_{Nozzle}$, and (c) at $2D_{Nozzle}$: Gen 1B (d) at nozzle exit, (e) at $0.5D_{Nozzle}$, and (f) at $2D_{Nozzle}$

3.2.3 Correlation between Noise Reduction and Flow Parameters

In this section, n attempt is made to find a correlation between noise reduction and flow parameters. If such a correlation could be found, CFD analysis could be performed to help better predict what changes in geometry or conditions would cause the best noise reduction. This would then lessen the burden of trial and error on acoustic experiments and thus an optimal configuration would be achieved more quickly. The predictions could also help the experiments know what is causing the noise reduction and they could then be better designed to achieve the corresponding flow parameters. The three parameters that were studied to find a correlation to noise reduction were the integrated magnitude of streamwise vorticity, integrated turbulent kinetic energy, and integrated Q-criterion.

The simulations that were examined can be found in Table 3.4 and Table 3.5. Case 14 in Table 3.4 refers to a baseline nozzle and so do case 3 and 6 in Table 3.5. Case 3 refers to the Gen2 baseline nozzle operating at a TTR = 1.0 and Case 6 is operating at a TTR = 2.5. There are more acoustic data available for the Gen 2 nozzle, however, only a select few cases were simulated.

Generation 1B Conditions for Noise Correlation					
NPR	TTR	Case Number	M_J	IPR_1	IPR_2
3.0	3.0	1	1.36	1.5	1.9
3.0	3.0	2	1.36	1.5	3.0
3.0	3.0	3	1.36	1.5	4.5
3.0	3.0	4	1.36	1.8	2.4
3.0	3.0	5	1.36	1.8	3.7
3.0	3.0	6	1.36	2.1	1.9
3.0	3.0	7	1.36	2.1	3.0
3.0	3.0	8	1.36	2.1	4.5
3.0	3.0	9	1.36	2.4	2.4
3.0	3.0	10	1.36	2.4	3.7
3.0	3.0	11	1.36	2.7	1.9
3.0	3.0	12	1.36	2.7	3.0
3.0	3.0	13	1.36	2.7	4.5
3.0	3.0	14	1.36	0	0

Table 3.4. Generation 1B Conditions for Noise Correlation

Generation 2 Conditions for Noise Correlation						
NPR	TTR	Case Number	M_J	IPR_1	IPR_2	IPR_3
3.0	1.0	1	1.36	3.0	3.0	3.0
3.0	1.0	2	1.36	4.5	4.5	4.5
3.0	1.0	3	1.36	0	0	0
3.0	2.5	4	1.36	3.0	3.0	3.0
3.0	2.5	5	1.36	4.86	4.86	3.51
3.0	2.5	6	1.36	0	0	0

Table 3.5. Generation 2 Conditions for Noise Correlation

The integrated magnitude of streamwise vorticity was taken on a slice at the nozzle exit. Figure 3.36 presents the calculated values. Whenever fluidic inserts were present, cases 1 through 13, there was significantly more streamwise vorticity than in the baseline, case 14. The two cases that had the best noise reduction were cases 5 and 10. Each of these cases have a relatively high value of integrated magnitude of streamwise vorticity. However, there are cases that gave less noise reduction that have a higher value of integrated magnitude of streamwise vorticity, such as cases 3 and 13. The magnitude of the integrated streamwise vorticity for the Gen 2 nozzle is shown in Figure 3.37. However, in this case the values needed to be normalized because comparisons between two different TTR are being made. The normalized integrated streamwise vorticity was calculated by dividing the original value by the exit velocity and nozzle exit diameter as given by

$$\int |\Omega^*| dA^* = \frac{1}{U_j D_j} \int |\Omega| dA. \tag{3.1}$$

Similarly with Gen 1B, there is a significantly more integrated streamwise vorticity when fluidic injectors are present when compared to the baselines, cases 3 and 6. In these cases case 5 had the best overall noise reduction and case 2 had the least overall noise reduction when fluidic inserts were present. Case 4 had the best noise reduction when the IPR were all equal. There does not seem to be any correlation between amount of streamwise vorticity and noise reduction, as the best overall case had the least amount of streamwise vorticity when fluidic inserts were present. The only conclusion that can be drawn is that there needs to be some streamwise vorticity present to gain any noise reduction.

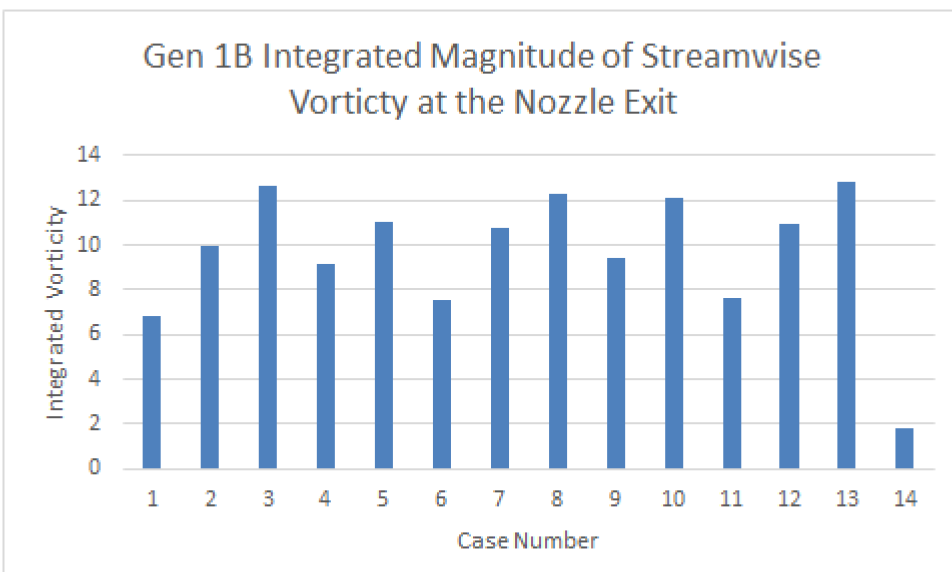

Figure 3.36. Gen 1B integrated magnitude of streamwise vorticity at the nozzle exit. Cases 5 and 10 gave the greates noise reduction

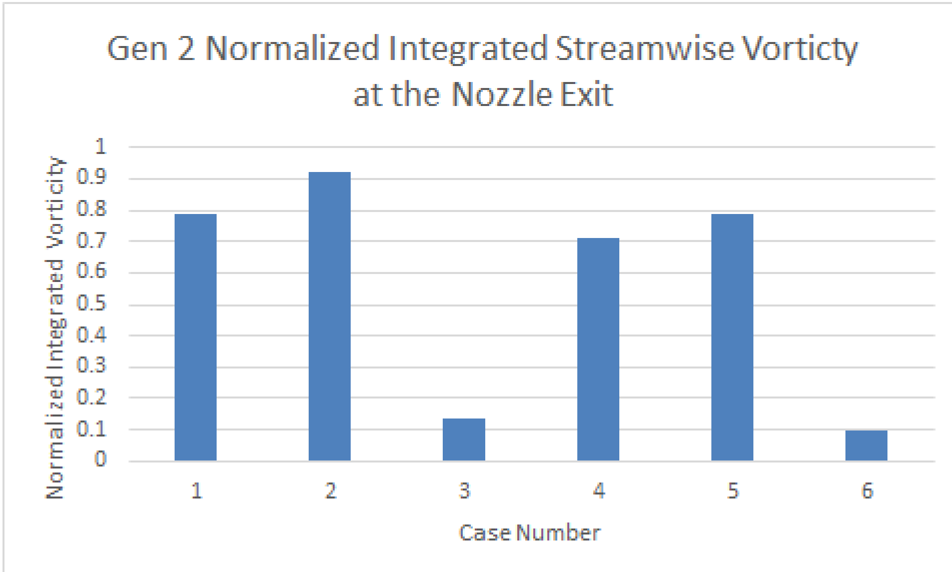

Figure 3.37. Gen 2 normalized integrated magnitude of streamwise vorticity at the nozzle exit. Cases 3 and 6 are the baseline cases

The integrated turbulent kinetic energy for the Gen 1B nozzle can be seen in Figure 3.38 and Figure 3.39. The integrated turbulent kinetic energy was taken over different volumes starting at the nozzle exit and going to a downstream location of $8D_{Nozzle}$ and then divided every $2D_{Nozzle}$. Figure 3.38 shows that there is a decrease for all the volumes in integrated TKE when fluidic inserts are present. The further downstream traveled the more TKE is present as seen in the previous section. When comparing the two best cases, case 5 and 10, the integrated TKE looks similar at all volumes. However when comparing a case that did not provide as much noise benefit, case 1, with case 5, there are very little differences at each volume level. Case 1 produced a fluidic insert that barely penetrated into the core flow of the nozzle, as seen in the work conducted by Kapusta [18], but it still gave similar integrated TKE to case 5. When looking at the total integrated TKE in the four volumes in Figure 3.39, the same conclusion can be drawn. The best cases look very similar to one another, but so do cases that did not perform as well. Subtle differences in the TKE seem to give different results in noise benefit. However, overall it is clear that a reduction in TKE is needed to have a reduction in noise.

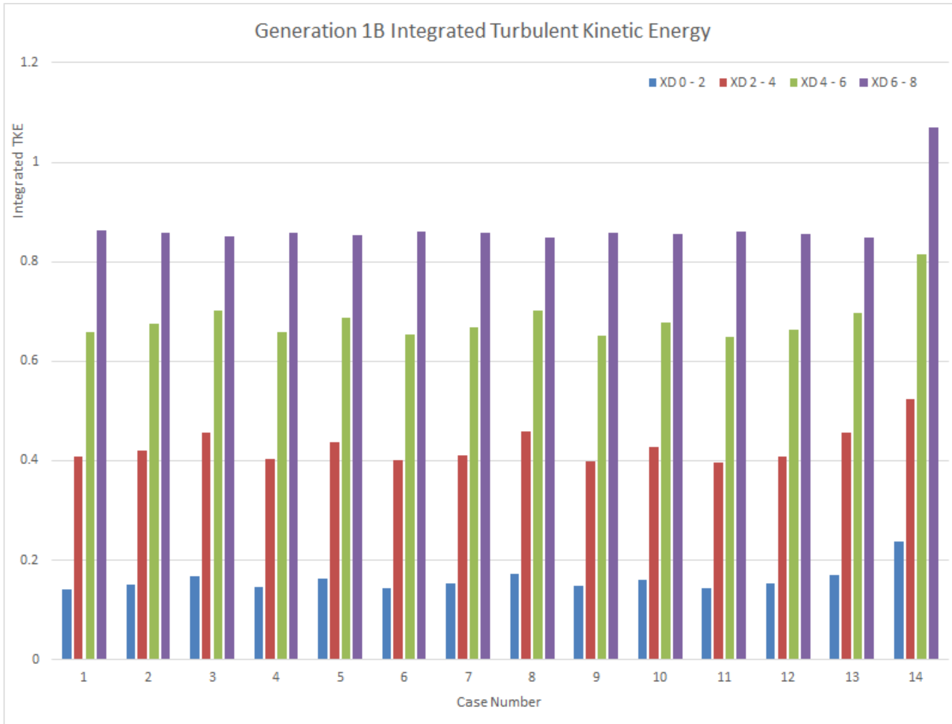

Figure 3.38. Gen 1B integrated turbulent kinetic energy in 2D volumes. Case 14 is the baseline case.

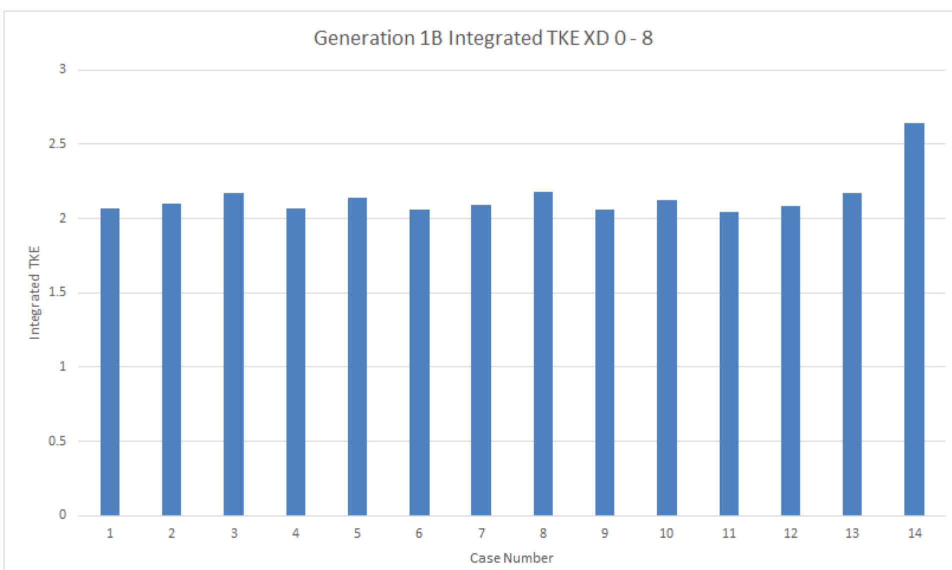

Figure 3.39. Gen 1B integrated turbulent kinetic energy from nozzle exit to $8D_{Nozzle}$. Case 14 is the baseline case

When comparing the turbulent kinetic energy in the Gen 2 nozzle, normalization is again needed. The normalized integrated TKE was obtained by dividing the original value by the exit velocity squared and the nozzle exit diamter cubed as given by

$$\int k^* dV^* = \frac{1}{U_j^2 D_j^3} \int k dV. \tag{3.2}$$

However comparison should still only be made between like TTR. The TKE was calculated the same way as the Gen 1B nozzle, but the volumes are described using the Gen 2 nozzle diameter, D_{Nozzle}. Figure 3.40 presents the integrated TKE in each of the volumes. The trend of the TKE rising the further the flow travels downstream is seen again. However, in these cases the integrated TKE is less in the baseline than when fluidic inserts are present, especially when the TTR is 1.0. The cause of this can be seen in Figure 3.42. The low values of TKE extend down the jet plume further in the baseline case than in the fluidic insert configuration. There are more areas of medium TKE, given by the green contour, in the fluidic insert case which leads to a higher value of integrated TKE. The high area of TKE in the top portion of the jet plume in the baseline configuration is reduced in the fluidic insert configurations, which is where the noise reduction occurs. Even though the overall integrated TKE is higher in the fluidic insert cases, the high intensity areas are removed directly behind the injector. This suggests that an overall reduction in TKE is not completely necessary and it is only in the regions where noise is being produced that it needs reduced.

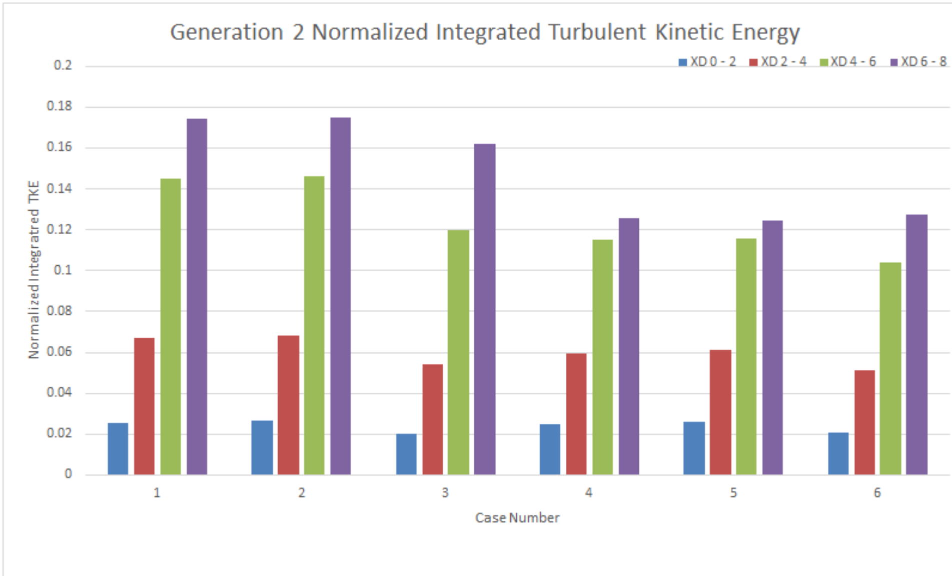

Figure 3.40. Gen 2 normalized integrated turbulent kinetic energy in different 2D volumes. Cases 3 and 6 are the baseline cases.

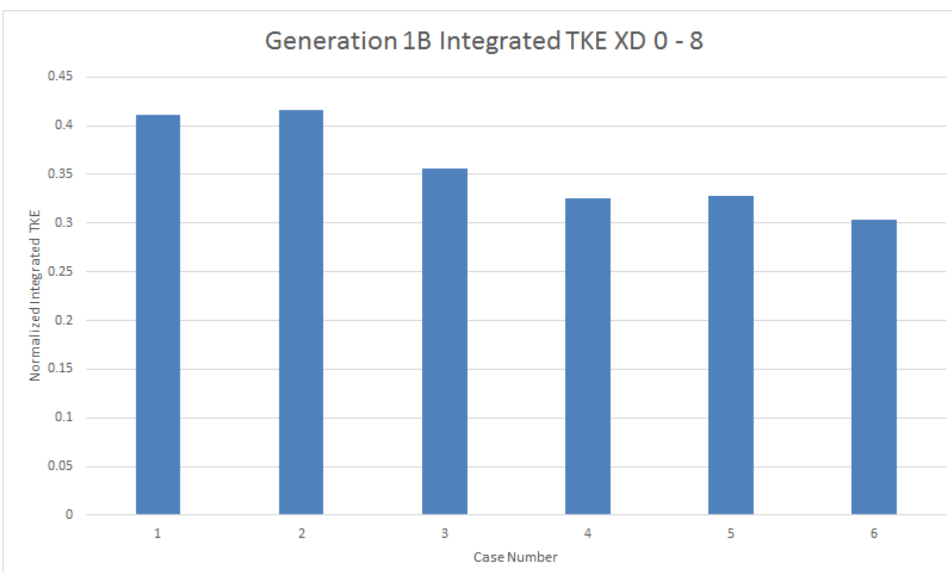

Figure 3.41. Gen 2 normalized integrated turbulent kinetic energy from nozzle exit to $8D_{Nozzle}$ distance downstream. Cases 3 and 6 are the baseline cases.

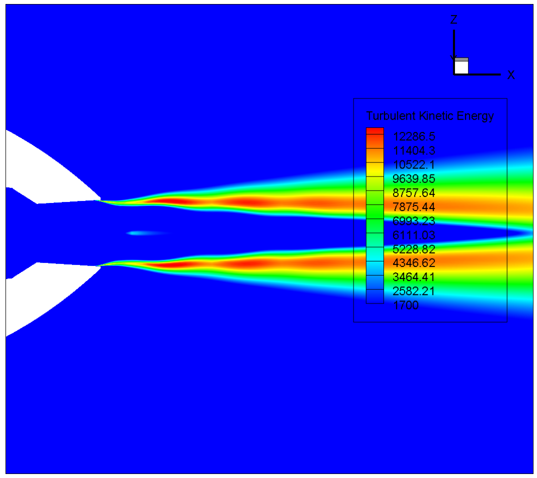

(a)

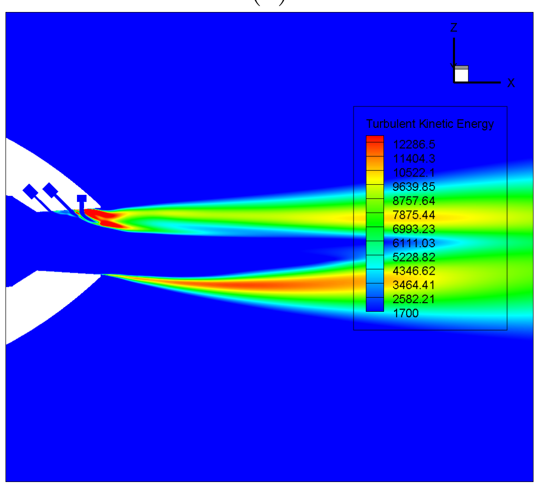

(b)

Figure 3.42. Comparison of a streamwise slice with turbulent kinetic energy contours for two configurations of a military style nozzle NPR =3.0, M_j = 1.36, TTR = 2.5: (a) Gen 2 baseline nozzle (b) 3 Injector per fluidic insert Gen 2 Best Case

The Q criterion was introduced by Hunt, Wray, and Moin. [21] It is a three dimensional vortex identifier. It is defined by the vorticity tensor, Ω, and the strain rate tensor, S. The Q criterion is defined by,

$$Q = \frac{1}{2}[|\Omega|^2 - |S|^2]. \tag{3.3}$$

A vortex is said to be present whenever the Q criterion is greater than zero. This means that a more positive value represents a more vorticity-dominated flow.

The opposite would mean a more strain rate-dominated flow. A streamwise slice of the Q criterion can be seen in Figure 3.43 for the Gen 2 TTR = 2.5 baseline and case 5 Gen 2 nozzle. The areas of red and yellow indicate that there are vorticies present whereas in the blue region there are no vortices. In the baseline nozzle case there are intermittent, axisymmetric vortices that surround the jet plume. Then further downstream there are larger vortices that separate from the jet plume. In the case with the fluidic inserts, the inserts disrupt the axisymmetric vortices and instead there is one large area of high vorticity that appears in line with a fluidic insert that travels outward from the jet plume.

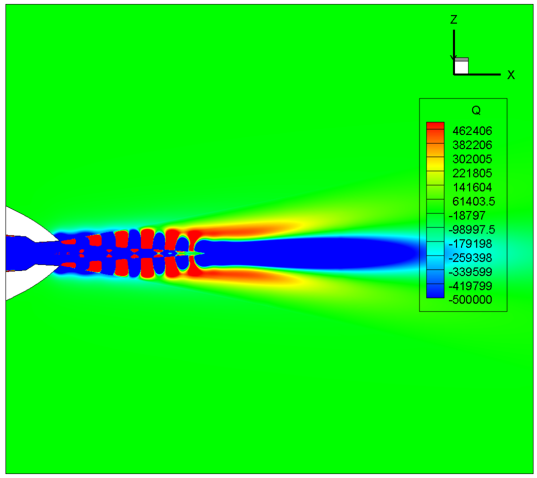

(a)

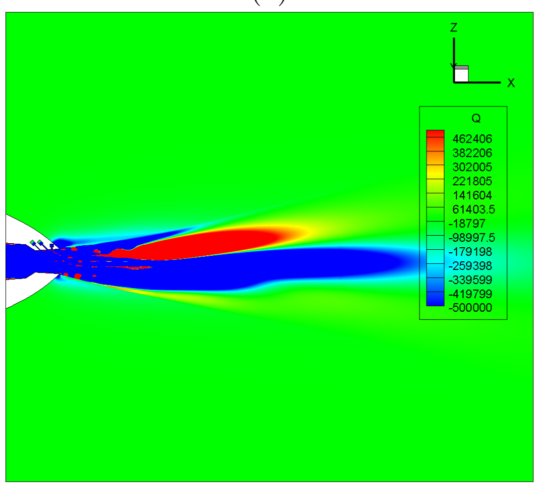

(b)

Figure 3.43. Comparison of streamwise slice with Q criterion contours for two configurations of a military style nozzle NPR =3.0, M_j = 1.36, TTR = 2.5: (a) Gen 2 baseline nozzle (b) 3 Injector per fluid insert Gen 2 Best Case

Figure 3.44 and Figure 3.45 present the integrated normalized Q criterion. The normalized values were calculated by dividing the original values by the exit velocity squared and the nozzle exit diameter cubed as given by,

$$\int Q^* dV^* = \frac{1}{U_j^2 D_j^3} \int Q dV. \tag{3.4}$$

The first notable characteristic is that there are no volumes of primarily vortex dominated flow. The second notable characteristic is that most of the total integrated Q criterion lies within the first two nozzle diameters downstream as seen in Figure 3.45. The integrated Q criterion in the first two nozzle diamters are several orders of magnitude higher. The addition of the fluidic inserts increases the amount of Q criterion in from $2D_{Nozzle}$ to $4D_{Nozzle}$ downstream when compared to the baseline case. The flow does become slightly more vortex dominated in the $4D_{Nozzle}$ to $6D_{Nozzle}$ when the fluidic inserts are present as the values become less negative when compared to the baseline. There are no strong quantitative correlations, only these few trends.

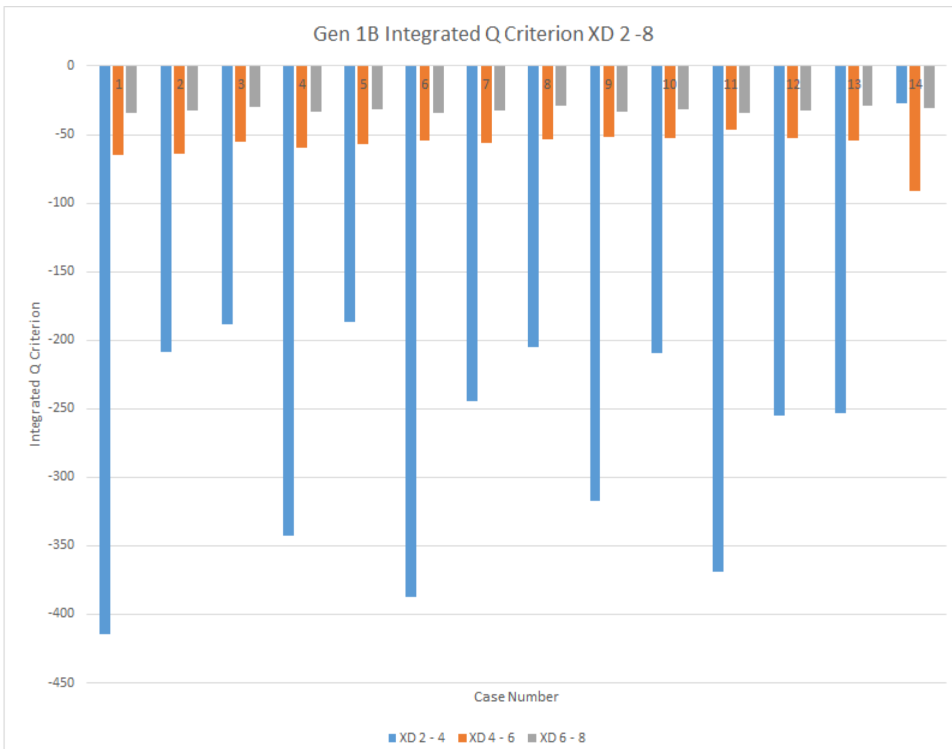

Figure 3.44. Gen 1B normalized integrated Q criterion from $2D_{Nozzle}$ to $8D_{Nozzle}$. Case 14 is the baseline case. Cases 5 and 10 gave the greatest noise reduction.

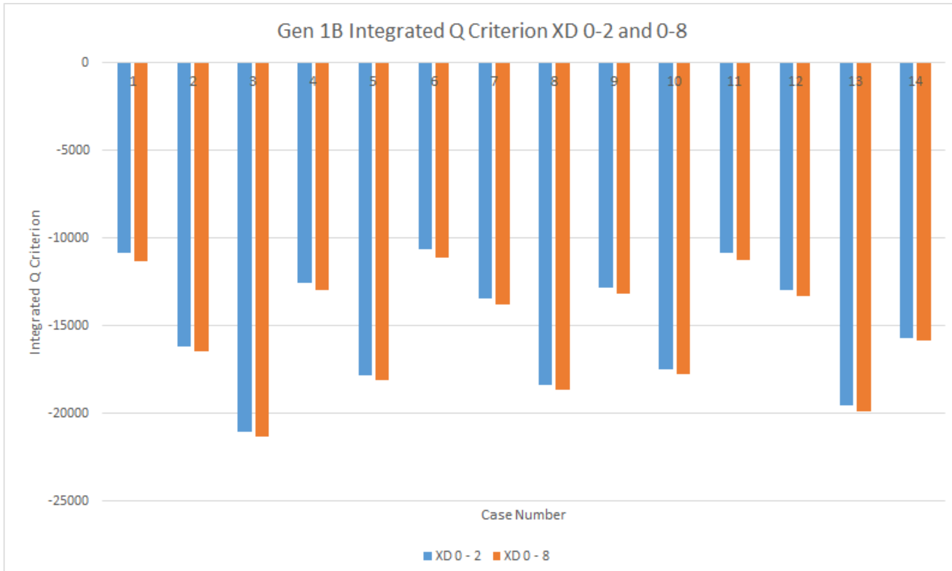

Figure 3.45. Gen 1B normalized integrated Q criterion from nozzle exit to $2D_{Nozzle}$ and nozzle exit to $8D_{Nozzle}$. Case 14 is the baseline case. Cases 5 and 10 gave the greatest noise reduction.

Similar qualities can be seen in the Gen 2 case as presented in Figure 3.46 and Figure 3.47. The most dominant region is the nozzle exit to $2D_{Nozzle}$ as seen in the Gen 1B configuration. The baseline case has higher magnitude of Q criterion in the $2D_{Nozzle}$ to $4D_{Nozzle}$ downstream region, which is different from what was seen in the Gen 1B cases. The trend of becoming less negative with the addition of the fluidic inserts in the $4D_{Nozzle}$ to $6D_{Nozzle}$ region is also seen. There are no clear correlations of this parameter to noise reduction.

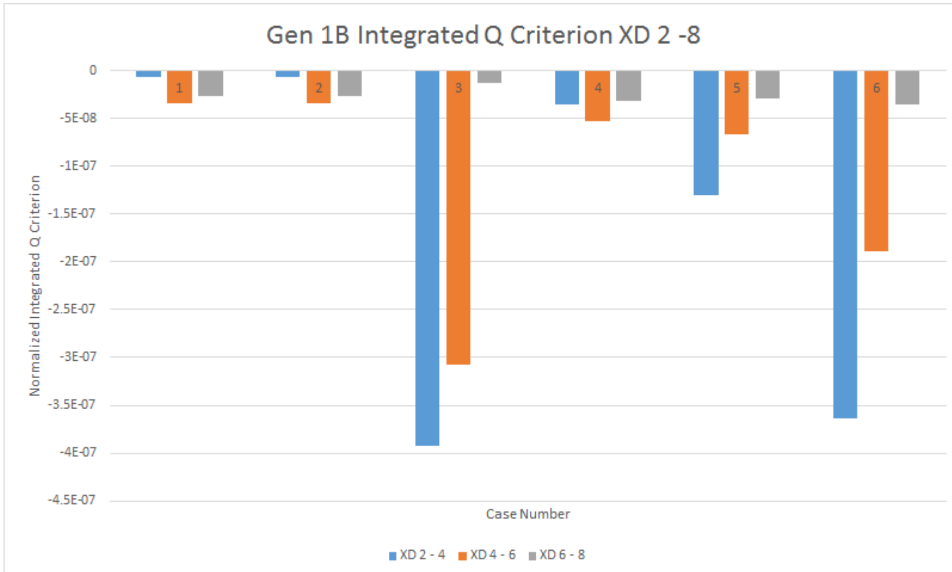

Figure 3.46. Gen 2 normalized integrated Q criterion from $2D_{Nozzle}$ to $8D_{Nozzle}$. Case 3 and 6 were the baseline cases.

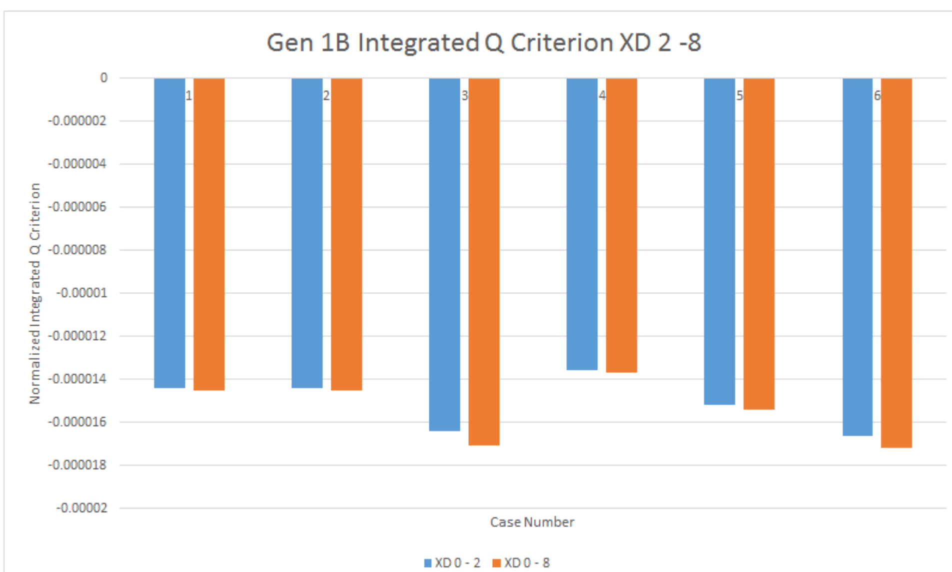

Figure 3.47. Gen 2 normalized integrated Q criterion from nozzle exit to $2D_{Nozzle}$ and nozzle exit to $8D_{Nozzle}$. Case 3 and 6 were the baseline cases.

Chapter 4 Conclusions

4.1 Summary of Work

The purpose of this project was to further understand the flow generated by fluidic inserts in a military style nozzle and to find a flow parameter that could be correlated to noise reduction.

This lead to a better understanding of the ANSYS suite. Specfically, the full abilities of ANSYS-ICEM are now understood. Previously there was a good degree of manual manipulation needed to improve the quality of the mesh. The vertices of the blocks were moved manually to improve the determinant and minimum angle of the cells. It was found that moving individual nodes is a much more effective method. This is done through using the mesh smoothing tool and it is completely automated. A value only needs to be input for the desired determinant or minimum angle and the tool will sweep through the nodes and make minimal adjustments to achieve the desired value. It was also newly discovered that the minimum determinant value needed for ANYSY-CFX to successfully complete a simulation is lower than previously thought. Before it was thought that the minimum determinant needed was 0.3 and it was found that ANSYS-CFX can handle values as low as 0.1, but 0.2 is the desired target. This new finding allows for quicker mesh generation and better simulations using ANSYS-CFX.

The simpler geometry of a supersonic flat plate boundary layer was used to better understand the flow generated by a three injector fluidic insert. The shape of a three injector fluidic insert is different than the flow generated by a two injector fluidic insert. The total pressure and total temperature are the best parameters to visualize the shape of the insert and the streamwise vorticity is what drives the bulbous shape of the insert. The slope of the three injector configuration is much smoother and gradual compared to the two injector configuration. There is a sharp increase in depth of the fluidic insert at the downstream injector of the two injector configuration that is not present in the three injector configuration. Bow shocks form from each injector in the fluidic insert and the shocks from the middle and downstream injector merge into a single, larger shock. Changes in the downstream injector angle also yielded different results. Generally, as the downstream injector angle is increased the shape of the fluidic insert becomes larger, penetrates further, separates from the wall earlier, and the high TKE region generated from the downstream injector travels further downstream. However, the results are similar enough to previous simulations that if needed, due to physical constraints, an injector with lower than a 90°angle to the centerline should work similarly.

The flow differences between a two injector and three injector per fluidic insert military style nozzle are very subtle. The shape follows what was seen in the simpler supersonic boundary layer. There is a larger total temperature drop in the jet plume for the two injector configuration. This indicates that the three injector configuration breaks up the shock cell structure more so than the two injector configuration. This is because the fluidic insert penetrates deeper into the core flow with the three injector configuration due to the middle injector reducing the momentum of the core flow even further. There is a region of high TKE that extends further downstream of the downstream injector in the three injector configuration than the two injector case. Whenever there is an increase in Reynolds number from scaling the nozzle up by a factor appropriate for university to industry scale, there are almost no distinguishable relative differences. The fluidic insert shape, shock structure, and turbulent kinetic energy are all practically identical. There was only one major difference and that was that the strength of the high amplitude counter rotating vortices generated by the fluidic inserts were lower by an order of magnitude in the larger nozzle. There were also no definitive correlations in the observed flow parameters with noise reduction. There were some weak correlations, such as a reduction in the integrated TKE generally yields a reduction in noise. But subtle differences in flow properties results in a significant difference in noise reduction. The same can be said about the integrated magnitude of streamwise vorticity at the nozzle exit. There was a correlation where an increase in magnitude of streamwise vorticity gave noise benefits but there were no quantitative values that could be determined. There were also no clear correlations with the Q criterion, only a few weak trends.

4.2 Future Work

Future work should include the generation of additional meshes that correspond to future and past experiments. This would include a military style nozzle with six fluidic inserts that have two and three injectors per insert. The inserts would be equally separated such that there would be fluidic inserts directly opposite from each other. A mesh should also be generated to simulate the experiments that have been conducted at GE. This would include a GE test scale size nozzle that has three fluidic inserts with five injectors per insert. A comparison should then be made between the simulations from these two meshes and the past simulations and experiments.

Further analysis should be conducted on future and previous simulations including finding a correlation between flow parameters and noise reduction. One parameter to look into would be the λ_2 vortex criterion. This criterion makes use of the strain rate tensor and the vorticity tensor and the intermediate eigenvalue of the strain and vorticity tensor according to Jeong and Hussain. [22] This criterion is similar to the Q criterion in that they both are used to identify vortices.

The generated thrust should be calculated for all past and future simulations as well. This would involve using the momentum integral equation. The thrust could be used to analyze the effect of the injectors at takeoff and also at cruising altitude to see if there are any areas of concern.

ANSYS-Fluent should also be considered in the future. Fluent has the capabilities to run a Large Eddy Simulation. Large Eddy Simulation would give better insight into the turbulence generated by the military style nozzle with fluidic inserts than the steady RANS calculations of ANSYS-CFX. The better turbulence calculations could give useful insight into the flow generated by the nozzle as well as better simulate the radiated noise.

Appendix | High Speed Jet Experiments

This section provides a brief description of the experimental configuration and approach. The experiments were conducted primarily by Russel Powers and Scott Hromisin and other grad students contributed. A more complete description of the experiments is given in [3]. The experiments were conducted inside of the Pennsylvania State University Jet Aeroacoustics Laboratory shown in Figure .1. A military style nozzle similar to the GE F404 family was used in the experiments.

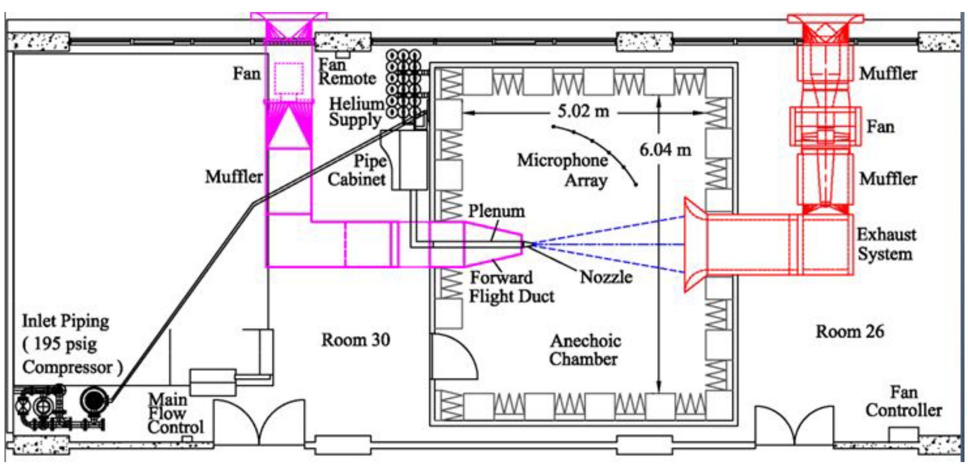

Figure .1. Schematic of the Penn State anechoic high speed jet noise facility [3]

The military style nozzle used in the experiments is similar to the one used in the simulations. The nozzle is conical in the convergent divergent and the divergent section has a faceted geometry. The facets represent the flaps and seals which are used to control the area of the nozzle to be used at different operating conditions. The nozzle used has a design Mach number of 1.65 and an exit diameter of 1.8 cm.

The nozzle has six total injectors and used three fluidic inserts. The fluidic inserts are separated equally azimuthally by 120°. The upstream injector is located at 30% of the distance from the throat to the nozzle exit. This injector is angle 45°to the nozzle centerline. The downstream injector is located at 70% of the distance from the nozzle throat to the nozzle exit and is 90°to the centerline. The nozzle can be seen in Figure .2.

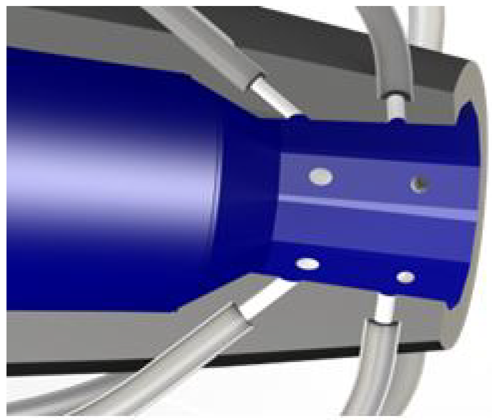

Figure .2. Schematic drawing of nozzle with 3 fluidic inserts and 2 injectors per insert [3]

The ability to heat the flow was not possible with the nozzle models used in the experiments. To simulate a TTR that is greater than 1.0, a mixture of helium and air was used. This was to replicate the higher jet exit velocity and decrease in jet density. Kinzie and McLaughlin [23] demonstrated that this mixture of helium and air is able to replicate the noise characteristics of a heated jet.

The anechoic chamber has dimensions of 5.02 m x 6.04 m x02.79 m. There is a large exhaust system at the back end oc the chamber. The exhaust minimizes air recirculation and potential helium buildup. The cut off frequency of the champer is 250 Hz. The facility has 23 microphones to take acoustic measurements. The microphones are positioned so the diaphragms are at a grazing incidence to the centerline of the jet exhaust and measurements are taken from 20°to 130°from the jet downstream axis.The microphones are position in the fair-field as they are approximately 1.8 meters from the nozzle exit.

The exterior of the jet nozzle and the upstream plenum can be seen in Figure .3. A shroud was built to encase the fluidic injectors to provide a cleaner aerodynamic path. The shroud contains all of the piping and tubing of the injectors and the jet plenum. The shroud allows the facility to operate at forward flight conditions. The shroud can be seen in Figure .4.

Figure .3. Photograph of nozzle with injectors [3]

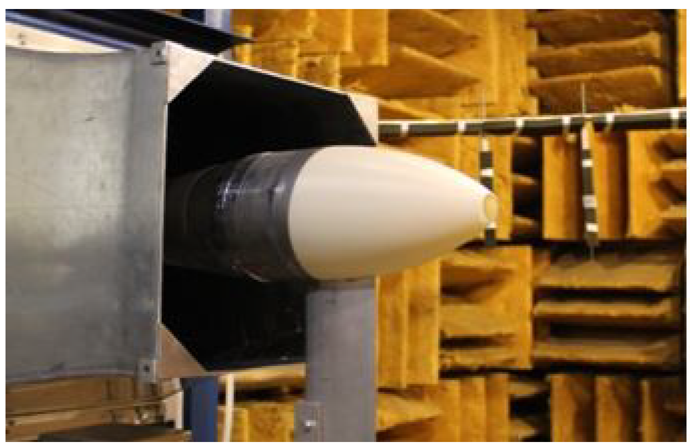

Figure .4. Photograph of nozzle shroud [3]

Bibliography

[1] University, V. T. (2001), "Nozzle Applet," http://www.engapplets.vt.edu/fluids/CDnozzle/cdinfo.html.

[2] ANSYS *Release 15.0, ICEM CFD, Users Manual and Programmers Guide*, ANSYS, INC.

[3] Morris, P. J., D. K. McLaughlin, R. W. Powers, and M. J. Kapusta (2014) "Prediction, Experiments and Optimization of High-Speed Jet Noise Reduction Using Fluidic Inserts," in *50th AIAA/ASME/SAE/ASEE Joint Propulsion Conference*, p. 3737.

[4] FAA (2016), "Aircraft Noise Issues," .
URL `http://www.faa.gov/about/office_org/headquarters_offices/apl/noise_emissi`

[5] Seiner, J. M., L. S. Ukeiley, and B. J. Jansen (2005) "Aero-performance efficient noise reduction for the F404-400 engine," *AIAA paper*, **3048**, p. 2005.

[6] Munday, D., E. Gutmark, J. Liu, and K. Kailasanath (2009) "Flow Structure of Supersonic Jets From Conical CD Nozzles," in *39th AIAA Fluid Dynamics Conference, San Antonio, TX, Jun*, vol. 24.

[7] Thomson, W. (1871) "XLVI. Hydrokinetic solutions and observations," *The London, Edinburgh, and Dublin Philosophical Magazine and Journal of Science*, **42**(281), pp. 362–377.

[8] Powers, R. W., C.-W. Kuo, and D. K. McLaughlin (2013) "Experimental comparison of supersonic jets exhausting from military style nozzles with interior corrugations and fluidic inserts," *AIAA Paper*, **2186**, p. 2013.

[9] Seiner, J. M. (1984) "Advances in high speed jet aeroacoustics," in *Orbit-Raising and Maneuvering Propulsion: Research Status and Needs*, p. 41.

[10] Harper-Bourne, M. and M. Fisher (1974) "The noise from shock waves in supersonic jets," *AGARD Noise Mech. 13 p(SEE N 74-22640 14-02).*

[11] Viswanathan, K. (2006) "Scaling laws and a method for identifying components of jet noise," *AIAA journal*, **44**(10), pp. 2274–2285.

[12] Bridges, J. E. (2009) *Broadband shock noise in internally-mixed dual-stream jets*, National Aeronautics and Space Administration, Glenn Research Center.

[13] Tam, C., J. Seiner, and J. Yu (1986) "Proposed relationship between broadband shock associated noise and screech tones," *Journal of Sound and Vibration*, **110**(2), pp. 309–321.

[14] Tam, C. K. (1995) "Supersonic jet noise," *Annual Review of Fluid Mechanics*, **27**(1), pp. 17–43.

[15] W. Tam, C. K. (2009) "Mach wave radiation from high-speed jets," *AIAA journal*, **47**(10), pp. 2440–2448.

[16] ANSYS *Release 15.0, CFX, CFX-PRE Users Guide, Modeling Guide, Theory Guide, and CFX-SOLVER Manager Users Guide*, ANSYS, INC.

[17] Huang, P., J. Bardina, and T. Coakley (1997) "Turbulence modeling validation testing and development," *NASA Technical Memorandum*, **110446**.

[18] Kapusta, M. (2015) *Simulations of the Flow Generated By Fluidic Inserts For Supersonic Jet Noise Reduction Based on Steady RANS Ssimulations*, Master's thesis, Pennsylvania State University.

[19] Papamoschou, D., J. Xiong, and F. Liu (2014) "Reduction of radiation efficiency in high-speed jets," *AIAA Paper*, **2619**.

[20] Online (2001), "Symmetric problem-Asymmetric prediction," .
URL `http://www.cfd-online.com/Forums/main/3044-symmetric-problem-asymmetric-prediction.html`

[21] Hunt, J. C., A. Wray, and P. Moin (1988) "Eddies, streams, and convergence zones in turbulent flows," .

[22] Jeong, J. and F. Hussain (1995) "On the identification of a vortex," *Journal of fluid mechanics*, **285**, pp. 69–94.

[23] Kinzie, K. W. and D. K. McLaughlin (1999) "Measurements of supersonic helium/air mixture jets," *AIAA journal*, **37**(11), pp. 1363–1369.